UNIVERSITY OF CALIFORNIA,
IRVINE

Cephalopod-Inspired Reflectin-Based Photonic Devices

DISSERTATION

submitted in partial satisfaction of the requirements
for the full degree of

DOCTOR OF PHILOSOPHY

in Materials Science and Engineering

by

Long Phan

Dissertation Committee:
Professor Alon A. Gorodetsky, Chair
Professor Nancy Da Silva
Professor Francesco Tombola

2016

DEDICATION

To Mom and Dad,
you risked your lives to provide me with this opportunity,
and so,
I will forever strive to honor your sacrifice.

TABLE OF CONTENTS

Page

LIST OF FIGURES

ACKNOWLEDGEMENTS

A huge debt of gratitude is owed to my advisor, Professor Alon Gorodetsky, for his eximious guidance and constant support throughout my PhD. I have become a more confident scientist and critical thinker thanks to his tutelage. I hope that David, Amir, and I have graduated from being "puppies" in Alon's eyes.

To Rena, for always being by my side, bringing light into my life when it is dark, and together shining bright when there is joy; words cannot express this gratitude – may my dedication, affection, and love for you ring eternal.

To Linh, for your constant love and occasional redirection when I stray.

To Đi Phu and An, for always supporting me and making me smile during the tough times.

I would like to thank David Ordinario and Amir Mazaheripour for their unwavering friendship for the last nine years. From solving problem sets late into the night or getting into trouble with Alon, we have shared so many wonderful memories and experiences; I hope that our paths continually converrge in the future.

I would like to thank Professor Albert Yee's Laboratory for the use of their optical microscope and atomic force microscope, Professor Matthew Law's Laboratory for the use of their atomic force microscope and integrating sphere, Dr. Beniam Berhane and the UCI Mass Spectroscopy facility for help with tryptic digest and MALDI, the UCI Laser Spectroscopy Facility for use of their instruments for biophysical characterization, and Filmetrics for refractive index acquisition.

I would like to thank Dr. Ward G. Walkup IV for teaching me everything I know about biology and protein expression, Dr. Vineet Nair for his help with the integrating sphere measurements, and the students from Professor Da Silva and Professor Wang's labs for fun scientific discussions and occasionally putting up with my antics in ET.

Finally, I would like to thank our funding sources for making this research possible, including APRA-E, DAPRA, AFOSR, and DHI.

Chapter 4 of this thesis is an adaptation of the material as it appears in the manuscript draft submitted to Advanced Optical Materials. The co-authors listed in this publication directed and supervised research which forms the basis for the material in the chapter. Author Contributions: D. D. O., P. E. S., and A. A. G. conceptualized and designed the experiments; D. D. O., E. M. L., and L. P. performed the research; M. N., J. P. L., and M. J. A. helped prepare material for experiments, D. D. O. and A. A. G. analyzed the data; and D. D. O., P. E. S., and A. A. G. wrote the paper.

CURRICULUM VITAE

Long Phan

Long.Phan@caa.columbia.edu · (978) 618-8463 · 69109 Verano Place · Irvine, CA 92617
www.linkedin.com/in/LongPhanCU

EDUCATION

University of California, Irvine, Henry Samueli School of Engineering, Irvine, CA
PhD in Materials Science and Engineering Nov. 2016
M.S. in Materials Science and Engineering June 2013

Columbia University, Fu Foundation School of Engineering and Applied Science, New York, NY
B.S. in Materials Science and Engineering May 2011

RESEARCH EXPERIENCE

Gorodetsky Group for Biomolecular Electronics, UC Irvine, Irvine, CA
Graduate Researcher Sept. 2011 – Nov. 2016

- Lead project researching reconfigurable thin films derived from cephalopod structural proteins for applications in advanced camouflage coatings, protein-based protonic transistors, and neural stem cell growth, resulting in 11 peer-reviewed publications and 2 patents. Responsibilities include protein expression and purification, biophysical characterization, protein/polymer thin film fabrication, and thin film characterization
- Collaborate with PI in writing full proposals; contributed to successful grants from ARPA-E, DARPA, and AFOSR

Naval Research Laboratory, Surface Nanoscience and Sensor Technology, Washington, DC Nov. 2016
Visiting Researcher

- Investigate protonic conductivity characteristics in reflectin thin films under simultaneous applied bias and high humidity using customized spectrophotometer and atomic force microscope

Marianetti Research Group, Columbia University, New York, NY
Undergraduate Research Assistant May 2010 – May 2011

- Performed Density Functional Theory (DFT) analysis using the Vienna Ab Initio Simulation Program (VASP) to analyze failure of molybdenum disulfide (MoS_2) monolayers

Chan Research Group, Columbia University, New York, NY
Undergraduate Research Assistant May 2010 – Sept. 2010

- Modernized the group's modeling practices by tutoring labmates in the CrystalMaker visualization program

MENTORING / MANAGEMENT

Business Plan Competition (BPC), UC Irvine Paul Merage School of Business Spring 2015
Contestant, Team "Allyte"

- Ranked in top 16 in a competition with 60+ teams across entire university
- Formulated a business plan and product (disposable infrared-reflective stickers for soldiers) using technology derived from cephalopod-inspired reconfigurable infrared camouflage research and presented to a panel of venture capitalists for potential funding in a university-wide competition setting

"Chemistry for Engineers", UC Irvine Fall 2014, 2015, 2016

Teaching Assistant

- Serve as teaching assistant for a course with more than 250 students from diverse academic backgrounds and led multiple discussion sections of more than 30 students each to deepen student learning

Gorodetsky Group for Biomolecular Electronics, UC Irvine Nov. 2011 – Nov. 2016

Graduate Student Mentor

- Manage 11 undergraduate students and teach various lab techniques/processes during their tenures in the Gorodetsky Group, with enough contribution for almost all to gain authorship on published journal articles
- Mentor for Mercedeez Aquino, Jonah-Micah Jocson, Emil Karshalev, Justin Kerr, Jessica Leal-Cruz, James Long, Mahan Naeim, Michael Nguyen, Tam Nguyen, Michael Shenk, Sean Winchester

PEER-REVIEWED PUBLICATIONS

11. D. D. Ordinario, E. M. Leung, **L. Phan**, M. Naeim, J. P. Kerr, M. J. Aquino, P. E. Sheehan, A. A. Gorodetsky. "Protochromic Devices from a Cephalopod Structural Protein". *Submitted*.
10. **L. Phan**, R. Kautz, E. M. Leung, K. L. Naughton, Y. Van Dyke, A. A. Gorodetsky. "Dynamic Materials Inspired by Cephalopods". *Chem. Mater.* **2016**, dx.doi.org/10.1021/acs.chemmater.6b01532.
    - Part of the *Up-and-Coming* series
9. K. L. Naughton, **L. Phan**, E. M. Leung, R. Kautz, Q. Lin, Y. Van Dyke, B. Marmiroli, B. Sartori, A. Arvai, S. Li, M. E. Pique, M. Naeim, J. P. Kerr, M. J. Aquino, V. A. Roberts, E. D. Getzoff, C. Zhu, S. Bernstorff, A. A. Gorodetsky. "Self-Assembly of the Cephalopod Protein Reflectin". *Adv. Mater*. **2016**, DOI:10.1002/adma.201601666.
    - Selected for inside back cover feature
8. D. D. Ordinario, **L. Phan**, W. G. Walkup IV, Y. Van Dyke, E. M. Leung, M. Nguyen, A. G. Smith, J. Kerr, M. Naeim, I. Kymissis, A. A. Gorodetsky. "Production and Electrical Characterization of the Reflectin A2 Isoform from Doryteuthis (Loligo) pealeii". *RSC Adv.* **2016**, *6*, 57103-57107.
7. D. D. Ordinario, **L. Phan**, Y. Van Dyke, T. Nguyen, A. G. Smith, M. Nguyen, N. M. Mofid, M. K. Dao, A. A. Gorodetsky. "Photochemical Doping of Protonic Transistors from a Cephalopod Protein". *Chem. Mater.* **2016**, *28*, 3703-3710.
6. **L. Phan**, R. Kautz, J. Arulmoli, I. H. Kim, D. T. T. Le, M. A. Shenk, M. M. Pathak, L. A. Flanagan, F. Tombola, A. A. Gorodetsky. "Reflectin as a Material for Neural Stem Cell Growth". *ACS Appl. Mater. Interfaces,* **2015**, *8*, 278–284.
5. **L. Phan**, D. D. Ordinario, E. Karshalev, M. Shenk, A. A. Gorodetsky. "Infrared Invisibility Stickers Inspired by Cephalopods". *J. Mater. Chem. C*. **2015,** *3,* 6493–6498.
    - Part of the *Bioelectronics* joint themed issue
    - Selected for front cover feature
    - Featured as a 2016 Journal of Materials Chemistry C Hot Paper
4. D. D. Ordinario, **L. Phan**, J-M. Jocson, T. Nguyen, A. A. Gorodetsky. "Protonic Transistors from Thin Reflectin Films". *APL. Mat.* **2015,** *3,* 014907.
    - Selected as an *Editor's Pick*
    - Part of the *Biomaterials and Bioelectronics* special issue
3. D. D. Ordinario, A. M. Burke, **L. Phan**, J-M. Jocson, H. Wang, M. N. Dickson, A. A. Gorodetsky. "Sequence Specific Detection of Restriction Enzymes at DNA-Modified Carbon Nanotube Field Effect Transistors". *Anal. Chem.* **2014,** *86,* 8628–8633.
2. D. D. Ordinario, **L. Phan**, W. G. Walkup IV, J-M. Jocson, E. Karshalev, N. Hüsken, A. A. Gorodetsky. "Bulk Protonic Conductivity in a Cephalopod Structural Protein". *Nat. Chem.* **2014,** *6,* 596–602.
1. **L. Phan**, W. G. Walkup IV, D. D. Ordinario, E. Karshalev, J-M. Jocson, A. M. Burke, A. A. Gorodetsky. "Reconfigurable Infrared Camouflage Coatings from a Cephalopod Protein". *Adv. Mater.* **2013,** *25,* 5621–5625.

- Selected for the inside front cover feature

PATENTS

2. **L. Phan**, D. D. Ordinario, E. Karshalev, M. Shenk, W. G. Walkup IV, A. A. Gorodetsky. "Dynamic Infrared-Reflective Materials Based on Reflectin Films." U. S. Patent Application, Number US 14/723772, May 28, 2015.
1. **L. Phan,** D. D. Ordinario, W. G. Walkup IV, A. A. Gorodetsky. "Cephalopod Proteins as Proton Conductors." U. S. Patent Application, Number US 14/559414, December 3, 2014.

AWARDS AND HONORS

- 30+ accepted abstracts presented at 9 conferences (ACS, MRS, Pacifichem, etc.) Sept. 2011 – Nov. 2016
- UC Irvine Business Plan Competition, Institution for Innovation Tech Surge Award May 2015
- Best Oral Presentation, Advanced Healthcare Materials, Wiley-VCH March 2015
- Honorable Mention, NSF Graduate Research Fellows Program April 2013
- Henry Samueli School of Engineering Graduate Fellowship Sept. 2011 – May 2013

PROFESSIONAL MEMBERSHIPS

- American Chemical Society (ACS), Materials Research Society (MRS)

TECHNICAL SKILLS

Biological Techniques: Protein expression with BL21(DE3) E. coli, high pressure liquid chromatography (HPLC) for analysis and purification, immobilized metal-ion affinity chromatography (IMAC), cell culture, DNA miniprep

Biophysical Characterization: UV-Visible absorbance spectroscopy, fluorescence spectroscopy, circular dichroism (CD), dynamic light scattering (DLS), polyacrylamide gel electrophoresis (SDS-PAGE), tryptic digest and LC-MS/MS, MALDI

Cleanroom Techniques: Device microfabrication (e.g. MEMS, microfluidics, etc.), photolithography, soft lithography, wet etch, e-beam and thermal evaporation, nanoimprint lithography (NIL), atomic layer deposition (ALD), sputtering, spincoating

Materials Characterization: Atomic force microscopy (AFM), optical microscopy, scanning electron microscopy (SEM) with focused ion beam (FIB) milling, UV-Visible Near-Infrared spectroscopy, surface profilometry, tensile test (Instron), TGA

Electrical Characterization: DC measurements on 2 and 3 terminal devices, electrochemical impedance spectroscopy (EIS), semiconductor parameter analysis, organic materials testing, biomolecule sensing

Software/Programming: IGOR Pro, coding in Python and MATLAB, Photoshop, Illustrator, Gwyddion

OTHER ACTIVITIES

ChEMS Graduate Student Association, UC Irvine

Outreach Coordinator Sept. 2014 – Sept. 2015
Vice President, Materials Science and Engineering Sept. 2013 – Sept. 2014
Treasurer Sept. 2012 – Sept. 2013
First-Year Representative Jan. 2012 – Sept. 2012

UC Irvine Intramural Flag Football Fall 2011 – Fall 2016

UC Irvine Intramural Softball Spr. 2013 – Sum. 2015

ABSTRACT OF THE DISSERTATION

Cephalopod-Inspired Reflectin-Based Photonic Devices

By

Long Phan

Doctor of Philosophy in Materials Science and Engineering

University of California, Irvine, 2016

Professor Alon A. Gorodetsky, Chair

Cephalopods are known as the chameleons of the sea due to their remarkable camouflage abilities. They can rapidly and accurately tune their skin's coloration, pattern, and texture to blend into the surrounding environment. This dynamic camouflage capability stems from their transparent dermis/epidermis and the optically-active, protein-based nanostructures found in embedded skin cells known as leucophores, chromatophores, and iridophores. Respectively, these cells provide a high contrast reflective white background, mechanically actuated pigmented pixels, and chemically actuated Bragg reflectors that function in concert to modulate incident visible light. Considerable effort has been devoted to understanding and emulating cephalopod camouflage abilities in the visible region of the electromagnetic spectrum, but few studies have attempted to translate these principles to the infrared region for nighttime stealth applications. Thus, the fabrication of bio-inspired infrared-reflective devices for infrared camouflage remains an unexplored area of research.

To address this challenge, we have developed a high-throughput strategy for the gram-scale production, purification, and self-assembly of a unique cephalopod structural protein, reflectin. We eliminate time-consuming and costly steps commonly used in protein expression and

purification and instead replace them with rapid, sequential filtrations all while retaining high purity (>99%). Using this reflectin protein, we fabricate dynamically tunable biomimetic camouflage coatings with relevance to industrial and military applications. We demonstrate reversible control of reflectin film coloration shifts over a range of 1,200 nm from the visible into the near infrared using an acid vapor stimulus. We then coat reflectin on flexible, transparent substrates that can adhere to arbitrary surfaces, and modulate the film reflectance by mechanical strain or applied heat. Finally, we prove electrical actuation can also induce reversible color change in our films based on the applied bias. Together, our findings represent a key step towards the development of wearable biomimetic color and shapeshifting technologies that utilize diverse means of actuation. Future biophysical and materials studies lending insight into the tunability of reflectin-based Bragg reflector structures and textured reflectin surfaces could provide additional methods to enhance overall film brightness, angle-dependence, and color modulation for advanced camouflage applications.

CHAPTER 1 Dynamic Materials Inspired by Cephalopods

1.1: Abstract

The related concepts of disguising an object or physically changing it to resemble something entirely different have long captivated the human imagination. Although such notions are seemingly derived from fables and science fiction, cephalopods have perfected analogous capabilities over millions of years of natural evolution. Consequently, these invertebrates have emerged as exciting sources of inspiration for futuristic adaptive camouflage and shapeshifter-like technologies. Herein, we provide an overview of selected literature examples that have used cephalopods as models for the development of novel adaptive materials, devices, and systems. We in turn highlight some significant remaining challenges and potential future directions for such studies. Through this perspective, we hope to stimulate additional dialogue and continued scientific exploration within the area of cephalopod-inspired dynamic materials.

1.2 Introduction

The related concepts of adaptive camouflage (disguising an object in real time such that it cannot be detected) and shapeshifting (physically transforming an entity into something entirely different) have captivated the human imagination and influenced popular culture since classical antiquity.[1-4] For example, Greek and Roman mythology contained many famous examples of the ancient gods shapeshifting into animals or people, such as the tale of Vertumnus (Figure 1.1A) taking the form of an old woman in order to woo Pomona (Figure 1.1B).[1] The fascination with changing form continued throughout the Middle Ages, when lycanthropy (the transformation of a human into a wolf or wolf-like creature) emerged as a widespread theme in European folklore and superstition (Figure 1.1C).[2] In the modern era, such classic ideas have manifested themselves in

popular culture; for instance, the characters of Mystique and Beast from the X-men series of comic books and movies embody the concepts of adaptive camouflage and shapeshifting.[3,4] Although these notions once may have seemed fantastic, the accelerated pace of technological innovation has enabled scientists to envision materials, devices, and systems that would make such ideas a routine part of daily life.

Figure 1.1: A) Painting by Giuseppe Arcimboldo depicting Vertumnus, the Roman mythological god of seasons, who is able to alter his form at will. B) Painting by Paulus Moreelse, in which Vertumnus has changed form into an old woman to woo Pomona. C) Medieval woodcut by Hans Weiditz of a human who has transformed into a wolf and is attacking two men. Part A [Public Domain] was reproduced via Wikimedia Commons. Part B [Public Domain] was reproduced via Wikimedia Commons. Part C [Public Domain] was reproduced via Wikimedia Commons.

Remarkably, adaptive camouflage and shapeshifting reach beyond fables and science fiction—over millions of years of natural evolution, cephalopods (e.g., squid, octopuses, and cuttlefish) have developed and refined these capabilities for communication and disguise.[5-11] For example, Figure 1.2A shows a common octopus on a seaweed- and algae-covered rock.[10] The animal blends almost perfectly into its environment by matching the surrounding patterning, color, shape, and texture (Figure 1.2A, left) and only becomes clearly visible upon being disturbed (Figure 1.2A, right).[10] Other cephalopods, such as the squid in Figure 1.2B, are capable of equally striking feats.[11] When swimming in front of a rocky background, the squid nearly disappears due to its mottled and partially transparent skin (Figure 1.2B, left) and is only easily distinguishable when its skin turns dark and relatively uniform (Figure 1.2B, right).[11] Due to such visually stunning

demonstrations, cephalopods have emerged as an exciting source of inspiration for the development of color- and shape-changing technologies.

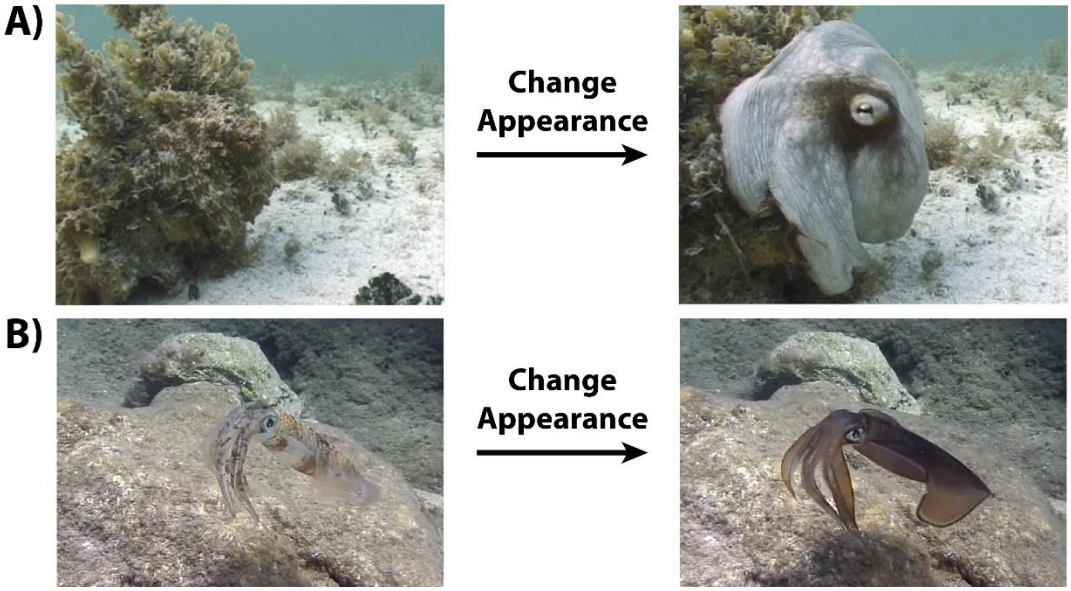

Figure 1.2: A) Camouflaged octopus positioned on a rock. The animal alters the coloration, texture, and morphology of its skin to match the surrounding environment, making it difficult to discern (left). When disturbed, the octopus changes its appearance and becomes visible (right). B) Squid with mottled and partially transparent skin, which is difficult to distinguish from the rock in the background (left). After the squid alters the coloration of its skin, the animal becomes clearly visible. Part A was reproduced with permission of Elsevier. Copyright 2007.

To understand (and ultimately emulate) the capabilities of cephalopods, it is instructive to consider their generalized skin architecture and morphology (note that the exact arrangement may vary among different species) (Figure 1.3). "Typical" cephalopod skin consists of multiple layers containing optically active cells known as leucophores, iridophores, and chromatophores (Figure 1.3A), which work in concert but possess distinct primary functions.[5,9] The leucophores serve as diffuse reflectors that scatter light, the iridophores serve as dynamic Bragg stacks that reflect light, and the chromatophores serve as size-variable spectral filters that absorb/transmit light (note that the specific cell types and their functionality also may vary among different species) (Figure 1.3B).[9,12-20] For some cephalopods, iridophores and chromatophores are controlled via an extensive network of embedded nerve fibers, which effectively multiplexes the cells and connects

them to the central nervous system.[5,9,16,20] Moreover, many cephalopods are capable of altering the physical form and shape of their skin, all without negatively affecting the embedded cells' optical functionality.[9,21-24] Thus, cephalopod skin essentially functions as a sophisticated three-dimensional adaptive display, with a combination of switchable vivid coloration, hierarchical multiplexing and pixelation, and precise shape and texture modulation that remains unrivaled both in the animal kingdom and among modern optical devices.

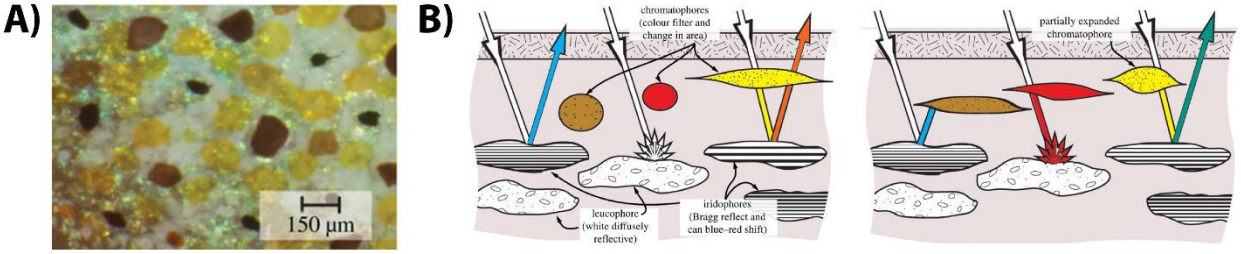

Figure 1.3: A) Picture of cuttlefish skin that shows leucophores (white), iridophores (green), and chromatophores (yellow, red, and dark brown). B) Diagram of "typical" cephalopod skin that illustrates the optical functionality of leucophores, iridophores, and chromatophores. The leucophores serve as diffuse white reflectors, the iridophores serve as dynamic Bragg reflectors, and the chromatophores serve as size-variable spectral filters. The picture shows two states on the left and the right (see the distinct cells and ray traces), exemplifying the sophisticated means by which cephalopods change their coloration. Parts A and B were reproduced with permission of The Royal Society. Copyright 2012.

In this perspective, we provide an overview of recent cephalopod-inspired studies, which can be viewed as preliminary steps toward realizing adaptive camouflage and shapeshifter-like technologies. First, we highlight various materials and devices that reversibly change their coloration. Subsequently, we describe integrated systems that are capable of sophisticated patterning. In turn, we present materials that alter both their color and texture/shape. Finally, we conclude with an overview of some potential applications and key remaining challenges. Here, we note that natural systems have evolved a fantastically diverse array of advanced photonic structures,[25-27] which have led to an impressive number of efforts seeking to understand and emulate their functionality.[28-30] As such, our perspective in no way constitutes an exhaustive review but rather presents specific excerpts from a limited number of selected case studies (which

all drew inspiration from cephalopods). Through our discussion of several illustrative examples, we hope to stimulate additional dialogue and further work in the exciting emerging area of cephalopod-inspired dynamic materials.

1.3 Switchable Coloration

Coloration changes in cephalopod skin are activated through a diverse combination of mechanisms. As one example, Figure 1.4A shows a schematic of a squid iridophore, which is actuated in part through a chemical stimulus.[14] The membrane of this cell folds to encompass platelets from a protein called reflectin, and these membrane-enclosed layers alternate with extracellular space to form Bragg reflector-like structures (Figure 1.4A). The reversible phosphorylation of reflectin induces platelet condensation/dehydration, changing the spacing, thickness, and refractive index of the layers and thus altering the dimensions of the Bragg reflectors.[14] This reversible process allows the iridophores to dynamically modulate their apparent color (Figure 1.4B).[14] As another example, Figure 1.4C shows a schematic of a cuttlefish chromatophore, which is actuated in part through a mechanical stimulus.[17] The cell is ringed by radial muscle fibers and encompasses sacs filled with a network of pigment granules, which contain pigments, reflectins, and crystallins (Figure 1.4C).[17] The muscle fibers expand the red, yellow, or brown chromatophores from barely visible spherical points to thin colored plates, altering the architecture, absorbance, and luminescence of the embedded granule network and enabling the cells to serve as spectral filters (Figure 1.4D).[17] The functionality of both of these cell types makes them attractive as models for artificial color-changing materials, devices, and systems.

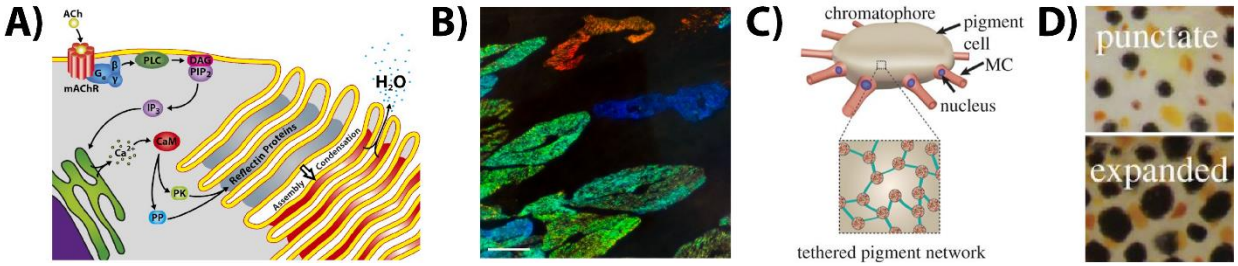

Figure 1.4: A) Illustration of an iridophore and its associated membrane-enclosed reflectin platelets, which alternate with extracellular space to form biological Bragg reflectors. The geometry and optical properties of the reflectors are modulated through a sophisticated signaling cascade. B) Microscope image of squid iridophores with different colorations. C) Illustration of a chromatophore and its internal tethered pigment granule network. The architecture and optical properties of the pigment network are controlled by the radial muscle fibers. D) A picture of cuttlefish chromatophores in their punctate (dot-like) and expanded states. Parts A and B were reproduced with permission of the National Academy of Sciences, USA. Copyright 2013. Parts C and D were reproduced with permission of The Royal Society. Copyright 2014.

Kramer and co-workers drew inspiration from reflectin platelets in iridophores and studied protein-based thin films and microstructures.[31] For this purpose, the authors used the protein reflectin, which had been shown to play a crucial role in the optical functionality of iridophores.[14,15] Figure 1.5A illustrates the general film fabrication procedure, which entailed flow coating reflectin with a blade onto an underlying substrate. The process yielded films for which the coloration was determined by their thickness and thin film interference (Figure 1.5B,C). The authors demonstrated that water vapor-induced swelling reversibly modulated the films' coloration, albeit across a relatively narrow range. Furthermore, the authors self-assembled reflectin into fibers and diffraction gratings, which held potential for more advanced photonic applications. These seminal experiments highlighted the promise of materials that occur naturally in cephalopods for applications in dynamic color-changing optical devices.

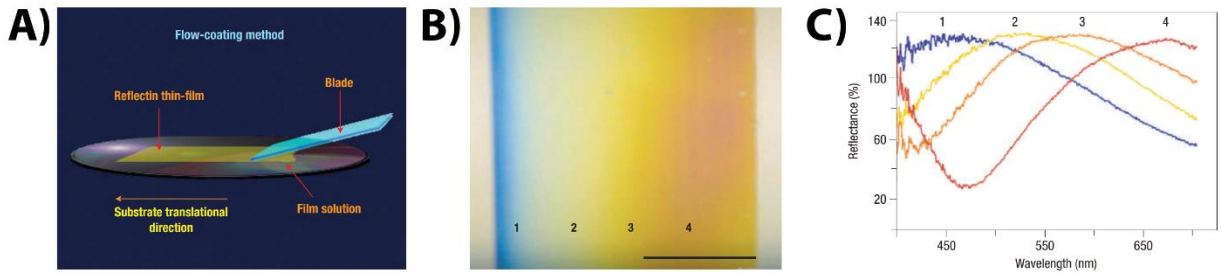

Figure 1.5: A) Procedure for flow coating reflectin films onto hard substrates. B) Reflectin film that featured a thickness gradient, which was produced by adjusting the tilt of the blade during fabrication. C) Corresponding reflectance spectra for the different regions of the film in part B. Note that the reflectance of the film was dictated by thin film interference. Parts A, B, and C were reproduced with permission of Macmillan Publishers Ltd.: Nature Materials. Copyright 2007.

Phan and co-workers also drew inspiration from reflectin platelets in iridophores and investigated protein-based color-changing coatings on hard substrates (in analogy to the work of Kramer and co-workers).[32] Figure 1.6A illustrates the general film fabrication procedure, which consisted of functionalizing the substrate with graphene oxide and then covering the surface with the stimuli-responsive protein reflectin. The process yielded films like the one shown in Figure 1.6B, for which the apparent color was dictated by the thickness. The authors next modulated the films' coloration through exposure to acetic acid vapor, which induced substantial swelling due to changes in intraprotein electrostatic interactions (Figure 1.6C). By controlling this chemical stimulus, the authors were able to reversibly tune the films' reflectance across the entire visible spectrum and even into the near-infrared (Figure 1.6D). Notably, the films functioned as a rudimentary form of active infrared camouflage, disguising objects from visualization under illumination with infrared light. These experiments demonstrated functionality not necessarily intended by nature, as well as a large dynamic coloration range, for protein-based coatings.

Phan and co-workers subsequently followed up on their initial experiments and studied color-changing coatings on conformable adherent substrates.[33] The authors first adapted their fabrication procedures for flexible substrate materials, forming reflectin films on graphene oxide-coated fluorinated ethylene propylene tape (Figure 1.7A). In turn, they applied the tape to standard camouflage fabrics as stickers, which were relatively difficult to distinguish from the background (Figure 1.7B). The initial unactuated stickers were transparent and featured peak reflectances in the near-infrared (Figure 1.7C). However, upon mechanical actuation (uniaxial stretching), the thickness of the tape and the overlaid reflectin films decreased due to the Poisson effect (Figure

1.7D). The actuated stickers thus acquired an opaque orange color (Figure 1.7E) and featured peak reflectances in the visible (Figure 1.7F), making them straightforward to identify. Here, the authors again used their systems as active infrared camouflage, noting the stickers' potential deployment flexibility. These experiments represented a straightforward method for the integration of simple mechanically actuated systems with fabrics.

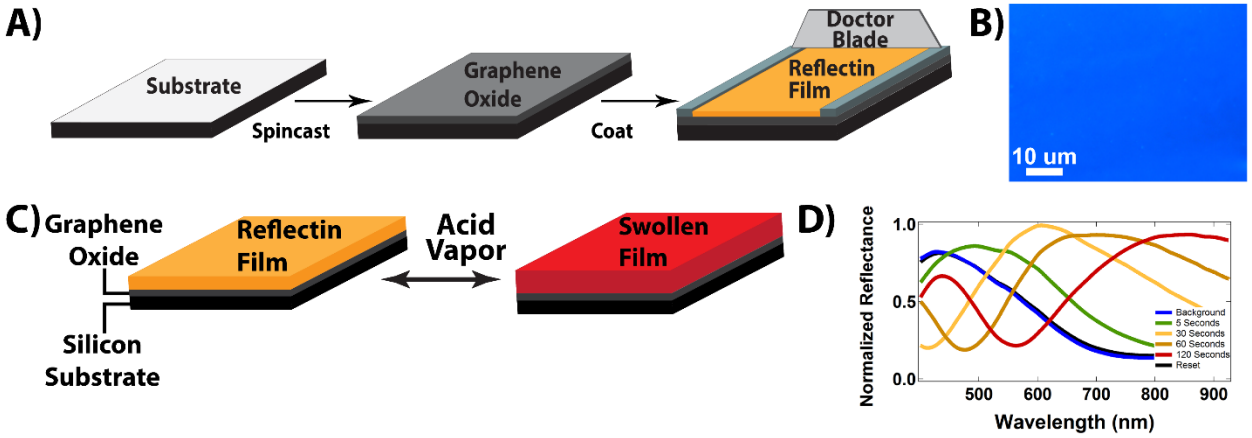

Figure 1.6: A) Procedure for fabrication of reflectin films on graphene oxide-modified substrates via doctor blading. (B) Representative optical image of a reflectin film, for which the color and reflectance were dictated by thin film interference. C) Change in thickness induced by acetic acid vapor for a reflectin film. D) Change in reflectance for a reflectin film as a function of time following the application of acetic acid vapor. Note that the initial reflectance spectrum could be recovered through removal of the acidic stimulus. Parts A–D were reproduced with permission of WILEY-VCH Verlag GmbH & Co. KGaA, Weinheim. Copyright 2013.

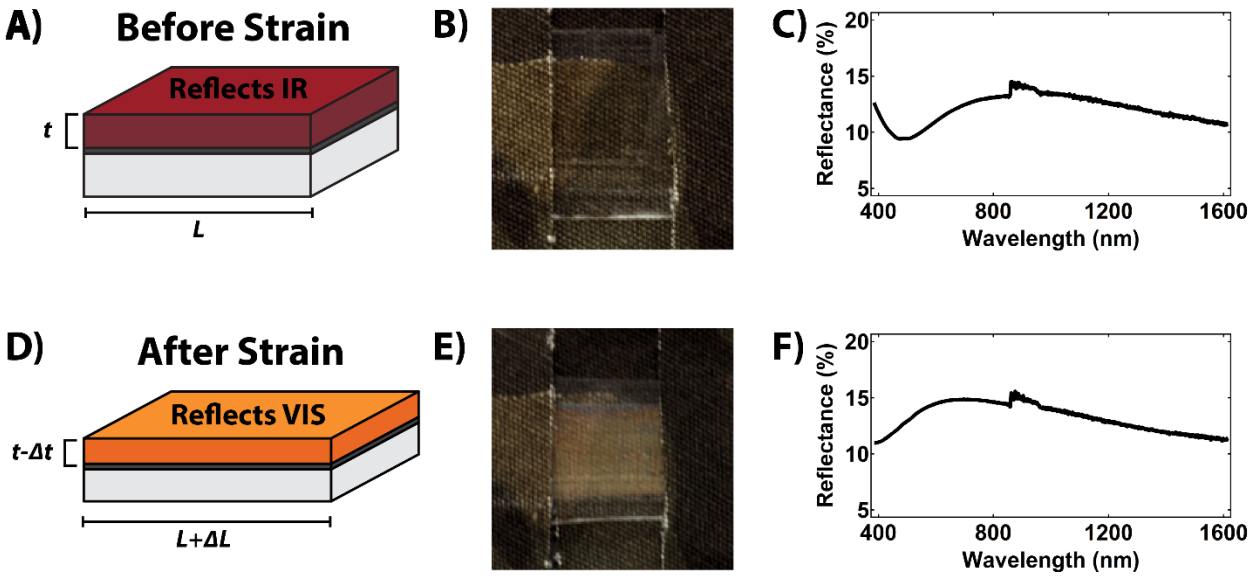

Figure 1.7: A) Schematic of reflectin-coated tape in the absence of strain. B) Optical camera image of a camouflage fatigue overlaid with reflectin-coated tape, which was transparent in the absence of strain. C) Corresponding reflectance spectrum for the film in part B. D) Schematic of reflectin-coated tape in the presence of strain. The application of a uniaxial strain to the tape altered the dimensions of the overlaid reflectin film. E) Optical camera image of the camouflage fatigue from part B after the application of strain to the reflectin-coated tape. Note that the tape acquired an orange color and became opaque. F) Corresponding reflectance spectrum for the film in part E, demonstrating a shift in the reflectance. Parts A–F were reprinted from ref 27.

Wang and co-workers drew inspiration from the mechanical actuation of chromatophores and investigated elastomers with mechanoresponsive coloration (in an approach analogous to the one of Phan and co-workers).[34] The authors prepared cross-linked silicone elastomers containing the covalently attached mechanophore spiropyran. In the absence of a mechanical stimulus, the elastomers possessed a pale yellow color (Figure 1.8A, left). However, the application of a sufficient uniaxial strain induced a ring-opening reaction, transforming the spiropyran to a merocyanine and changing the color of the elastomers to blue (Figure 1.8A, middle). The relaxed elastomers were returned to their original state through irradiation with green light, which induced a ring-closing reaction and converted the merocyanine back to a spiropyran (Figure 1.8A, right). Notably, due to the fluorescence of the embedded molecules, the authors were able to monitor the entire reversible conversion process with fluorescence microscopy (Figure 1.8B). These experiments showcased the coupling of mechanical and chemical effects for the induction of coloration changes in elastomeric materials.

Rossiter and co-workers also drew inspiration from the mechanical actuation of chromatophores and studied polymer-based artificial variants of these cells (in another analogous strategy).[35] The authors fabricated their devices from dielectric elastomers, a class of materials for which the application of an electric field induces transverse thickness compression and planar areal expansion.[35,36] The artificial chromatophores consisted of a clear polyacrylate dielectric elastomer layer sandwiched by two transparent, compliant electrodes and overlaid with a blue-colored soft gel (Figure 1.9A). Prior to electrical actuation, the appearance of the device was dictated by the

initial size of the electrodes and the color of the overlaid gel (Figure 1.9B, left), but after electrical actuation, the appearance of the device was determined by the applied transverse electric field, which increased the electrode active area and reduced the gel color intensity (Figure 1.9B, right). These experiments constituted an initial demonstration of cephalopod-inspired devices that were controlled electrically.

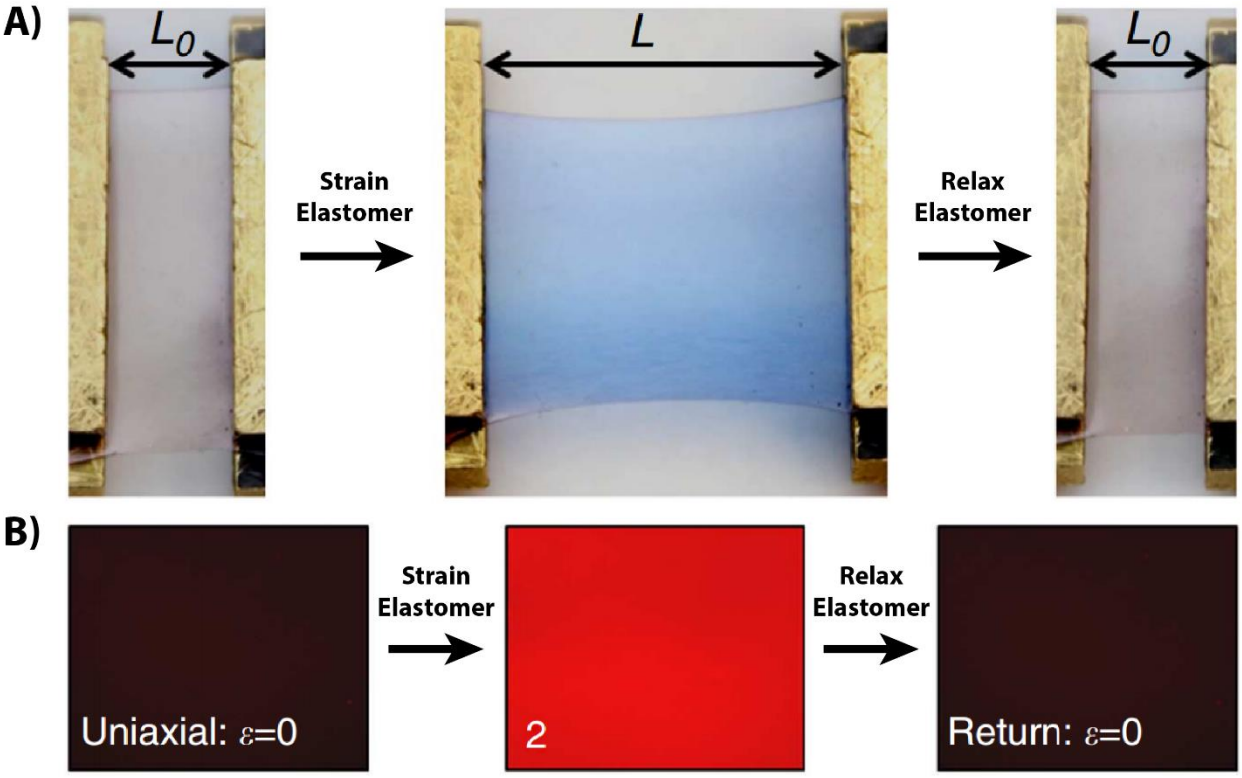

Figure 1.8: A) Optical image of a silicone elastomer that contained covalently attached spiropyran mechanophores in the absence of an applied strain (left), under a uniaxial strain of 200% (middle), and after relaxation and illumination with green light (right). The applied strain caused a change in the coloration of the elastomer from pale yellow to blue, due to conversion of the spiropyrans into merocyanines. The relaxation of the strain and exposure to green light returned the mechanophores to their original state, as well as returned the coloration of the elastomer to yellow. B) Fluorescence microscope images of the film corresponding to the three situations in part A, revealing the fluorescence of the merocyanines (middle). Parts A and B were reproduced with permission of Macmillan Publishers Ltd.: Nature Communications. Copyright 2014.

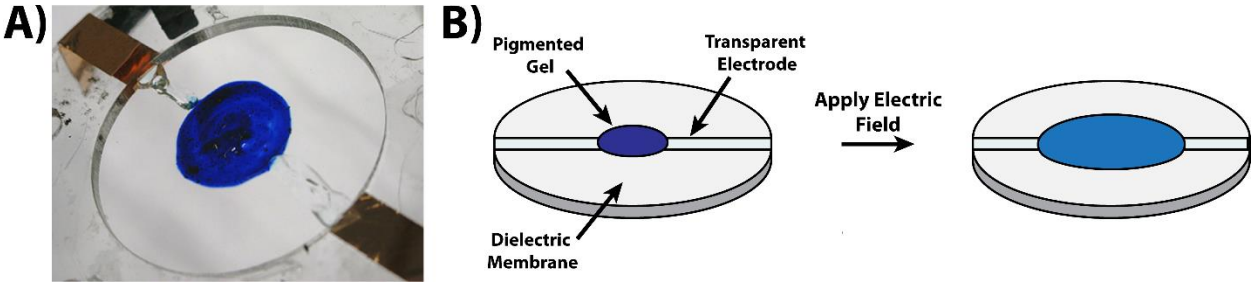

Figure 1.9: A) Image of a single artificial chromatophore, which was composed of a transparent dielectric elastomer layer stretched over a frame, partially sandwiched between two transparent electrodes, and overlaid with a blue-colored gel. B) Schematic of the artificial chromatophore, for which the application of an electric field induced a change in both the geometry of the electrode and the color intensity of the overlaid gel. Part A was reproduced with permission of IOP Publishing. Copyright 2012.

1.4 Hierarchical Multiplexing and Pixelation

Many cephalopods control the appearance of their skin at both the local and global levels via an interconnected network of embedded nerve fibers.[5,9,16,20] As an example, Figure 1.10A shows a fluorescence microscopy image of squid fin skin, for which the nerve fibers are stained red with a fluorescent dye.[20] The image clearly demonstrates that the nerves are highly branched and situated near the iridophores and chromatophores (or even contact them directly). Remarkably, direct electrical stimulation of the nerves triggers coloration changes for the innervated cells, as shown for both individual iridophores (Figure 1.10B) and entire iridophore clusters (Figure 1.10C).[20] Thus, the nerve fibers effectively serve to multiplex the three-dimensional network of color-changing elements that comprise the skin. Consequently, the general strategy squid employ to hierarchically modulate the appearance of their skin holds appeal for applications in autonomous multiplexed systems from independently addressable color-changing elements.

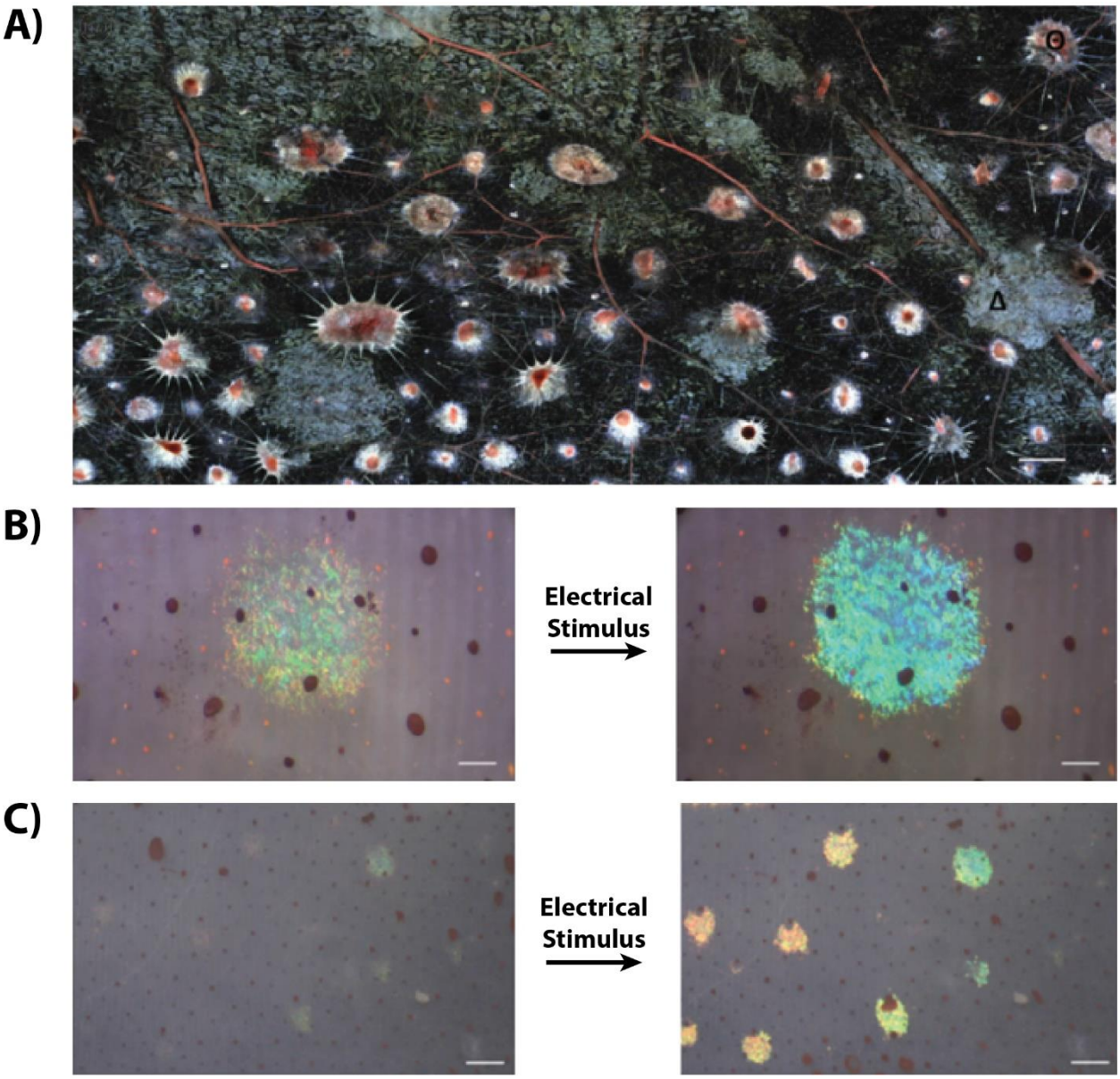

Figure 1.10: A) Fluorescence image of innervated squid skin with the nerve fibers stained red. Note the proximity of the nerve fibers to the chromatophores and iridophores. B) Example of a squid iridophore before (left) and after (right) nerve electrical stimulation. Note the change in color for the cell. C) Example of a squid fin iridophore cluster before (left) and after (right) electrical stimulation of the fin nerve. Note the change in color for the cell cluster. Parts A, B, and C were reproduced with permission of The Royal Society. Copyright 2012.

Rossiter and co-workers built upon their earlier experiments and investigated the optical functionality of devices from multiple artificial chromatophores.[36] Thus, the authors fabricated more advanced devices, which consisted of three distinct dielectric elastomer layers partially sandwiched by either red, green, or blue pigmented electrode areas and stacked on top of one

another (Figure 1.11A). For this cluster or pixel configuration, the layers could be addressed and electrically actuated independently. As an example, Figure 1.11B shows a schematic of a device that was cycled between different coloration states, wherein the green and blue layers were actuated (Figure 1.11B, top), the red and green layers were actuated (Figure 1.11B, bottom left), and only the blue layer was actuated (Figure 1.11B, bottom right). The authors modeled the coloration of such clusters when integrated into a large array, spaced precisely apart, multiplexed for arbitrary electrical triggering, and viewed from a distance. The theoretical modeling indicated that arrayed pixels would be capable of generating a wide range of colors. These experiments laid a conceptual foundation for the preparation of systems that use only simple elements to mimic a broad color palette.

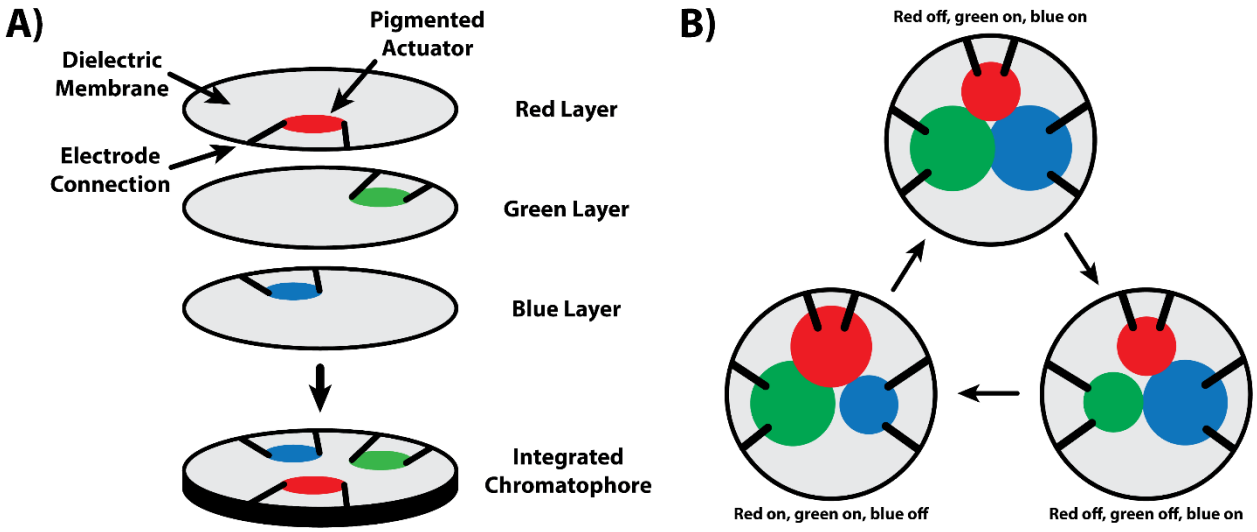

Figure 1.11: A) Schematic of a device that featured artificial chromatophores within multiple independent stacked layers. The three layers contained red (top), green (middle), and blue (bottom) electrode areas. Note that the layers could be electrically actuated independently. B) Schematic of a device for which the green and blue layers were actuated (top), the red and green layers were actuated (bottom left), and only the blue layer was actuated (bottom right). These figures are an artistic rendition of the schematics from ref 30.

Morin and co-workers drew inspiration from the global color-changing abilities of cephalopod skin and studied a sophisticated integrated system that was capable of concealment in diverse settings.[37] For this purpose, the authors fabricated elastomer layers containing distinct

networks of independently addressable microfluidic channels (Figure 1.12A). Through injection of different liquids into the channels, the layers' coloration and patterning could be changed in a predetermined fashion; Figure 1.12B,C,D shows the appearance of a layer for which one channel was filled with a red dye solution, one channel was filled with a blue dye solution, or two different channels were filled with red and blue dye solutions. The authors also demonstrated that layers filled with appropriate dye dispersions were capable of matching various backgrounds, such as rocks (Figure 1.12E). Moreover, through injection of solutions with controlled temperatures, the layers could be induced to either blend into or stand out against their thermal environments (Figure 1.12F). Notably, by integrating the microfluidic layers with pneumatically actuated soft robots, the authors manufactured mobile systems that exhibited camouflage capabilities. For example, Figure 1.12G shows a robot among leaves before being filled with a dye solution (when it is clearly visible), as well as the same robot after being filled with a dye solution (when it is more difficult to discern from the background). Together, these experiments constituted a substantial advance with regard to mobile systems that adaptively emulate a wide range of environments.

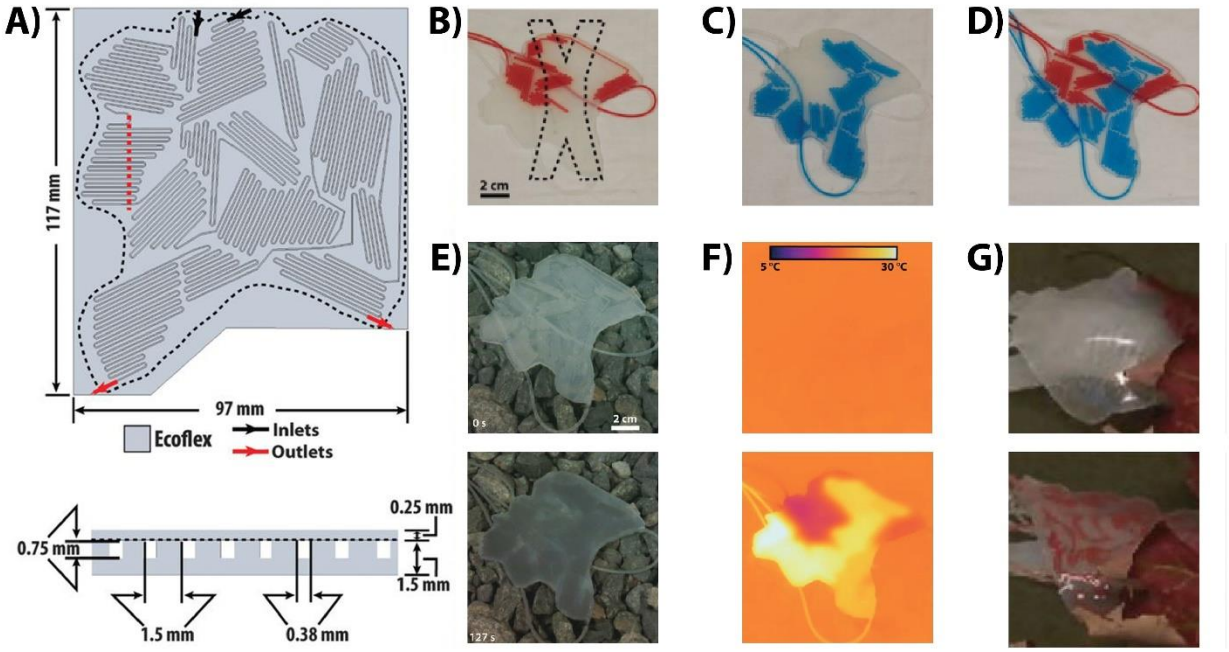

Figure 1.12: A) Schematic of the top and side views of an elastomer layer that contained two different microfluidic channel networks. B) Image of the layer from part A, for which one channel was filled with a red dye solution. C) Image of the layer from part A, for which one channel was filled with a blue dye solution. D) Image of the layer from part A, for which different channels were filled with red and blue dye solutions. E) Images of a microfluidic layer before (top) and after (bottom) injection of dye dispersions with different gray shades. The dispersions allowed the layer to match the appearance of the background rocks. F) Infrared camera images of the microfluidic layer from part E before (top) and after (bottom) injection of dye dispersions with different temperatures. The dispersions allowed the layer to stand out from its thermal environment. G) Images of an elastomer layer that was integrated with a pneumatically actuated soft robot. The robot was clearly distinguishable from a red leaf background before injection of a dye solution (top) and blended into the red leaf background after injection of a dye solution (bottom). Parts A–G were reproduced with permission of The American Association for the Advancement of Science. Copyright 2012.

Larson and co-workers drew inspiration from the architecture of cephalopod skin and investigated soft multipixel electroluminescent display-like sheets.[38] Thus, the authors first designed and fabricated hyperelastic light-emitting capacitors, which consisted of a phosphor-containing layer sandwiched between two ionically conducting polyacrylamide electrodes and encapsulated within a silicon housing (Figure 1.13A). Subsequently, the authors used replica molding to fabricate sheets containing arrays of such devices (Figure 1.13B,C). For these arrays, the emission of light was induced through the selective application of alternating current electric fields to independent pixels in distinct areas, enabling control over the sheets' patterning and appearance. As an example, Figure 1.13C,D,E shows sheets for which eight by eight, six by six,

and three by three arrayed pixel subsets have been actuated. Here, the use of different phosphors in the electroluminescent layers made it straightforward to fabricate devices with distinct colorations; Figure 1.13B,C shows different sheets from phosphors that emit blue and orange light. These experiments constituted an exciting example of soft devices that possessed spatiotemporally patternable coloration and appeared amenable to integration with more advanced systems.

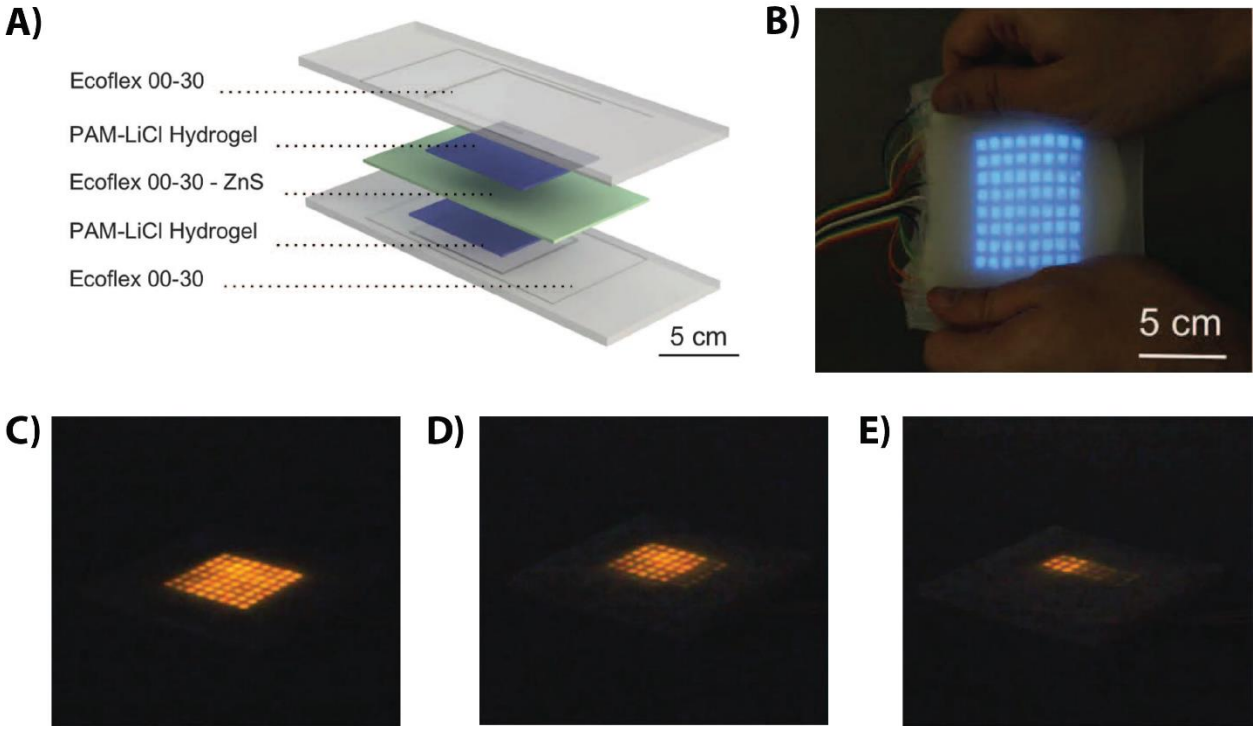

Figure 1.13: A) Schematic of a hyperelastic light-emitting capacitor, which consisted of an electroluminescent phosphor-containing layer sandwiched between two ionically conducting polyacrylamide electrodes and encapsulated in a flexible silicon housing. B) Picture of a multipixel display composed of arrayed capacitors. The display emitted blue light upon application of an electric field (actuation). C) Picture of a multipixel display comprised of arrayed capacitors. The entire eight by eight pixel array was actuated and emitted orange light. D) Picture of the display from part C, for which a six by six subset of the pixel array was actuated and emitted orange light. E) Picture of the display from part C, for which a three by three subset of the pixel array was actuated and emitted orange light. Parts A–E were reproduced with permission of The American Association for the Advancement of Science. Copyright 2016.

Yu and co-workers also drew inspiration from the hierarchical multilayer architecture of cephalopod skin and studied the properties of multiplexed optoelectronic systems.[39] The authors therefore designed multilayer unit cells, for which an exploded view schematic is illustrated in Figure 1.14A and corresponding optical images are shown in Figure 1.14B,C,D,E. These unit cells

consisted of a thermochromic color-changing dye embedded in a polymer matrix, in analogy to a chromatophore (Figure 1.14B); a thin silver layer as a bright white background, in analogy to a leucophore (Figure 1.14C); a silicon diode heating element as an actuator, in analogy to the chromatophores' muscle fibers (Figure 1.14D); and a silicon photodiode as a light sensor, in analogy to photoresponsive opsin-containing functional units (Figure 1.14E). The authors fabricated multilayer, multiplexed arrays composed of the unit cells on flexible polymeric support substrates; an exploded view schematic of the arrays is illustrated in Figure 1.14F, and a corresponding optical image is shown in Figure 1.14G. Through controlled localized heating of the thermochromic color-changing elements, the final integrated systems were capable of producing arbitrary black and white patterns. As an example, Figure 1.14H shows an array that was programmed to display the text "UoI." Notably, such arrays maintained their functionality even under mechanical deformation and possessed angle-independent coloration. Furthermore, the authors demonstrated that the integrated systems were able to autonomously sense exogenous stimuli, i.e., incident light, and appropriately adapt their appearance, i.e., change coloration. For instance, Figure 1.14I shows an array that was illuminated with light in different areas—the stimulus was detected by the photodiodes and transduced into localized color changes (from black to white) via heating of specific elements. Overall, these experiments represented a key innovative step forward for multiplexed systems that could exhibit fully autonomous operation.

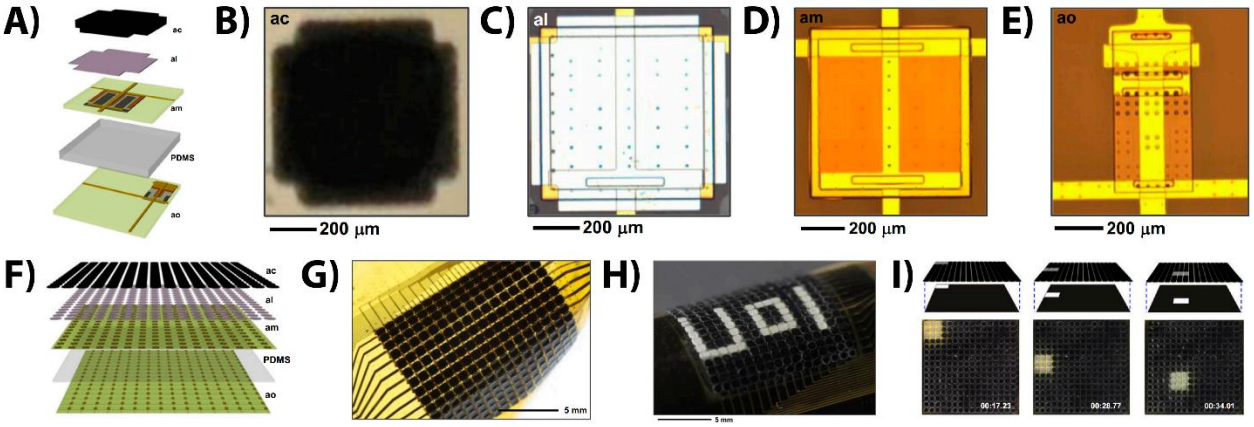

Figure 1.14: A) Schematic of a multilayer unit cell that incorporated essential design features found in cephalopod skin. The unit cells consisted of a thermochromic color-changing dye embedded in a polymer matrix, in analogy to a chromatophore; a thin silver layer as a bright white background, in analogy to a leucophore; a silicon diode heating element as an actuator, in analogy to the chromatophores' muscle fibers; and a silicon photodiode as a light sensor, in analogy to photoresponsive opsin-containing functional units. B) Optical image of a thermochromic equivalent to a chromatophore. C) Optical image of the silver layer and the silicon diode. D) Optical image of the diode. E) Optical image of a photodiode and an associated blocking diode for multiplexing. F) Illustration of an interconnected unit cell array in a complete artificial adaptive camouflage skin. G) Optical image of an interconnected unit cell array in a complete artificial adaptive camouflage skin. H) Image of a bent device that was actuated to display the text "UoI." I) Schematics and corresponding optical images of devices that were illuminated with light, which stimulated the photodiodes and induced a local coloration change from black to white. As a shadow mask moved the light to different locations, the artificial camouflage skins were able to independently adapt their pattern to match the constantly changing position of the incident light. Parts A–I were reproduced with permission of the National Academy of Sciences, USA. Copyright 2014.

1.5 Shape and Texture Modulation

Cephalopods' flexible and deformable skin allows these animals to contort their body and appendages into seemingly arbitrary geometries and positions.[21-24] As one example, Figure 1.15A shows a common octopus attempting to grab a piece of bait in a glass tube.[24] When reaching for the bait, the octopus elongates an outstretched arm by a factor of 2 or more, demonstrating the intrinsic stretchability of its skin.[24] As another example, Figure 1.15B shows a picture of a common octopus' eye and the surrounding smooth skin.[22] To match its surroundings, the octopus extends small rounded protuberances known as papillae, causing the skin to appear textured.[22] Such mechanical properties make cephalopod skin unique in the animal kingdom and highly attractive as a prototype for systems with reconfigurable shapes and textures.

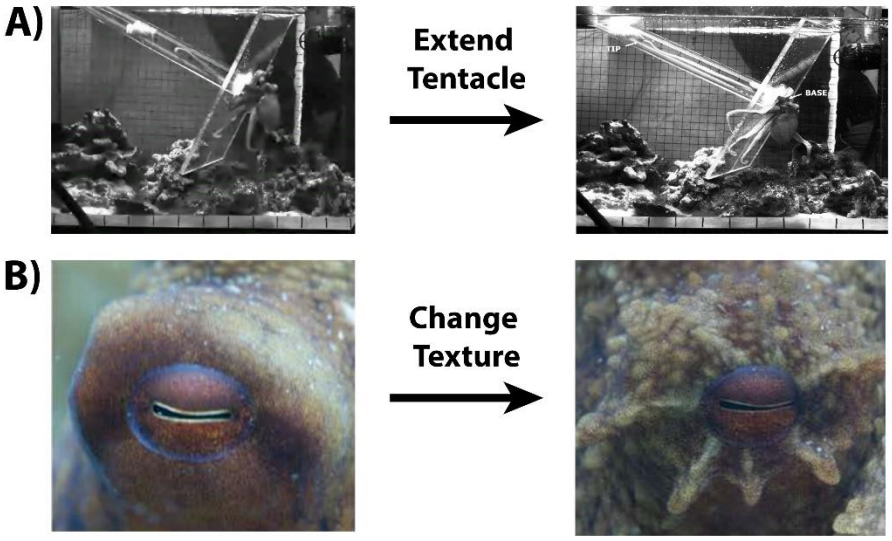

Figure 1.15: A) Picture of an octopus and bait positioned at opposite ends of a glass tube, with the animal reaching for the bait (left). After the bait is moved farther away, the octopus attempts to secure the bait by substantially elongating its arm to twice the original length (right). B) Picture of an octopus with flat skin around its eye (left). The octopus extends papillae to texture the skin (right). Part A was reproduced with permission of Elsevier. Copyright 2013. Part B was reproduced with permission of Wiley Periodicals, Inc. Copyright 2013.

Rossiter and co-workers drew inspiration from multiple types of cephalopod skin cells and investigated "inverted" artificial chromatophore/iridophore variants.[35] The authors therefore fabricated devices consisting of a dielectric elastomer layer sandwiched by annular carbon grease electrodes and overlaid with a blue-colored gel in the region lacking electrodes (Figure 1.16). In the absence of an applied electric field, the gel-covered central area possessed a specific size/thickness and color intensity, and the surrounding electrode was relatively smooth (Figure 1.16A, left and Figure 1.16B, left). However, in the presence of an applied electric field, the central region changed its size/thickness and corresponding color intensity, and the surrounding electrode displayed radial buckling or wrinkling (Figure 1.16A, right and Figure 1.16B, right). These experiments represented an early proof-of-principle demonstration of the simultaneous modulation of the macroscopic texture and color for cephalopod-inspired devices.

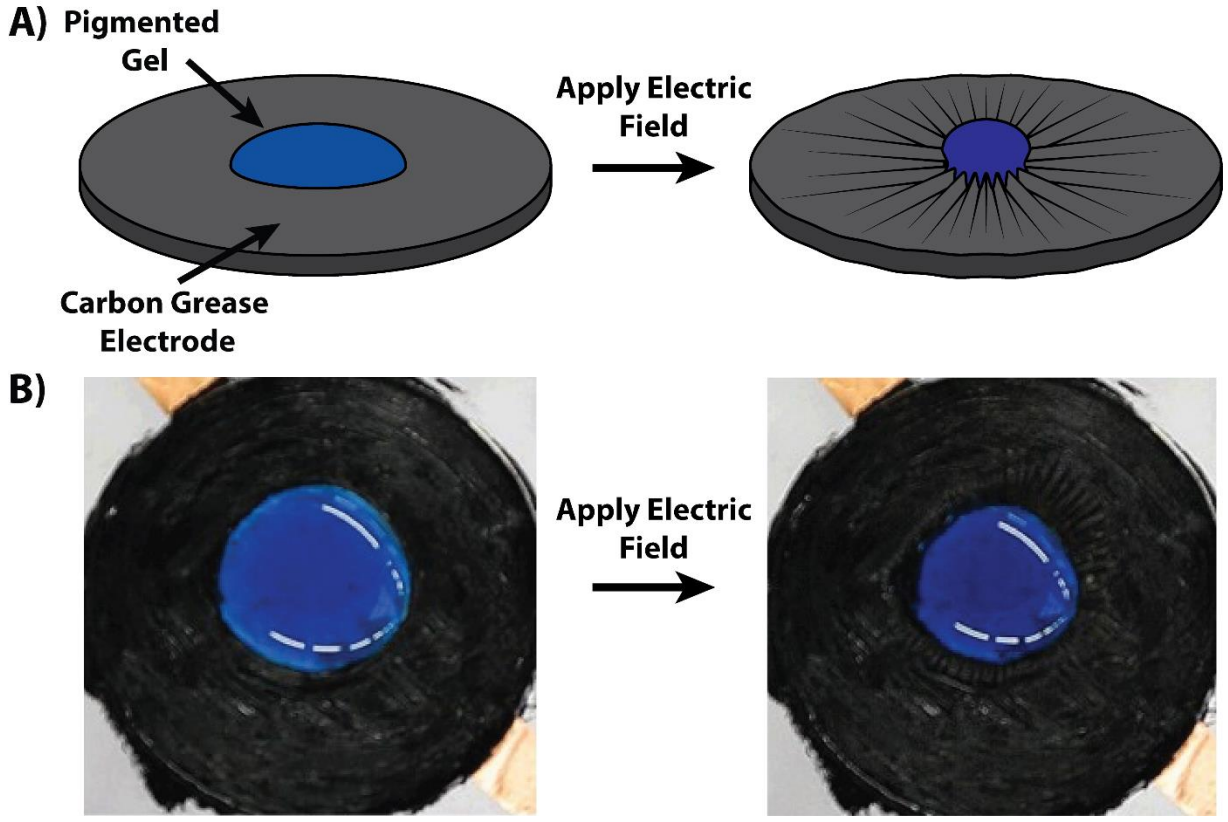

Figure 1.16: A) Schematic of an "inverted" artificial chromatophore, which consisted of a central region overlaid with a blue-colored gel layer and surrounded by an annular electrode (left). The application of an electric field induced a change in the geometry and color intensity of the central region, as well as radial buckling/wrinkling of the surrounding electrode's surface (right). B) Image of an "inverted" artificial chromatophore before (left) and after (right) electrical actuation. The device displayed a change in geometry and color intensity for the central region, as well as radial buckling/wrinkling of the surrounding electrode upon application of an electric field. Part B was reproduced with permission of IOP Publishing. Copyright 2012.

Wang and co-workers drew inspiration from the general optomechanical properties of cephalopod skin and used electromechanochemically responsive elastomers in electrically actuated systems with advanced microscale patterning capabilities.[34] For this purpose, the authors designed and fabricated multilayer structures, which consisted of a thin metal foil, a rigid protective insulator, a buffer elastomer layer, an electromechanochemically responsive elastomer layer, and a conductive salt solution electrode (Figure 1.17A). In the absence of applied electric fields, the surfaces of such devices were flat, but upon application of electric fields above material-specific critical values, the surfaces became unstable and formed patterns of micrometer-size

wrinkles (Figure 1.17B). For even larger applied electric fields, the valleys between the wrinkles were pressed down, forming craters (Figure 1.17C). As an example, Figure 1.17D shows an optical image of an initially flat electromechanochemically responsive elastomer layer for which an applied electric field had triggered the formation of a pattern of craters (note that the surface recovered its flat state once the stimulus was removed). Notably, the authors demonstrated that larger electric fields induced more substantial deformation around the crater edges and an associated local activation of fluorescence for the spiropyran mechanophores, leading to controllable changes in the effective coloration of the layer (Figure 1.17E). Furthermore, the authors showed that prestretching the electromechanochemically responsive elastomer films produced patterns of trenches (Figure 1.17F) and that embedding U-shaped obstacles within the buffer layers reproduced their underlying geometries on the surface (Figure 1.17G). Altogether, these experiments demonstrated a strategy for the localized rational programming and patterning of microscopic texture and color for cephalopod-inspired systems.

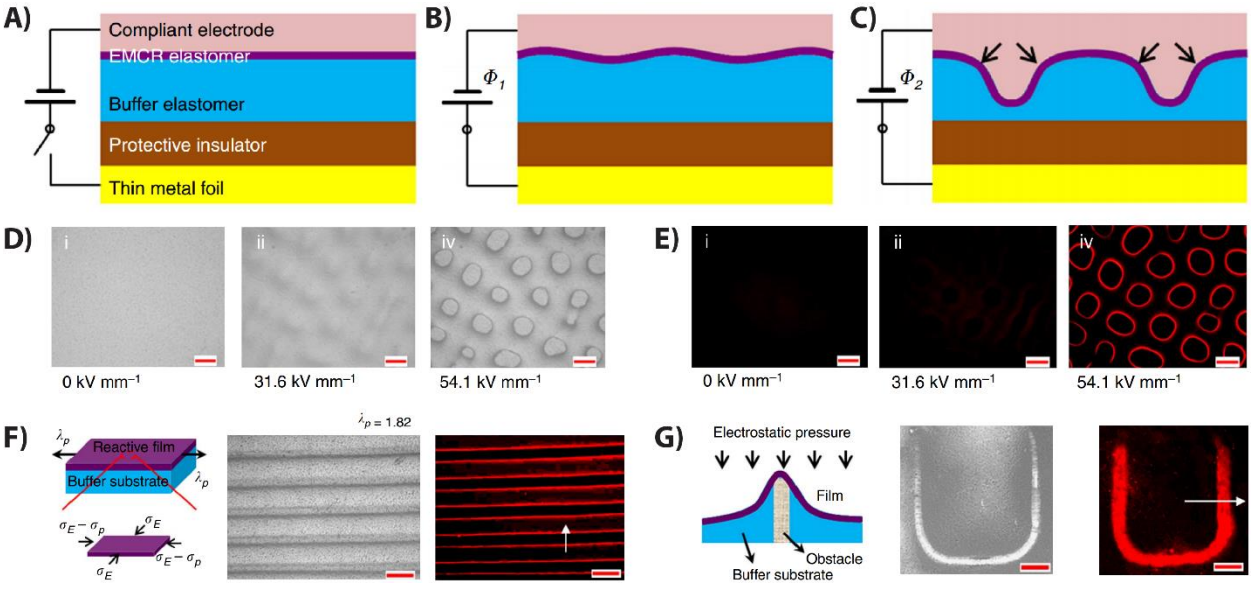

Figure 1.17: A) Schematic of the electromechanochemically responsive structure, which consisted of a thin metal foil, a rigid protective insulator, a buffer elastomer layer, an electromechanochemically responsive elastomer layer, and a conductive salt solution electrode. B) Schematic of the structure from part A, for which the application of electric fields above material-specific critical values led to the formation of wrinkles. C) Schematic of the structure from part A, for which the application of even larger electric fields led to the formation of craters. D) Optical microscope images

of an initially flat elastomer layer, for which applied electric fields of increasing magnitude induced surface texturing (the formation of craters). E) Fluorescence microscope images of the layer from part D showing that deformation around the crater edges locally converted the spiropyrans to fluorescent merocyanines. F) Schematic of a prestretched electromechanochemically responsive elastomer film (left). An optical microscope image of a prestretched film for which an electric field induced the formation of trenches (middle). A fluorescence microscopy image of the prestretched film demonstrating that the edges of the trenches were fluorescent (right). G) Schematic of an electromechanochemically responsive elastomer film with an obstacle embedded in the underlying buffer substrate (left). An optical microscope image of the film for which an electric field induced deformation along the contour of the obstacle (middle). A fluorescence microscopy image of the deformed film demonstrating that the edges of the obstacle were fluorescent (right). Parts A–G were reproduced with permission of Macmillan Publishers Ltd.: Nature Communications. Copyright 2014.

Larson and co-workers drew inspiration from the general malleability of octopus skin and investigated the functionality of their display-like sheets under substantial deformation.[38] Here, the authors employed both single- and multipixel variants of the hyperelastic light-emitting capacitors. As one example, Figure 1.18A shows a single-pixel capacitor in its initial and stretched states; the device continued operating under tension, with a predictable increase in the intensity of the emitted light. As another example, Figure 1.18B,C,D shows multipixel display-like sheets that were wrapped around a finger, bent, or rolled. Such patterned analogues of the stretchable devices maintained their normal functionality, i.e., light emission, even when subjected to different types of mechanical deformation. Moreover, deformation did not appear to affect localized triggering of device coloration changes via selective regional application of electric fields (Figure 1.18E). These experiments demonstrated the modulation of both global shape and appearance with independent orthogonal stimuli for cephalopod-inspired devices.

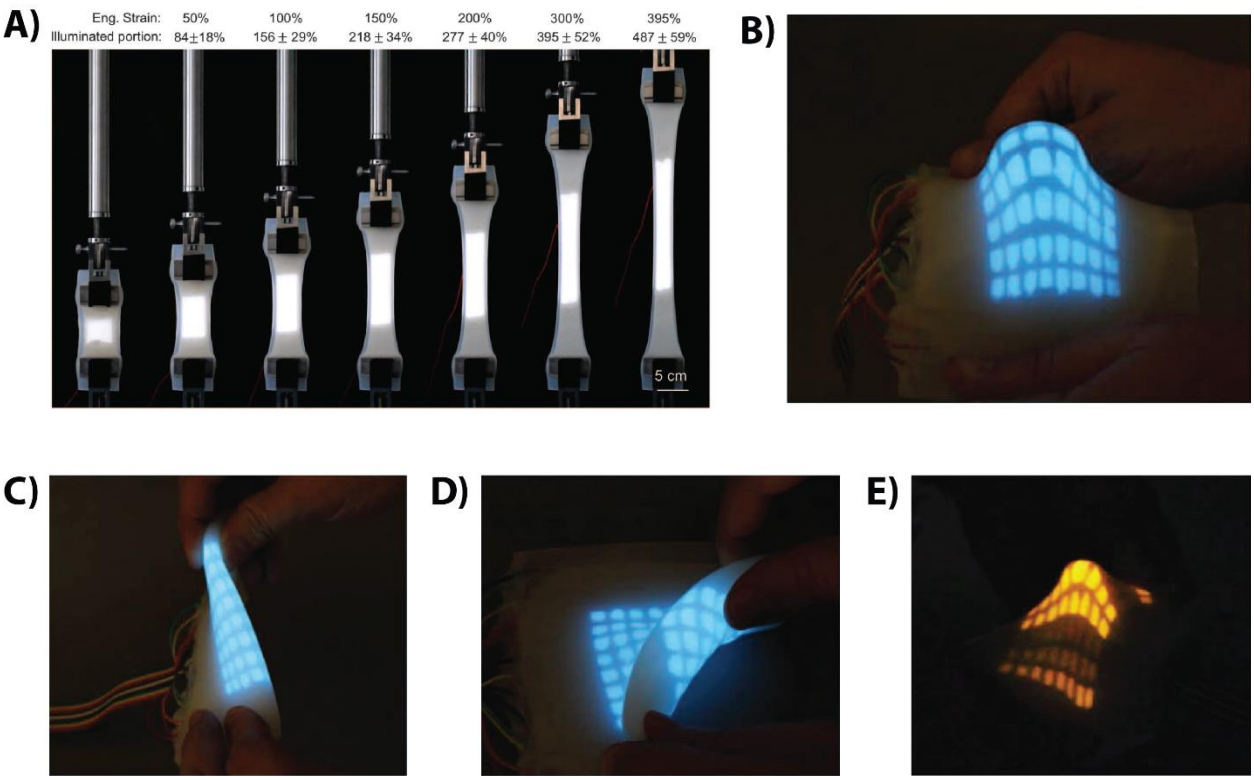

Figure 1.18: A) Optical images of a hyperelastic light-emitting capacitor under different applied engineering strains. As the device was stretched to approximately five times its original length (left to right), the functionality was maintained, and the intensity increased in predictable fashion. B) Multipixel blue light-emitting display that was deformed by wrapping around a finger. C) Multipixel blue light-emitting display that was deformed by folding. D) Multipixel blue light-emitting display that was deformed by rolling. E) Deformed multipixel orange light-emitting display for which a subset of its pixels was actuated. Parts A–E were reproduced with permission of The American Association for the Advancement of Science. Copyright 2016.

1.6 Conclusion and Implications

In summary, we have provided an overview of the remarkable abilities of cephalopods and the development of color- and shape-changing materials, devices, and systems directly inspired by these animals. We have highlighted several selected case studies related to switchable coloration, hierarchical multiplexing/pixelation, and shape/texture modulation. These studies constitute substantial progress toward advanced adaptive camouflage and shapeshifter-like technologies that emulate the abilities of cephalopods. Moving forward, we believe that the integration of cephalopod-inspired materials, devices, and systems with textiles and fabrics represents the natural

future progression of research in this field, with such work enabling the development of clothing that functions like a second skin and has a disruptive effect on daily life.

When considering the possibilities afforded by futuristic wearable adaptive camouflage, military applications readily come to mind. Indeed, the U.S. military has invested heavily in the development of advanced fabrics for concealing soldiers from detection by enemy combatants.[40-42] These efforts have often viewed universal camouflage fatigues that function with equal efficacy in any environment as the ultimate lofty goal.[40-42] The utility of such clothing becomes apparent when considering a soldier who travels from a desert to a forest environment. Initially, for optimum concealment in the desert, the soldier needs a uniform with a flat surface and large light brown or beige patterning. Subsequently, for optimum concealment in the forest, the soldier needs a uniform with a textured brush-like surface and smaller green and dark brown patterning. Fatigues that adapt to disguise the soldier in both environments therefore may greatly enhance his survivability. This type of game-changing technology could prove invaluable in many combat situations and help save countless lives.

Wearable color- and shape-changing technologies also appear highly attractive for leisure applications. Indeed, apparel companies have envisioned customizable fabrics that selectively adapt to the needs of the wearer.[43,44] As an example, Figure 1.19 shows images from an advertisement produced by Under Armour, which is entitled "Future Girl."[43] In this advertisement, a woman dons an advanced garment that dynamically regulates its properties, readily changing shape and size to conform to the user's body (Figure 1.19A). Moreover, the garment contains an integrated control and monitoring panel (Figure 1.19B), allowing the user to modulate the garment's style and coloration at the push of a button for any conceivable activity (Figure 1.19C). Such futuristic clothing presents seemingly endless possibilities, including regulation of an

individual's personal thermal comfort and direct continuous monitoring of vital signs. This type of technology could ultimately have a transformative impact on the daily activities of the average person.

The illustrative examples above are just two of a myriad of possibilities, and one can envision many other applications, including (but certainly not limited to) physical therapy for injuries, assistance for the elderly, and support suits for construction crews. However, for wearable cephalopod-inspired adaptive systems to reach their full potential, many scientific and technological challenges must still be overcome by interdisciplinary groups of scientists. For instance, despite the exciting progress made to date, further work and research is certainly necessary within the realms of switchable coloration and hierarchical multiplexing/pixelation. In addition, cephalopod-inspired materials that simultaneously change shape and color are not yet comparable to the state-of-the-art in thematically related fields, such as shape memory polymers and alloys,[45-47] as relatively fewer cephalopod-inspired studies have leveraged concepts from these entrenched areas.[48,49] Moreover, switching speed, power consumption, long-term durability, textile integration, manufacturability, and cost are all significant concerns, which we have not adequately addressed in our discussion. Finally, the envisioned applications inherently necessitate the development of advanced portable control systems for the transduction of sensory inputs from the surroundings into physical effects; such control systems require a degree of complexity comparable to that of the cephalopods' central nervous system, which is a daunting prospect. Although the numerous remaining challenges are formidable, we hope that the prospect of bringing to life concepts from fables and science fiction, i.e., adaptive camouflage and shapeshifting, will provide an impetus for additional research effort and ensure continued impressive scientific breakthroughs in the described emerging area.

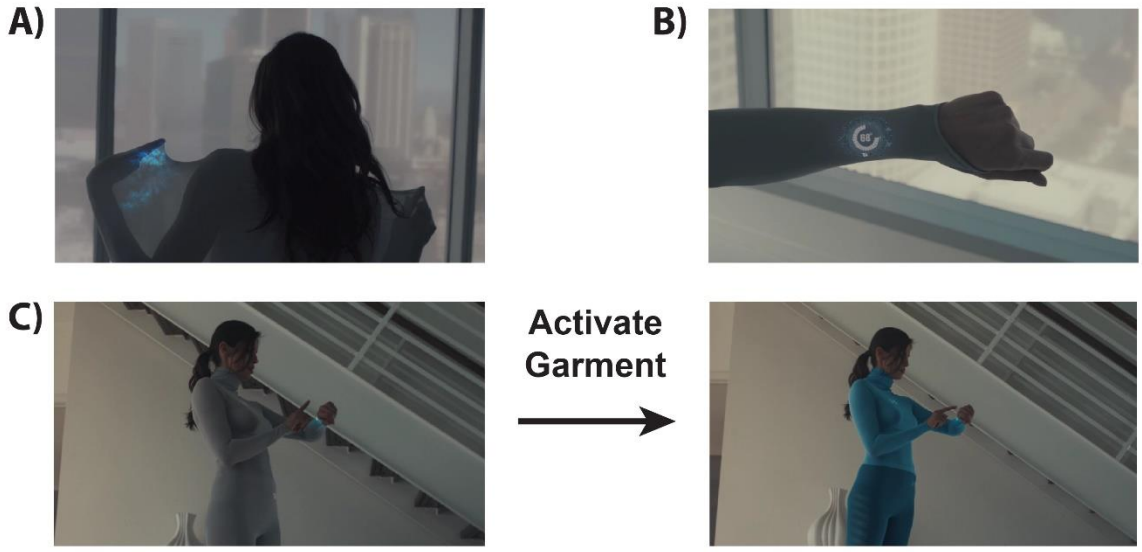

Figure 1.19: A) Picture of Under Armour's "Future Girl," who is in the process of donning a garment that adapts its size and shape to conform to the body of the wearer. B) Picture of the adaptive garment's wrist-mounted control and monitoring panel. C) Pictures of the garment when it is gray (left) and blue (right). The color change is activated via the wrist-mounted panel. Parts A–C were reproduced with permission from Under Armour.

1.7: References

1. Naso, P. O. Metamorphoses; Harvard University Press: Cambridge, England, 1916; translated by F. J. Miller.
2. von Kaysersberg, J. G. Die Emeis: Dis ist das buch von der Omeissen, und auch Herr der könnig ich diente gern; Johann Grüninger: Strasbourg, Germany, 1517.
3. Mallory, M. X-Men: The Characters and Their Universe, 1st ed.; Hugh Lauter Levin Associates: Fairfield, CT, 2006.
4. X-Men: Days of Future Past; 20th Century Fox: Los Angeles, CA, 2014, Film.
5. Mäthger, L. M.; Denton, E. J.; Marshall, N. J.; Hanlon, R. T. Mechanisms and Behavioural Functions of Structural Coloration in Cephalopods, *J. R. Soc., Interface* **2009**, *6*, S149–S163, DOI: 10.1098/rsif.2008.0366.focus
6. Hanlon, R. T.; Messenger, J. B. Cephalopod Behavior; Cambridge University Press: Cambridge, England, 1998.

7. Hanlon, R. T.; Chiao, C.-C. C.; Mäthger, L. M.; Buresch, K. C.; Barbosa, A.; Allen, J. J.; Siemann, L.; Chubb, C. Rapid adaptive camouflage in cephalopods. In Animal Camouflage: Mechanisms and Function; Stevens, M.; Merilaita, S., Eds.; Cambridge University Press: Cambridge, England, 2011; pp 145–163.
8. Kaufmann, G. director, producer, writer; Orlt, C. producer. Cuttlefish: The Brainy Bunch [Television Broadcast]. Kings of Camouflage, July 13, 2011; Public Broadcasting Service (PBS).
9. Kreit, E.; Mäthger, L. M.; Hanlon, R. T.; Dennis, P. B.; Naik, R. R.; Forsythe, E.; Heikenfeld, J. Biological Versus Electronic Adaptive Coloration: How Can One Inform the Other? *J. R. Soc., Interface* **2013**, *10*, 20120601, DOI: 10.1098/rsif.2012.0601.
10. Hanlon, R. T. Cephalopod Dynamic Camouflage, *Curr. Biol.* **2007**, *17*, R400–R404, DOI: 10.1016/j.cub.2007.03.034.
11. Steenfeldt, H. Amazing Squid Changing Color [Video File]. YouTube, August 13, 2012. https://www.youtube.com/watch?v=OauXCp8l3QI (accessed March 21, 2016).
12. DeMartini, D. G.; Ghoshal, A.; Pandolfi, E.; Weaver, A. T.; Baum, M.; Morse, D. E. Dynamic Biophotonics: Female Squid Exhibit Sexually Dimorphic Tunable Leucophores and Iridocytes, *J. Exp. Biol.* **2013**, *216*, 3733– 3741, DOI: 10.1242/jeb.090415.
13. Mäthger, L. M.; Senft, S. L.; Gao, M.; Karaveli, S.; Bell, G. R. R.; Zia, R.; Kuzirian, A. M.; Dennis, P. B.; Crookes-Goodson, W. J.; Naik, R. R.; Kattawar, G. W.; Hanlon, R. T. Bright White Scattering from Protein Spheres in Color Changing, Flexible Cuttlefish Skin, *Adv. Funct. Mater.* **2013**, *23*, 3980–3989, DOI: 10.1002/adfm.201203705.

14. DeMartini, D. G.; Krogstad, D. V.; Morse, D. E. Membrane Invaginations Facilitate Reversible Water Flux Driving Tunable Iridescence in a Dynamic Biophotonic System, *Proc. Natl. Acad. Sci. U. S. A.* **2013**, *110*, 2552–2556, DOI: 10.1073/pnas.1217260110.
15. DeMartini, D. G.; Izumi, M.; Weaver, A. T.; Pandolfi, E.; Morse, D. E. Structures, Organization, and Function of Reflectin Proteins in Dynamically Tunable Reflective Cells, *J. Biol. Chem.* **2015**, *290*, 15238–15249, DOI: 10.1074/jbc.M115.638254.
16. Messenger, J. B. Cephalopod Chromatophores: Neurobiology and Natural History, *Biol. Rev.* **2001**, *76*, 473–528, DOI: 10.1017/S1464793101005772.
17. Deravi, L. F.; Magyar, A. P.; Sheehy, S. P.; Bell, G. R. R.; Mäthger, L. M.; Senft, S. L.; Wardill, T. J.; Lane, W. S.; Kuzirian, A. M.; Hanlon, R. T.; Hu, E. L.; Parker, K. K. The Structure-Function Relationships of a Natural Nanoscale Photonic Device in Cuttlefish Chromatophores, *J. R. Soc., Interface* **2014**, *11*, 20130942, DOI: 10.1098/rsif.2013.0942.
18. Mäthger, L. M.; Hanlon, R. T. Malleable Skin Coloration in Cephalopods: Selective Reflectance, Transmission and Absorbance of Light by Chromatophores and Iridophores, *Cell Tissue Res.* **2007**, *329*, 179–186, DOI: 10.1007/s00441-007-0384-8.
19. Cloney, R. A.; Brocco, S. L. Chromatophore Organs, Reflector Cells, Iridocytes and Leucophores in Cephalopods, *Am. Zool.* **1983**, *23*, 581–592, DOI: 10.1093/icb/23.3.581.
20. Wardill, T. J.; Gonzalez-Bellido, P. T.; Crook, R. J.; Hanlon, R. T. Neural Control of Tuneable Skin Iridescence in Squid, *Proc. R. Soc. London, Ser. B* **2012**, *279*, 4243–4252, DOI: 10.1098/rspb.2012.1374.
21. Allen, J. J.; Bell, G. R. R.; Kuzirian, A. M.; Hanlon, R. T. Cuttlefish Skin Papilla Morphology Suggests a Muscular Hydrostatic Function for Rapid Changeability, *J. Morphol.* **2013**, *274*, 645–656, DOI: 10.1002/jmor.20121.

22. Allen, J. J.; Bell, G. R. R.; Kuzirian, A. M.; Velankar, S. S.; Hanlon, R. T. Comparative Morphology of Changeable Skin Papillae in Octopus and Cuttlefish, *J. Morphol.* **2014**, *275*, 371–390, DOI: 10.1002/jmor.20221.
23. Allen, J. J.; Mäthger, L. M.; Barbosa, A.; Hanlon, R. T. Cuttlefish Use Visual Cues to Control Three-Dimensional Skin Papillae for Camouflage, *J. Comp. Physiol., A* **2009**, *195*, 547–555, DOI: 10.1007/s00359-009-0430-y.
24. Mazzolai, B.; Margheri, L.; Dario, P.; Laschi, C. Measurements of Octopus Arm Elongation: Evidence of Differences by Body Size and Gender, *J. Exp. Mar. Biol. Ecol.* **2013**, *447*, 160–64, DOI: 10.1016/j.jembe.2013.02.025.
25. Vukusic, P.; Sambles, J. R.Photonic Structures in Biology Nature 2003, 424, 852–855, DOI: 10.1038/nature01941.
26. Kinoshita, S.; Yoshioka, S. Structural Colors in Biological Systems: Principles and Applications; Osaka University Press: Osaka, 2005.
27. Kinoshita, S. Structural Colors in the Realm of Nature; World Scientific Publishing Co.: Singapore, 2008.
28. Saito, A. Material Design and Structural Color Inspired by Biomimetic Approach, *Sci. Technol. Adv. Mater.* **2011**, *12*, 064709, DOI: 10.1088/1468-6996/12/6/064709.
29. Wu, L.; He, J.; Shang, W.; Deng, T.; Gu, J.; Su, H.; Liu, Q.; Zhang, W.; Zhang, D. Optical Functional Materials Inspired by Biology, *Adv. Opt. Mater.* **2016**, *4*, 195–224, DOI: 10.1002/adom.201500428.
30. Fu, Y.; Tippets, C. A.; Donev, E. U.; Lopez, R. Structural Colors: from Natural to Artificial Systems. WIREs Nanomed. Nanobiotechnol. [Online early access], 8, 758, DOI: 10.1002/wnan.1396 . Published Online: Mar 8, 2016.

31. Kramer, R. M.; Crookes-Goodson, W. J.; Naik, R. R. The Self-Organizing Properties of Squid Reflectin Protein, *Nat. Mater.* **2007**, *6*, 533–538, DOI: 10.1038/nmat1930.

32. Phan, L.; Walkup, W. G., IV; Ordinario, D. D.; Karshalev, E.; Jocson, J.-M.; Burke, A. M.; Gorodetsky, A. A. Reconfigurable Infrared Camouflage Coatings from a Cephalopod Protein, *Adv. Mater.* **2013**, *25*, 5621–5625, DOI: 10.1002/adma.201301472.

33. Phan, L.; Ordinario, D. D.; Karshalev, E.; Walkup, W. G., IV; Shenk, M. A.; Gorodetsky, A. A. Infrared Invisibility Stickers Inspired by Cephalopods, *J. Mater. Chem. C* **2015**, *3*, 6493–6498, DOI: 10.1039/C5TC00125K.

34. Wang, Q.; Gossweiler, G. R.; Craig, S. L.; Zhao, X. Cephalopod-Inspired Design of Electro-Mechano-Chemically Responsive Elastomers for On-Demand Fluorescent Patterning, *Nat. Commun.* **2014**, *5*, 4899, DOI: 10.1038/ncomms5899.

35. Rossiter, J.; Yap, B.; Conn, A. Biomimetic Chromatophores for Camouflage and Soft Active Surfaces, *Bioinspiration Biomimetics* **2012**, *7*, 036009, DOI: 10.1088/1748-3182/7/3/036009.

36. Rossiter, J.; Conn, A.; Cerruto, A.; Winters, A.; Roke, C. Colour Gamuts in Polychromatic Dielectric Elastomer Artificial Chromatophores, *Proc. SPIE* **2014**, *9056*, 905620-1–905620-8, DOI: 10.1117/12.2045168.

37. Morin, S. A.; Shepherd, R. F.; Kwok, S. W.; Stokes, A. A.; Nemiroski, A.; Whitesides, G. M. Camouflage and Display for Soft Machines Science, **2012**, *337*, 828–832, DOI: 10.1126/science.1222149.

38. Larson, C.; Peele, B.; Li, S.; Robinson, S.; Totaro, M.; Beccai, L.; Mazzolai, B.; Shepherd, R. Highly Stretchable Electroluminescent Skin for Optical Signaling and Tactile Sensing, *Science* **2016**, *351*, 1071– 1074, DOI: 10.1126/science.aac5082.

39. Yu, C.; Li, Y.; Zhang, X.; Huang, X.; Malyarchuk, V.; Wang, S.; Shi, Y.; Gao, L.; Su, Y.; Zhang, Y.; Xu, H.; Hanlon, R. T.; Huang, Y.; Rogers, J. A. Adaptive Optoelectronic Camouflage Systems with Designs Inspired by Cephalopod Skins, *Proc. Natl. Acad. Sci. USA* **2014**, *111*, 12998–13003, DOI: 10.1073/pnas.1410494111.
40. Hartcup, G. Camouflage: A History of Concealment and Deception in War; Scribner's: New York, 1980.
41. Cox, M. Congress Pushes Ahead with Plan for Joint Camouflage Uniform, 2014. Military.com. http://www.military.com/daily-news/2014/12/04/congress-pushes-ahead-with-plan-for-joint-camouflage-uniform.html (accessed February 29, 2016).
42. Hambling, D. US Army Calls for Ideas on Invisible Uniforms for Soldiers, 2015. New Scientist. https://www.newscientist.com/article/mg22630202.200-us-army-calls-for-ideas-on-invisible-uniforms-for-soldiers/#.VUsfWNOqpBd (accessed March 26, 2016).
43. Kinghorn, M. Under Armour, "Future Girl" [Video File]. Vimeo, June 25, 2013. https://vimeo.com/69062155 (accessed February 20, 2016).
44. Pierce, D. How Under Armour Plans to Turn Your Clothes Into Gadgets, 2016. Wired. http://www.wired.com/2016/01/under-armour-healthbox/ (accessed April 2, 2016).
45. Sun, L.; Huang, W. M.; Ding, Z.; Zhao, Y.; Wang, C. C.; Purnawali, H.; Tang, C. Stimulus-Responsive Shape Memory Materials: A Review, *Mater. Eng.* **2012**, *33*, 577–640, DOI: 10.1016/j.matdes.2011.04.065.
46. Jani, J. M.; Leary, M.; Subic, A.; Gibson, M. A. A Review of Shape Memory Alloy Research, Applications and Opportunities, *Mater. Eng.* **2014**, *56*, 1078–1113, DOI: 10.1016/j.matdes.2013.11.084.

47. Hager, M. D.; Bode, S.; Weber, C.; Schubert, U. S. Shape Memory Polymers: Past, Present and Future Developments, *Prog. Polym. Sci.* **2015**, *49*, 3–33, DOI: 10.1016/j.progpolymsci.2015.04.002.
48. Laschi, C.; Cianchetti, M.; Mazzolai, B.; Margheri, L.; Follador, M.; Dario, P. Soft Robot Arm Inspired by the Octopus, *Adv. Robot.* **2012**, *26*, 709– 727, DOI: 10.1163/156855312X626343.
49. Chatterjee, S.; Velankar, S. S. Reversibly Texturing Active Surfaces with Spatial and Temporal Control, *J. Intell. Mater. Syst. Struct.* **2015**, *26*, 328–339, DOI: 10.1177/1045389X14525492.

CHAPTER 2 Reconfigurable Infrared Camouflage Coatings from a Cephalopod Protein

2.1: Abstract

In nature, cephalopods employ unique dynamic camouflage mechanisms. Herein, we draw inspiration from self-assembled structures found in cephalopods to fabricate tunable biomimetic camouflage coatings. The reflectance of these coatings is dynamically modulated between the visible and infrared regions of the electromagnetic spectrum in situ. Our studies represent a crucial step towards reconfigurable and disposable infrared camouflage for stealth applications.

2.2: Introduction

Over millions of years of evolution, nature has mastered the manipulation of light and color through the controlled arrangement of nanoscale structures.[1-3] Structural color is widespread in the animal kingdom (noteworthy examples are present in insects, reptiles, cephalopods, frogs, fish, and birds), and it typically plays a crucial biological role in camouflage, communication, and temperature control.[1-3] The functional diversity of structural color has inspired the development of materials and surfaces that imitate natural coloration mechanisms.[4-6] Such studies have shown promise for applications in commercial and military technologies, including reconfigurable camouflage, advanced adaptable optics, and energy efficient devices.[4-11]

For stealth applications,[7-9] the camouflage mechanisms of cephalopods are particularly attractive. For example, squid in the Loliginidae family possess specialized dermal cells known as iridocytes.[11-19] These cells contain alternating layers of cell membrane-enclosed platelets composed of a structural protein called reflectin, which has a high refractive index, and extracellular space, which has a low refractive index.[11-19] The lamellar structures function as

modular Bragg reflectors, whose spacing Loliginids tune to modulate their skin coloration across the entire visible spectrum and even into the near infrared.[11-19] Thus, the Loliginidae family demonstrates two capabilities that are highly desirable in next generation infrared stealth technology:[7-9] the reflectance of light over a broad range of wavelengths (extending from the visible region into the near infrared region) and reversible dynamic color tunability.

Herein, we describe our progress towards Loliginid-inspired biomimetic infrared camouflage. Our strategy uses simple fabrication techniques to prepare thin films from a water-soluble *Loligo* (*Doryteuthis*) *pealeii* reflectin isoform[15] on graphene oxide-coated substrates. We can dynamically tune the reflectance of our coatings over more than 600 nm, which, to the best of our knowledge, represents the largest tunable reflectance window for any biological thin film. This tunability allows our films to reversibly disappear and reappear when visualized with an infrared imaging camera. Our findings represent an inexpensive and robust strategy for the fabrication of dynamically tunable infrared camouflage coatings on arbitrary surfaces.

2.3 Results and Discussion

We began our studies by optimizing heterologous expression and inclusion body preparation protocols for the production of the histidine-tagged reflectin A1 (RfA1) isoform in *E. coli*. The protein was sequentially purified by immobilized metal affinity chromatography (IMAC) under denaturing conditions and high performance liquid chromatography (HPLC) (Figure S2.1 and Figure S2.2, Supporting Information). The identity of the purified RfA1 was definitively confirmed by in-gel tryptic digestion and tandem mass spectrometry, which produced sequence coverage in excess of 96% (Figure S2.3). Notably, our optimized expression and purification procedure yielded >800 mg of purified RfA1 per liter of *E. coli* cell culture, with a purity of over

99%, as judged from HPLC chromatograms (Figure S2.1). The high yield and excellent purity facilitated subsequent thin film fabrication.

We proceeded to screen a variety of substrates and surface treatments for the reliable formation of RfA1 thin films. The best results were obtained by spincasting 5 to 10 nm films of graphene oxide on (3-aminopropyl)triethoxy silane (APTES)-modified fused silica (or glass) substrates (Figure 2.1A). This material, which presents a negatively charged, amphipathic surface, is well suited for the electrostatically-induced assembly of positively charged RfA1.[20,21] We used a modified doctor blading approach to spread RfA1 onto the graphene oxide-coated substrates (Figure 2.1A), yielding smooth films over centimeter areas, as determined by optical microscopy and atomic force microscopy (AFM) (Figure 2.1B and Figure S2.4).

We next investigated the optical properties of our RfA1 films. Here, the distinct coloration of the surfaces was dictated by the film thickness. As examples, Figure 2.1B and Figure 2.1C show typical optical images and reflectance spectra for two RfA1 films on silica: a 125 nm-thick blue film and a 207 nm-thick orange film, as determined by profilometry and interferometry. The observed peak reflectance wavelengths ($\lambda = 431$ nm and $\lambda = 625$ nm for the blue and orange films, respectively) yielded theoretical thicknesses (138 nm and 204 nm for the blue and orange films, respectively) that were in excellent agreement with the measured values (see Supporting Information for calculation details).[22]

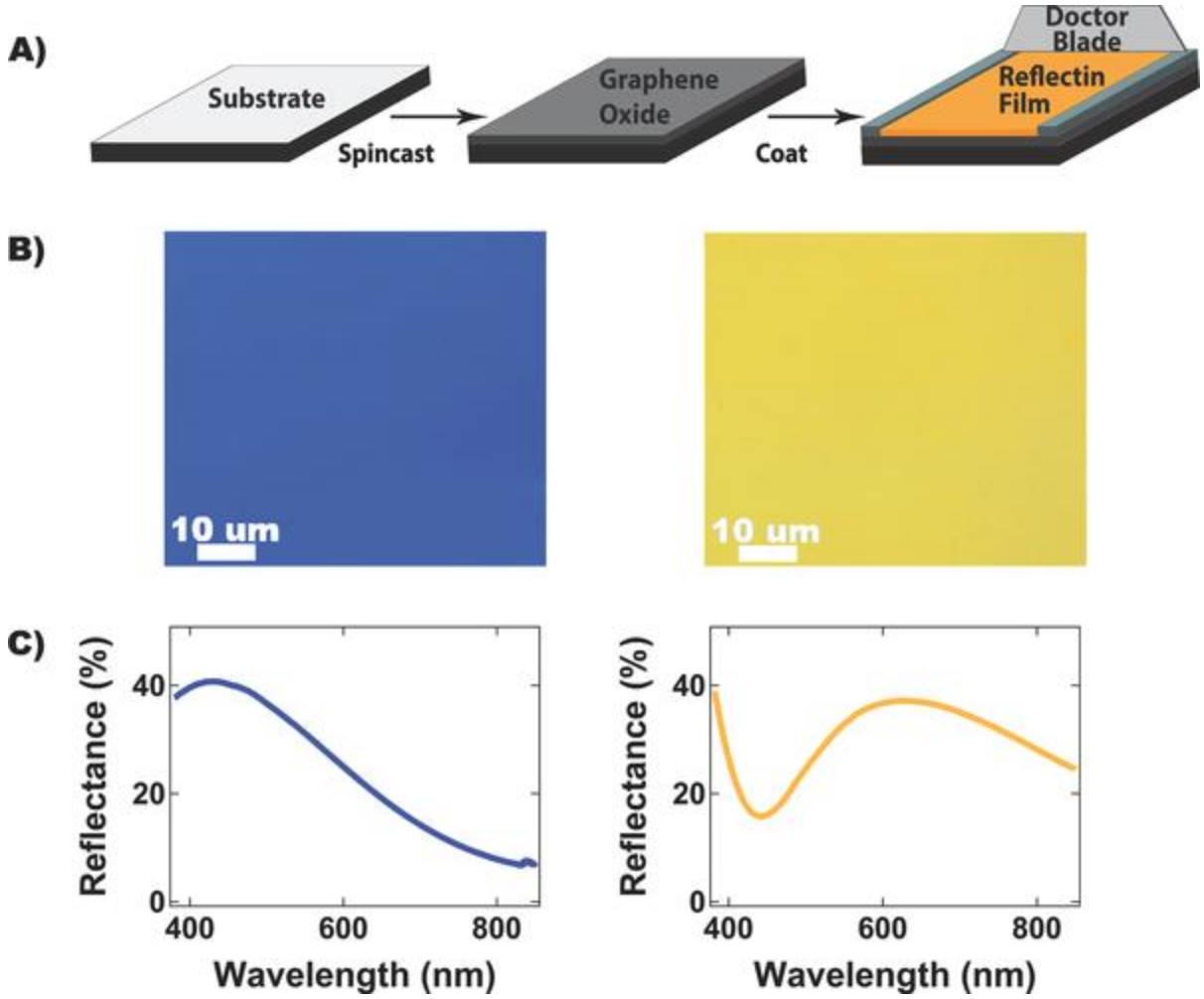

Figure 2.1: A) Illustration of the fabrication of RfA1-coated substrates. The process consists of casting a graphene oxide film onto an APTES-modified substrate, followed by doctor blading of RfA1 directly onto this surface. B) Typical optical microscopy images for blue (left) and orange (right) RfA1 thin films, with thicknesses of 125 nm and 207 nm, respectively. C) Correponding reflectance spectra for the blue (left) and orange (right) films.

Inspired by the dynamic optical properties of reflectin nanostructures, we sought to shift the reflectance of our RfA1 films into the infrared region of the electromagnetic spectrum. Given that Loliginids can dynamically modulate their skin reflectance across the entire visible spectrum and even out to near infrared wavelengths of ≈800 nm,[19] we postulated that it should also be possible to tune the reflectance of our RfA1 thin films across a similar, or even larger, wavelength range. Thus, we sought conditions that would significantly increase the thickness of our RfA1 films and, consequently, shift their reflectance spectra toward the infrared.

We first explored the response of our coatings to an increase in relative humidity. Previous work demonstrated that reflectin thin films exhibit hydrogel-like behavior and can be swollen by exposure to water vapor, modulating the peak reflectance across the visible spectrum.[14,17] Indeed, for a typical orange film, the presence of water vapor (relative humidity of 75%) caused the thickness to increase from 207 nm to 244 nm, with a concomitant peak reflectance shift from λ = 625 nm to λ = 765 nm, as determined by interferometry (Figure S2.5). These observations were in qualitative agreement with previous studies.[17]

To modulate the reflectance of our RfA1 coatings over an even larger wavelength range, we explored their response to a variety of chemical stimuli (see Supporting Information). We discovered that exposing our films to vapor from a concentrated acetic acid solution induced a large, reversible shift in the reflectance spectra (Figure 2.2A and Figure S2.6). For example, when exposed to acetic acid vapor, an orange film on glass exhibited a new peak centered at λ = 1200 nm (Figure 2.2A), which correlated to a film thickness of 394 nm (see Supporting Information for calculation details). Bovine serum albumin (BSA) control films prepared and treated under identical conditions displayed a much smaller response to acetic acid vapor (Figure S2.7). Surprisingly, the RfA1 films were stable upon exposure to acetic acid and could be dynamically cycled between visible and near infrared reflectance more than 140 times prior to degradation (Figure S2.4 and Figure S2.6). The large wavelength range and exceptional stability of our material represent important advantages for infrared camouflage coating applications.[7-9]

To explain the observed acid-induced swelling behavior, we considered the structure of the RfA1 films, which is illustrated in Figure 2.2B. The films are known to consist of closely packed RfA1 nanoparticles, as demonstrated by TEM and SAXS studies.[15] Thus, we investigated the formation and size of RfA1 nanoparticles in solution as a function of pH via circular dichroism

(CD), fluorescence spectroscopy, and dynamic light scattering (DLS). In deionized water at a pH of ≈6.3, DLS revealed the formation of a stable solution of aggregated RfA1 with a narrowly distributed hydrodynamic radius of RH = 75 nm (±11 nm) (Figure S2.8). Furthermore, CD indicated that the aggregated RfA1 possessed little secondary structure (Figure S2.9) and fluorescence spectroscopy revealed a peak at λ = 342 nm, which is characteristic of tryptophan residues (Figure S2.10).[23] Decreasing the pH to ≈2.3 caused little change in the protein structure, as evidenced by the CD spectra (Figure S2.9) and fluorescence measurements (Figure S2.10). However, DLS revealed that the average size of the aggregates increased to RH = 99 nm (±15 nm) at low pH, with a narrow distribution and no evidence of nanoparticle break-up (Figure S2.8). In their totality, these observations indicated that RfA1 nanoparticles occupy a larger volume under more acidic conditions, though the protein itself undergoes minimal structural changes.

Given previous literature precedent[15] and our own observations, we postulate a simple model for acid-induced swelling of our films (Figure 2.2B). The isoelectric point (pI) of RfA1 is 9.1, so at neutral pH, RfA1 possesses a net positive charge.[15] Acidic conditions further increase the positive charge of the RfA1 protein, likely through the protonation and neutralization of the side chains of aspartic and glutamic acid residues (pKa of ≈3.9 and ≈4.3, respectively) and through the protonation of the imidazole groups of histidine residues (pKa of ≈6.0 to ≈7.0).[23] This increase in net positive charge leads to enhanced intra-protein electrostatic repulsion and accounts for the observed swelling of the RfA1 nanoparticles in solution. Since our films consist of closely packed RfA1 nanoparticles,[15] the swelling of the individual nanoparticles explains the significant increase in film thickness under acidic conditions.

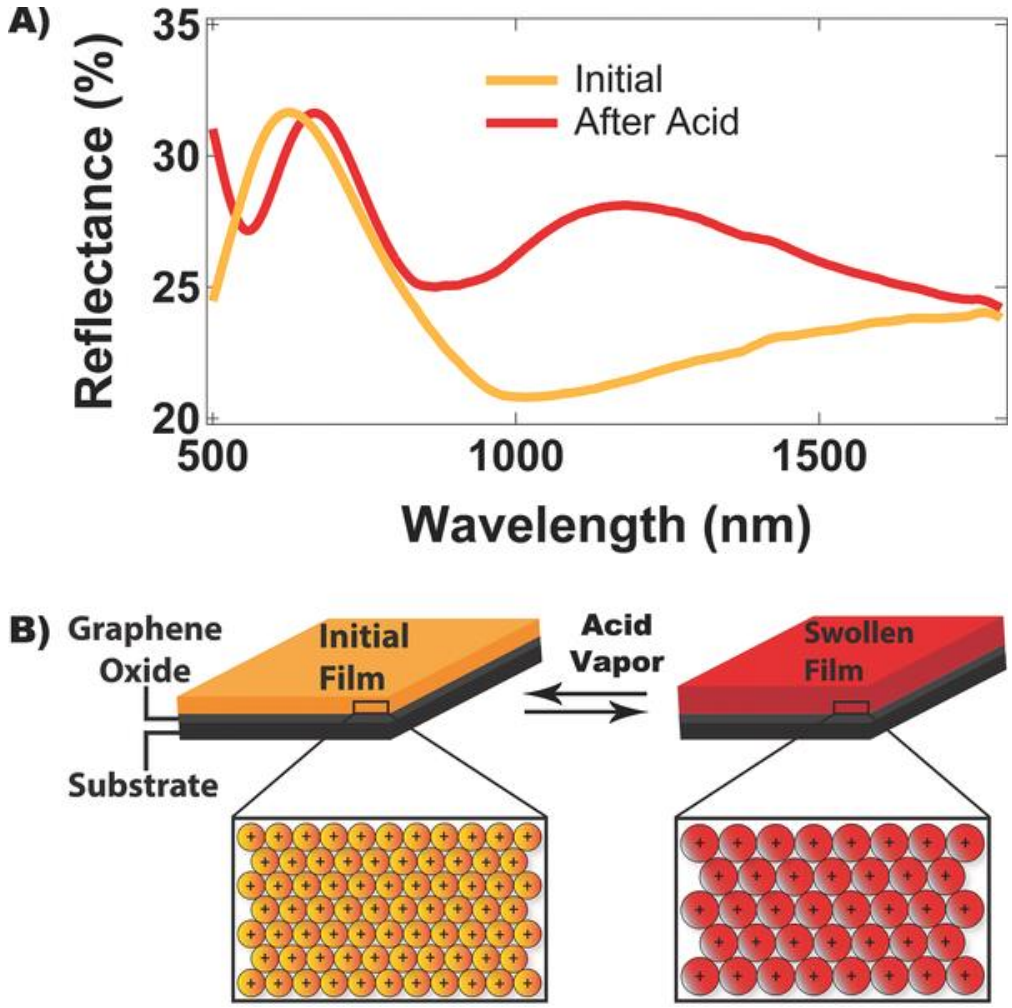

Figure 2.2: A) Effect of acetic acid vapor on the reflectance spectrum of an RfA1 film. Swelling of the film leads to the appearance of a large reflectance peak centered at 1200 nm. The curves have been smoothed for clarity. B) Illustration of acetic acid vapor-induced swelling for a film composed of net positively charged RfA1 nanoparticles.

In a proof of principle demonstration of our coatings' infrared camouflage capabilities, we visualized RfA1-covered silica substrates with a camera in both standard and infrared imaging modes, while modulating their reflectance in situ (Figure 2.3A). Under white light illumination, a typical RfA1 film appeared orange and could be readily distinguished from a piece of black paper and a leaf (Figure 2.3B). Under infrared illumination at $\lambda = 940$ nm without any chemical stimulus, the RfA1 coating appeared black, with a relative brightness of 13% and resembled the paper control sample, with a relative brightness of 1% (Figure 2.3B and Figure S2.11). The leaf, which reflected in the infrared as expected for typical foliage, appeared red, with a relative brightness of

57% (Figure 2.3B and Figure S2.11). However, under infrared illumination at λ = 940 nm in the presence of acetic acid vapor, the reflectance of the RfA1 film shifted into the near infrared, and the RfA1-coated substrate appeared red, with a maximum relative brightness of 100% (Figure 2.3B and Figure S2.11). The RfA1-coated substrate thus became distinct from the paper control, with a relative brightness of 7%, and now resembled the leaf control, with a relative brightness of 64%. (Figure 2.3B and Figure S2.11). Overall, this experiment demonstrated that the RfA1-covered substrates could be dynamically hidden or revealed when probed with standard infrared detection equipment.

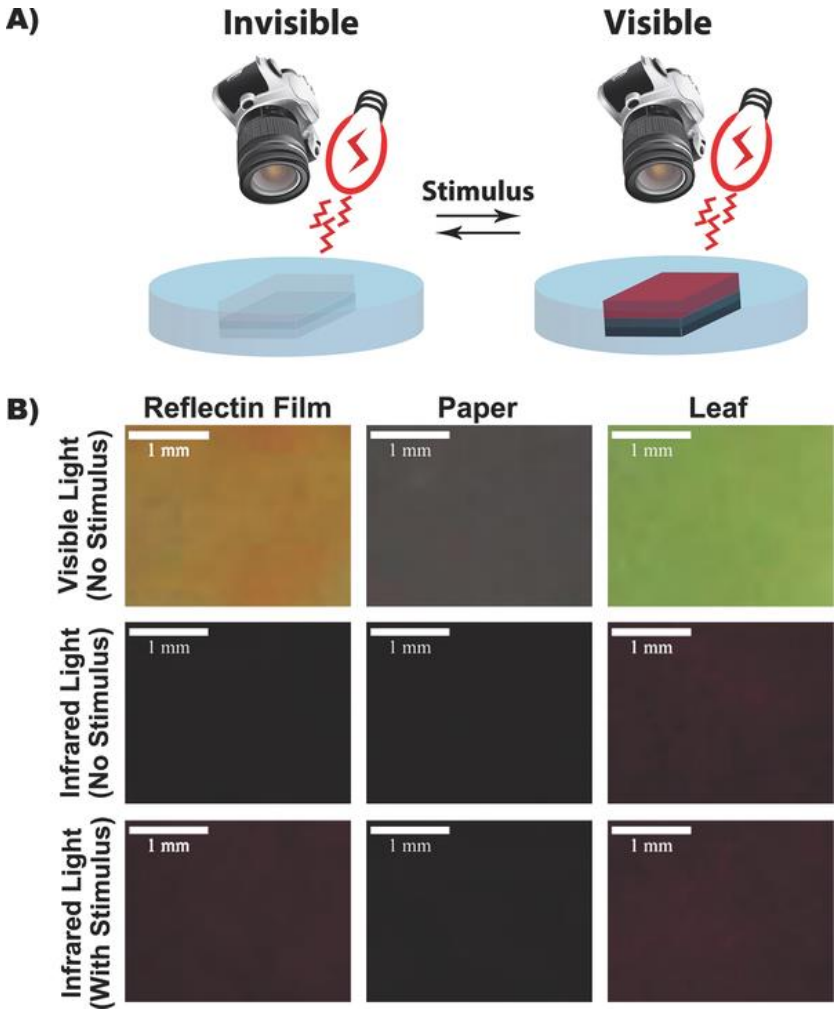

Figure 2.3: A) Illustration depicting the appearance of the RfA1 film in the absence and presence of an external stimulus (acetic acid), when visualized with an infrared camera. B) First row: images of an RfA1-coated substrate (left), a black piece of paper (center), and a plant leaf (right) that were captured with a standard camera under white

light illumination. Second row: images of the same RfA1-coated substrate (left), black piece of paper (center), and plant leaf (right) that were captured with an infrared camera in the absence of acetic acid under infrared diode illumination. Third row: images of the same RfA1-coated substrate (left), black piece of paper (center), and plant leaf (right) that were captured with an infrared camera in the presence of acetic acid under infrared diode illumination. Note the change in apparent coloration from black to red for the RfA1-coated substrate in the absence (second row, left) and presence (third row, left) of acetic acid vapor.

2.4 Conclusion

In conclusion, we have demonstrated graphene-templated, biomimetic camouflage coatings that possess several important advantages. The thin film fabrication strategy is inexpensive, robust, and compatible with a wide range of substrates of arbitrary form factor. The reflectance spectra of our coatings are modulated in situ, with an accessible coloration range between $\lambda = 400$ nm and $\lambda = 1200$ nm, as well as a dynamic tunability of over 600 nm. To the best of our knowledge, the demostrated in situ reflectance window is the largest reported for any biological thin film. In addition, we are aware of only limited examples of conformable coatings from soft materials that display dynamic tunability of their reflectance,[24-31] with only a single example demonstrating in situ dynamic reflectance modulation over a larger portion of the electromagnetic spectrum.[24] Furthermore, the thin film reflectance of our samples extends into the important $\lambda = 700$ nm to $\lambda = 1200$ nm spectral region, which matches the standard imaging range of infrared visualization equipment.[7-9] Given these advantages, our dynamically tunable, infrared-reflective films represent a crucial first step towards the development of reconfigurable and disposable biomimetic camouflage technologies for military stealth applications.[7-9]

2.5 Supplementary Information

Reflectin A1 Expression and Purification: An *E. coli* codon optimized gene coding for 6X histidine-tagged reflectin A1 protein (RfA1) from *Doryteuthis pealeii* (Genbank: ACZ57764.1) was synthesized and cloned into the pJExpress414 vector (DNA2.0). Note that the histidine tag,

while required for purification, may alter the properties of the wild type protein. The vector was transformed into BL21(DE3) cells (Novagen). RfA1 was expressed at 37 °C using Overnight Express Instant Terrific Broth (TB) media (Novagen) supplemented with 100 μg mL^{-1} Carbenicillin. RfA1 was completely insoluble when expressed at 37 °C and was sequestered in inclusion bodies prepared using BugBuster (Novagen) according to the manufacturer's suggested protocols. The RfA1 inclusion bodies were then solubilized in denaturing buffer (pH 7.4, 50 mM sodium phosphate, 300 mM sodium chloride, 6 M guanidine hydrochloride) and purified under denaturing conditions on a HisPur Cobalt Resin gravity column (Thermo Scientific) according to the manufacturer's protocols (elution was performed using denaturing buffer supplemented with 250 mM imidazole). The fractions containing RfA1 protein were pooled and concentrated on an Amicon Concentrator (Millipore) before being purified with high performance liquid chromatography (HPLC) on an Agilent 1260 Infinity system using a reverse phase C18 column. The gradient was evolved from 95% Buffer A:5% Buffer B to 5% Buffer A:95% Buffer B at a flow rate of 0.5 mL min^{-1} over 20 minutes (Buffer A: 99.9% water, 0.1% trifluoroacetic acid; Buffer B: 95% acetonitrile, 4.9% water, 0.1% trifluoroacetic acid). The pure RfA1 protein was pooled, flash frozen in liquid nitrogen, and lyophilized. Protein concentrations and yields were quantified via the Bradford protein assay (BioRad) with BSA as the standard.

Reflectin A1 Analysis: Sodium dodecyl sulfate polyacrylamide gel electrophoresis (SDS-PAGE) was performed to assay protein purity and analyze RfA1 yields throughout the purification process. RfA1 samples were analyzed by SDS-PAGE and Gel Code Blue Reagent staining (Thermo Scientific) on an XCell SureLock Mini-cell Electrophoresis System (Invitrogen) using NuPAGE Novex 4–12% Bis-Tris gels (Invitrogen), with either NuPAGE MOPS or MES (Invitrogen) as the running buffer under reducing conditions (Figure S2.2). Stained protein bands were subjected to

in-gel tryptic digestion, which was performed according to literature procedures.[32] After digestion, the RfA1 peptides were separated on C18 resin beads and analyzed by mass spectrometry on a Waters Synapt G2 instrument outfitted with an electrospray ionization source.

Spectroscopic Characterization: RfA1 was analyzed with dynamic light scattering, fluorescence spectroscopy, UV-visible spectroscopy, and circular dichroism. Dynamic light scattering measurements were performed with a Malvern Zeta-Sizer Nano S instrument. Fluorescence spectra were obtained on a Hitachi F4500 Fluorescence Spectrophotometer. UV-visible spectra were obtained on a Cary 50 Spectrophotometer. Circular dichroism spectra were obtained on a Jasco J-810 Spectropolarimeter. All measurements were performed in deionized water (MilliQ). When necessary, the pH was adjusted with acetic acid and measured both in the presence and absence of RfA1.

Thin Film Fabrication: Square chips cut from either silica substrates (SQI) or glass slides (VWR) were etched in piranha solution (1:3 hydrogen peroxide to sulfuric acid) for 45 minutes. The chips were sequentially rinsed with HPLC-grade acetone and isopropanol, prior to being dried with nitrogen. The substrates were subsequently immersed in a 3% (3-Aminopropyl)triethoxysilane (APTES) in acetone solution for ≈2 (glass) or ≈10 (silica) minutes, rinsed with acetone, and dried with nitrogen. The chips were coated with graphene oxide (Graphene Marketplace) at 3000 RPM on a Laurell WS-400-NNP spincoater. For doctor blading of RfA1, the graphene oxide-coated substrates were modified with teflon tape (McMaster-Carr) on two sides, which acted as a spacing rail and allowed the blade to sit above the substrate surface. The RfA1 solution was then cast onto the substrate in front of the blade, which was translated at a constant speed across the surface to

produce thin films. To promote water evaporation and uniform film formation, the coating procedure was performed on a hot plate at 80 °C. Thicker films were produced by varying the RfA1 concentration (typically ≈500 μM for blue films) and/or applying multiple sequential coatings.

Physical Characterization of Thin Films: RfA1 thin films were characterized with atomic force microscopy and profilometry. The surface morphology was examined in situ with an Asylum Research MFP-3D AFM outfitted with an Asylum Research Humidity Sensing Cell. The AFM data was analyzed with the Gwyddion software package. The topological scans were rastered at 0.50 Hz and normalized using polynomial subtraction for improved image quality. Film thicknesses were confirmed with a Bruker Dektak XT profilometer by examining trenches scribed directly into the protein film.

Optical Characterization of Thin Films: RfA1 thin films were characterized with optical microscopy and reflectance measurements. Optical images were obtained on a Carl Zeiss Axio Imager A1M Microscope (outfitted with an Epiplan 20X lens, NA = 0.4) and processed with the manufacturer's AxioVision AC4.5 software. Reflectance spectra were measured in the presence and absence of solvent vapor on three instruments: 1) an Ocean Optics SD2000 Miniature Fiber Optic Spectrometer, outfitted with a tungsten halogen white light source and a R400–7 Reflection/Backscattering Probe (effective wavelength range of λ = 340 nm to λ = 950 nm); 2) a Perkin-Elmer Lambda 950 Spectrophotometer, outfitted with deuterium and tungsten halogen white light sources and a 60 mm integrating sphere (effective wavelength range of λ = 190 nm to λ = 3300 nm); and 3) a Filmetrics F40-NSR microscope system, outfitted with a tungsten halogen

white light source (effective wavelength range of λ = 400 nm to λ = 800 nm). For measurements in the presence of water or acetic acid vapor, the samples were housed in custom built closed cells fabricated from either a polystyrene petri dish (Fisher Scientific) or from ABS+ plastic fitted with an N-BK7 glass window (Anchor Optics) (Figure S2.12). Measurements on the Filmetrics F40-NSR microscope system allowed for confirmation of the film thickness determined by AFM and profilometry. The reflectance data were acquired normal to the substrate surface and were referenced to a SpectraLabs Spectralon Reflectance Standard (unless otherwise noted).

Infrared Imaging of Coated Substrates: The infrared imaging experiments employed a Nikon D-70 Camera equipped with a 35 mm f/1.8 AF-S DX Lens (Nikon) and a 52 mm RM-72 infrared filter (Hoya). The infrared illumination light source consisted of a home-built 26 LED array (XtraLED). The images were captured with an exposure time of 1 second, aperture setting of f/8, and ISO of 200. The integrated relative brightnesses were determined with Adobe Photoshop CS6.

Detailed Description of Film Thickness Calculations: The theoretical film thicknesses were calculated based on thin-film interference theory.[33] At normal incidence, the reflected light obeys the formula:

$$m * \lambda = 2 * n * d$$

where *m* is an integer that describes wavelength order, λ is the peak reflected wavelength, *n* is the refractive index of the film, and *d* is the film thickness. At non-normal incidence, a factor of $cos(\Theta_F)$ must be introduced, where Θ_F is the angle in the film that can be calculated with Snell's Law. The formula above is applicable for measurements performed with an integration sphere accessory because the angle of incidence for the integrating sphere is 10°, leading to a small

deviation in the theoretical thickness (<4%).[33] Furthermore, the graphene oxide adhesion layer used in our experiments was very thin with a high refractive index, so it did not dramatically influence the calculated values. The refractive indices used for the calculations were measured at Filmetrics (San Diego, CA) using a Filmetrics F20-UV spectrometer (Figure S2.13).

Surface Treatment: The APTES/graphene oxide surface treatment yielded smooth RfA1 films over large areas. Alternative surface functionalization schemes, such as triethoxyoctylsilane (OTES) treatment, UV-Ozone exposure, and APTES treatment without graphene oxide, produced less reliable results.

Response of Reflectin Films to Chemical Stimuli: We screened numerous potential solvents for shifting the reflectance of RfA1 coatings. These solvents included acetic acid, ethanol, ethyl acetate, isopropanol, triethyl amine, dimethyl formamide, and dimethyl sulfoxide. Such stimuli produced small spectral shifts, with the exception of acetic acid vapor

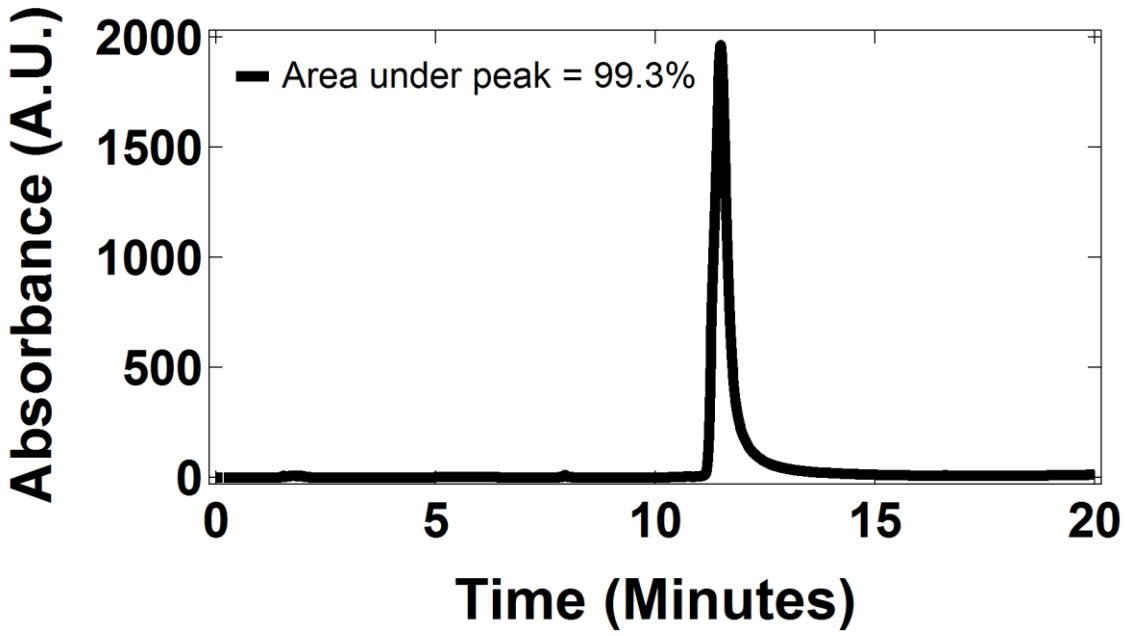

Figure S2.1: Typical reverse phase HPLC chromatogram of RfA1 following immobilized metal affinity chromatography. The presence of a single peak, whose area integrates to > 99 % of the total peak area represented in the chromatogram, indicates the excellent purity of our protein. The single peak also indicates that higher order aggregates are not present during chromatographic purification. RfA1 was eluted in a gradient evolved from 5 % Buffer A:95 % Buffer B to 95 % Buffer A:5 % Buffer B at a flow rate of 0.5 mL min^{-1} over 20 minutes (Buffer A: 99.9 % H2O, 0.1% TFA; Buffer B: 95 % acetonitile, 4.9 % H2O, 0.1% TFA).

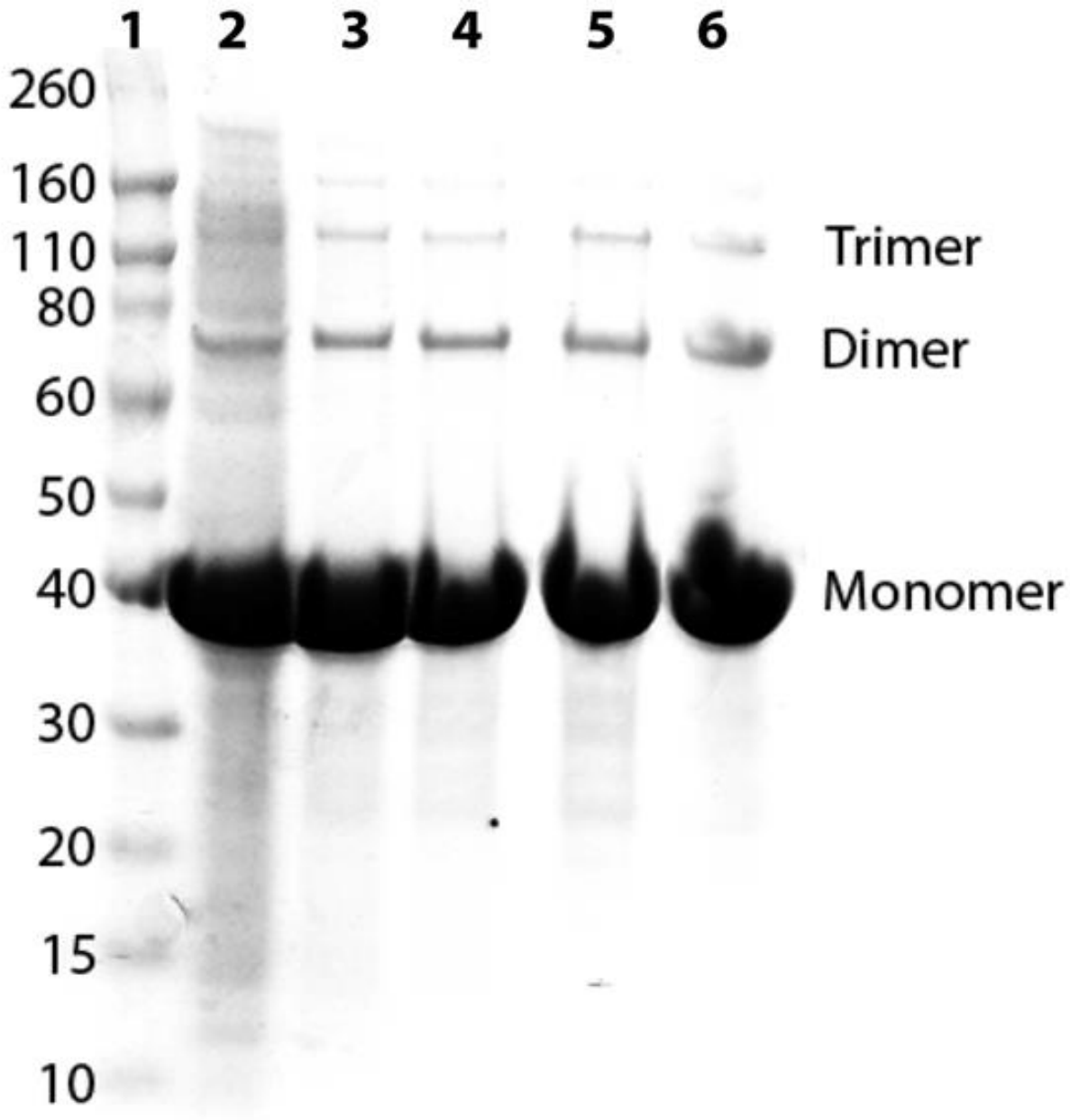

Figure S2.2: Analysis of the purification of RfA1 via denaturing gel electrophoresis. Samples of RfA1 at different stages of the purification process were analyzed by SDS-PAGE and visualized by GelCode Blue Stain Reagent (Thermo Scientific). Lane 1: Novagen Sharp protein ladder for molecular weights of 10 kDa to 260 kDa. Lane 2: Total protein fraction after cell pellet resuspension and lysis. Lane 3: Insoluble protein fraction following centrifugation. Lane 4: Inclusion body fraction after resuspension in denaturing buffer. Lane 5: Eluate from the IMAC (HisPur Cobalt Resin) gravity column. Lane 6: Eluate from C18 reverse phase HPLC column. Bands corresponding to monomeric (44,605 Da) and oligomeric RfA1 are labeled accordingly.

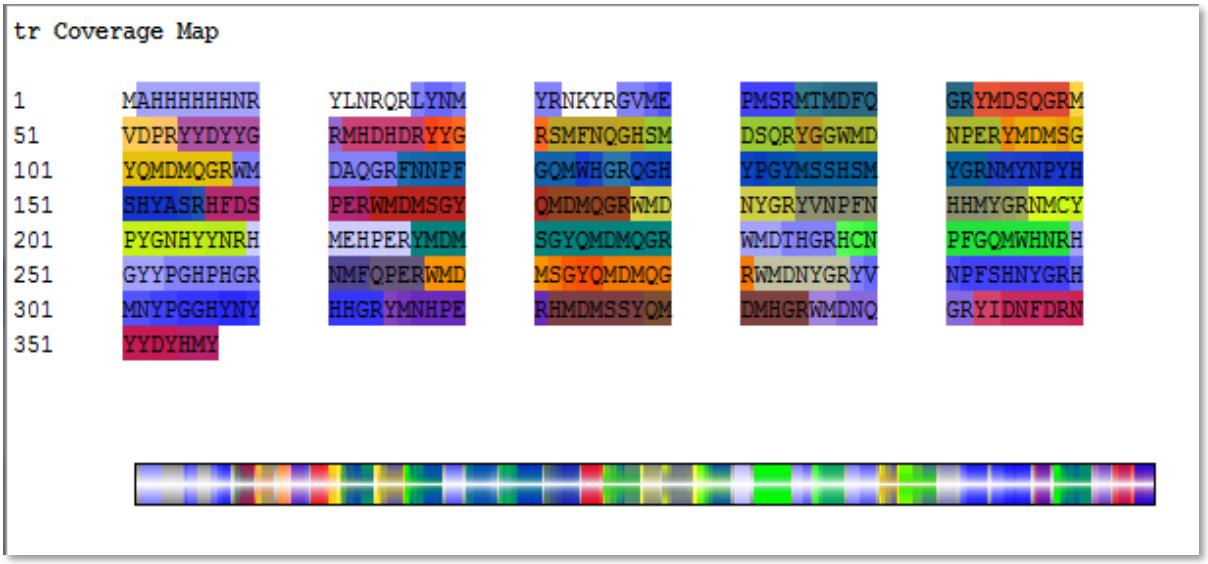

Figure S2.3: Peptide coverage map of RfA1 protein sequence produced by in-gel digestion of purified soluble RfA1 with porcine trypsin. The color coding corresponds to different tryptic peptide fragments. Sequence coverage exceeded 96%, definitively confirming the purified protein's identity as RfA1.

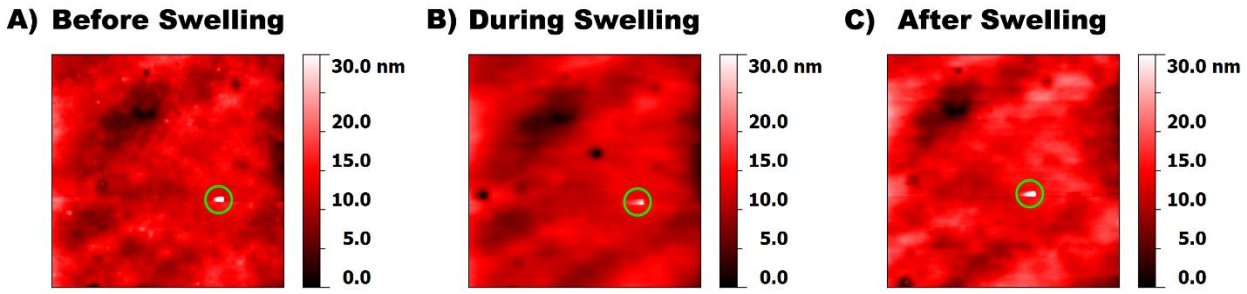

Figure S2.4: A) Atomic force microscopy (AFM) images of a RfA1 film A) before, B) during, and C) after exposure to acetic acid vapor. The film morphology does not exhibit any signs of degradation during and after the incubation. Note that the AFM images represent the same spot on each film as demonstrated by the green marker.

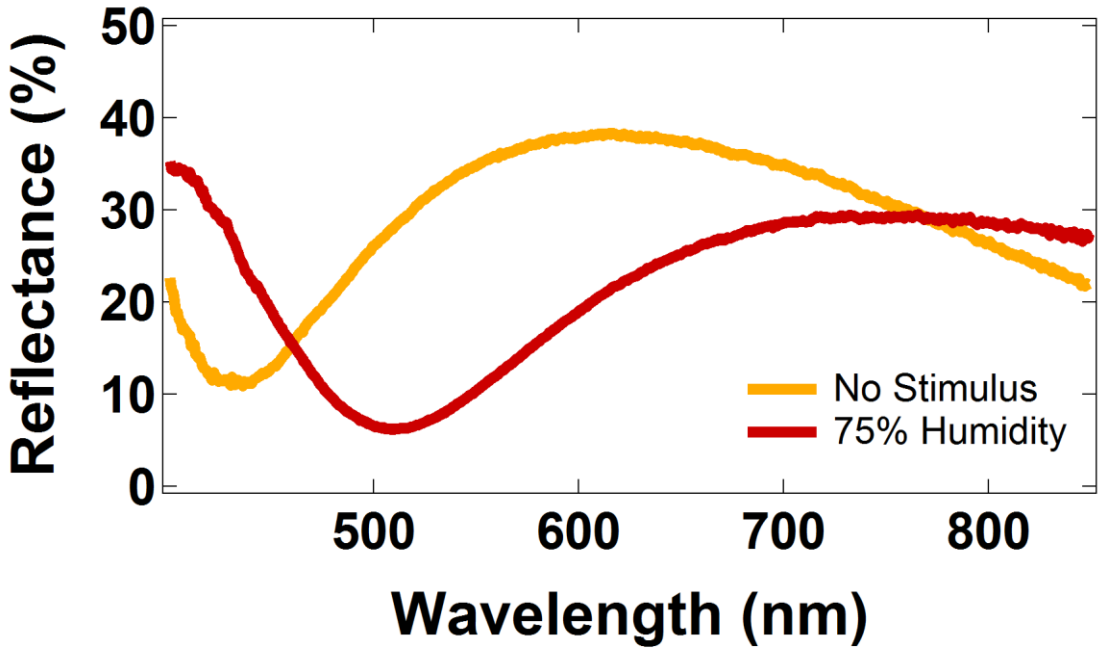

Figure S2.5: Reflectance spectra of an RfA1 orange film before (orange curve) and after (red curve) exposure to water vapor (relative humidity of 75%).

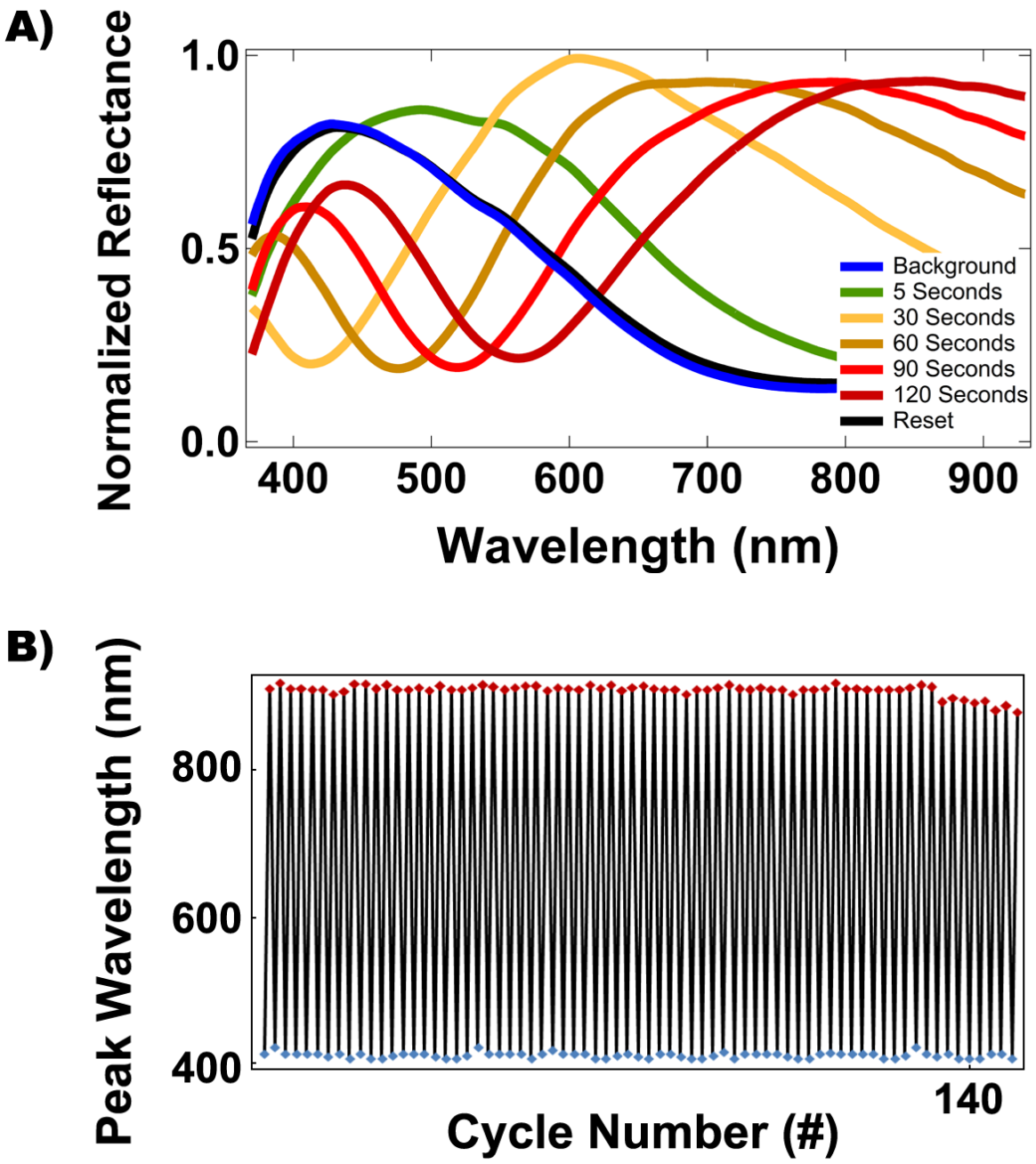

Figures S2.6: A) Change in the reflectance for an RfA1 film as a function of time following application of acetic acid vapor. The spectra were collected with a bare fused silica substrate as the standard and normalized with respect to the maximum reflectance value. Note that the initial reflectance spectra can be recovered within seconds by a "reset" or removal of the acetic acid vapor stimulus (the blue and black traces overlap). B) Illustration of reversible cycling of the RfA1 films between a peak reflectance of λ = 400 nm in the visible (blue markers) and a peak reflectance of λ = 900 nm in the infrared (red markers). The cycling was performed by exposure to solvent vapor from a glacial acetic acid solution. The experiment was repeated until the film demonstrated a degradation in the reflectance intensity.

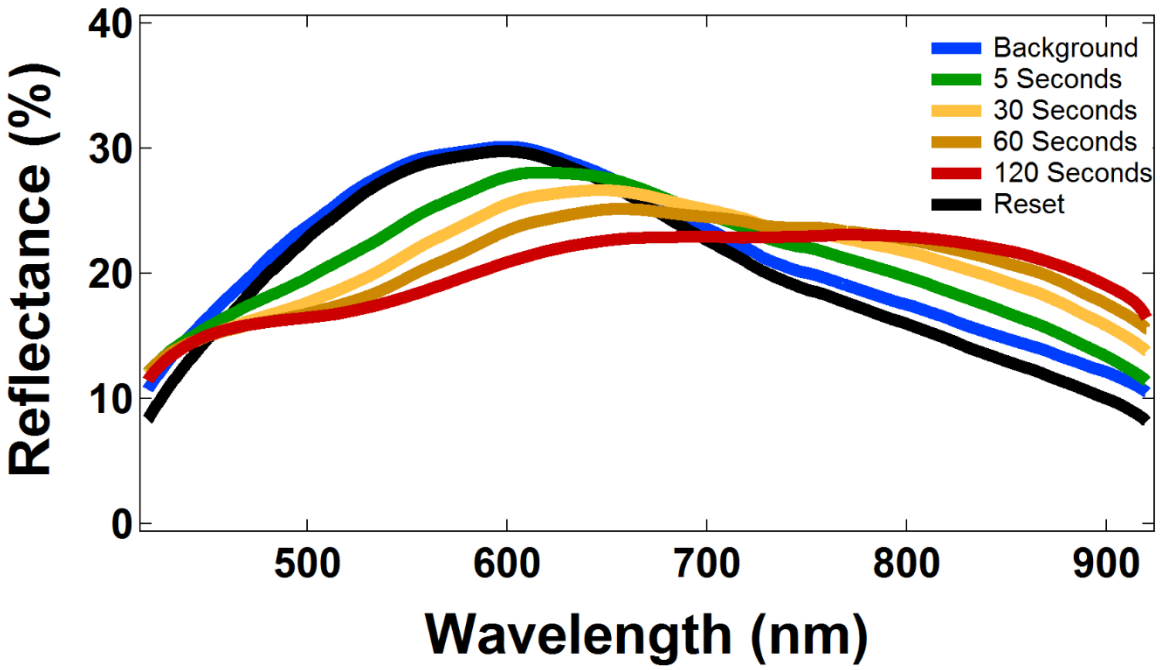

Figure S2.7: Reflectance spectra for a Bovine Serum Albumin (BSA) film as a function of time following application of acetic acid vapor. The film preparation and treatment were identical to those used for RfA1 films. The curves have been smoothed for clarity. Note the small peak shift.

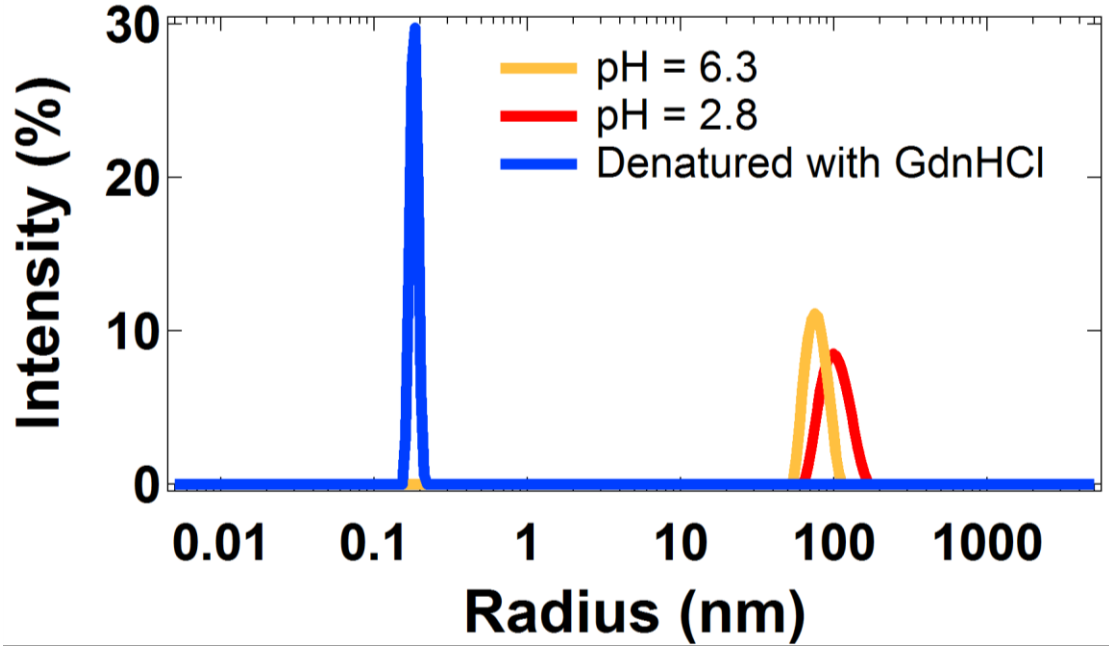

Figure S2.8: Dynamic light scattering spectra for RfA1 (0.5 mg/mL) at pH 6.3 (orange curve) and pH 2.8 (red curve). The measured RH value increases from 75 (±11) nm at pH 6.3 to 99 (±14) nm at pH 2.8. The size of the aggregated RfA1 is distinct from that reported in reference 15 in the text, presumably due to differences in the protein and salt concentrations. The aggregation of RfA1 was confirmed by the introduction of guanidinium hydrochloride (GdnHCl) into the solution, which denatured RfA1 (blue curve), yielding an RH value of < 1 nm.

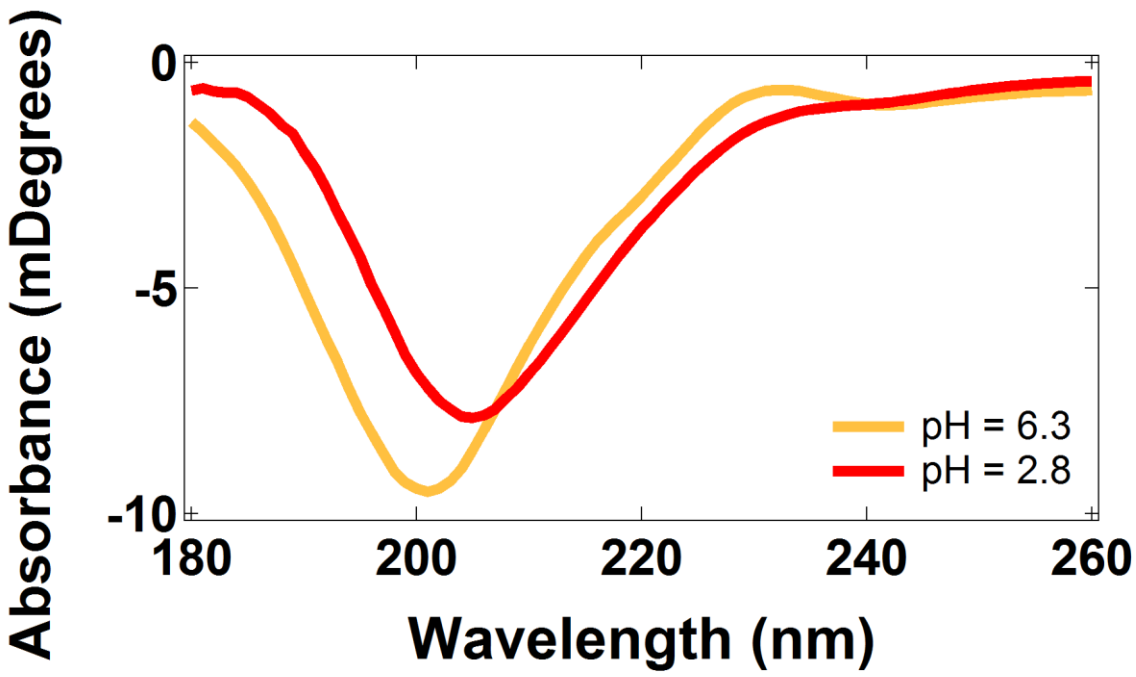

Figure S2.9: Circular dichroism spectra for RfA1 (~0.5 mg/mL) at pH 6.3 (orange curve) and pH 2.8 (red curve). The spectra were analyzed with DICHROWEB software (http://dichroweb.cryst.bbk.ac.uk), indicating that RfA1 possesses little to no alpha helical or beta strand secondary structure, which is in excellent agreement with previous findings (see references 13 to 17 in the text).

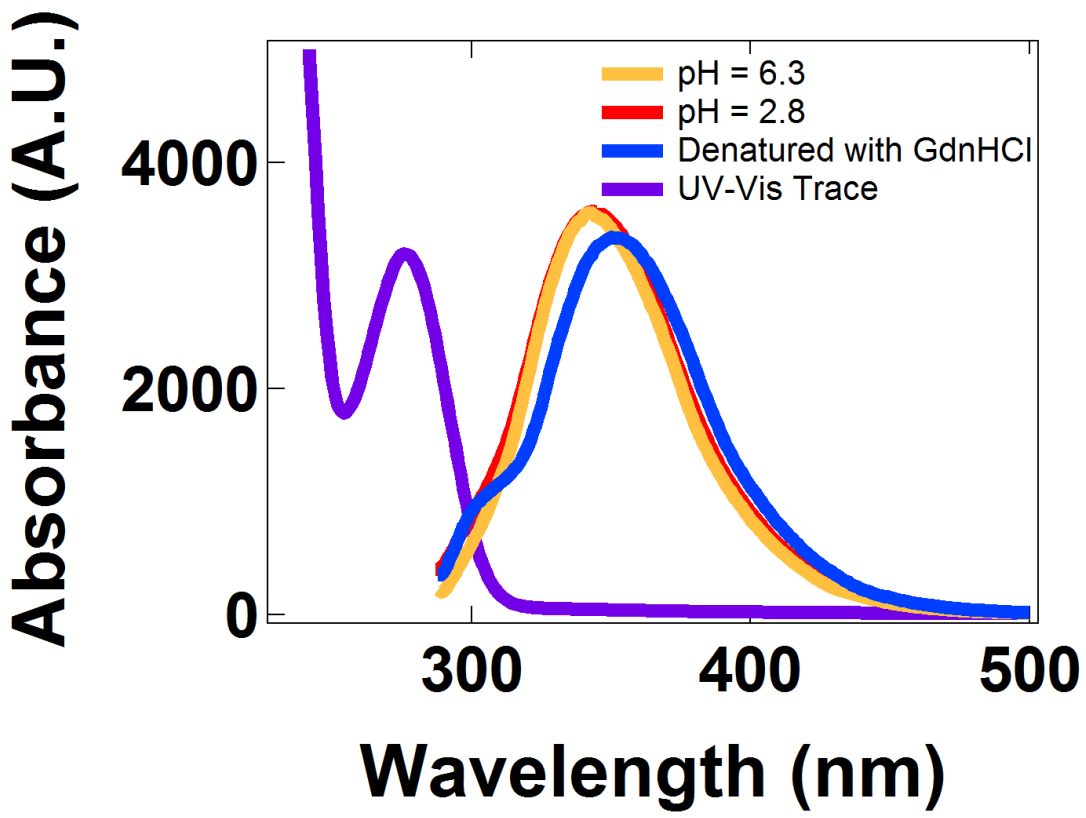

Figure S2.10: Fluorescence and UV-visible absorbance spectra for RfA1 (0.5 mg/mL). The absorbance spectrum (purple curve) displays a characteristic peak at λ = ~ 280 nm. The fluorescence spectra were obtained for RfA1 (0.5 mg/mL) at pH 6.3 (orange curve), pH 2.8 (red curve), and at a temperature of 100°C (green curve) (excitation wavelength of λ = 282 nm). There is virtually no change in the fluorescence spectra with a change in pH (red curve) or temperature (green curve), indicating RfA1 maintains its conformation. However, upon addition of GdnHCl (blue curve), the fluorescence spectrum maximum shifts to λ = ~ 347 nm and a new peak appears at λ = ~ 300 nm. Absorbance at λ = ~ 300 nm is characteristic of solution exposed tyrosine residues, i.e. RfA1 denaturation.

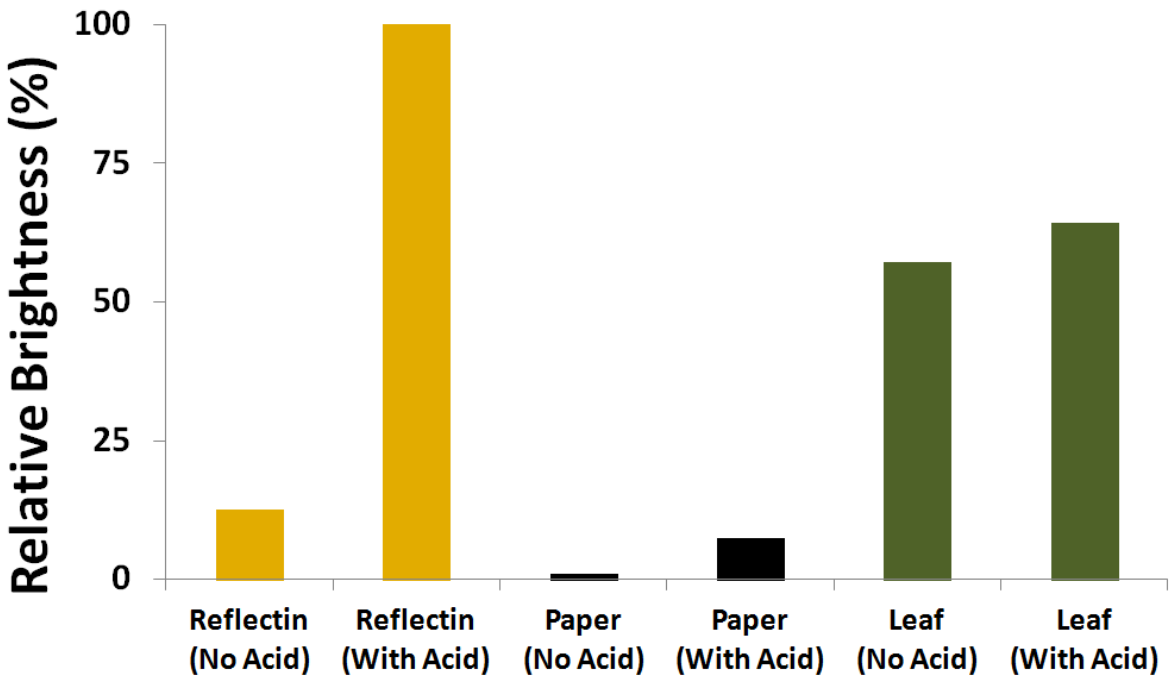

Figure S2.11: Integrated infrared brightness values measured for an RfA1 film, a piece of paper, and a Buxus plant leaf in the presence and absence of acetic acid vapor. The values were extracted by analyzing Figure 3B in the main text and normalized to the maximum brightness.

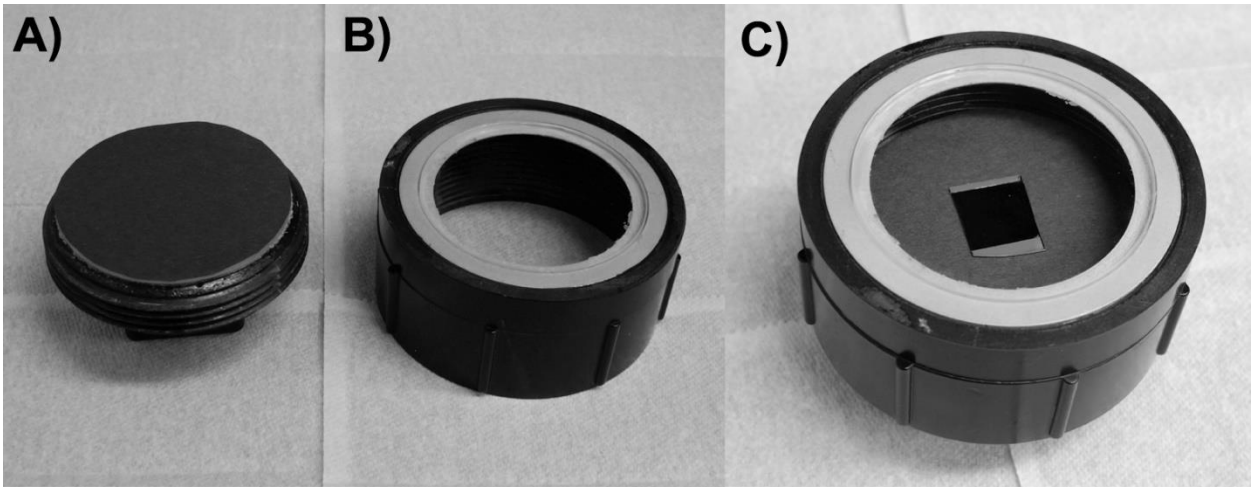

Figure S2.12: Pictures of the housing used for exposure of the RfA1 coated substrates to acetic acid vapor. A) The bottom part of housing. B) The top part of housing. C) The integrated housing containing an RfA1 coated substrate.

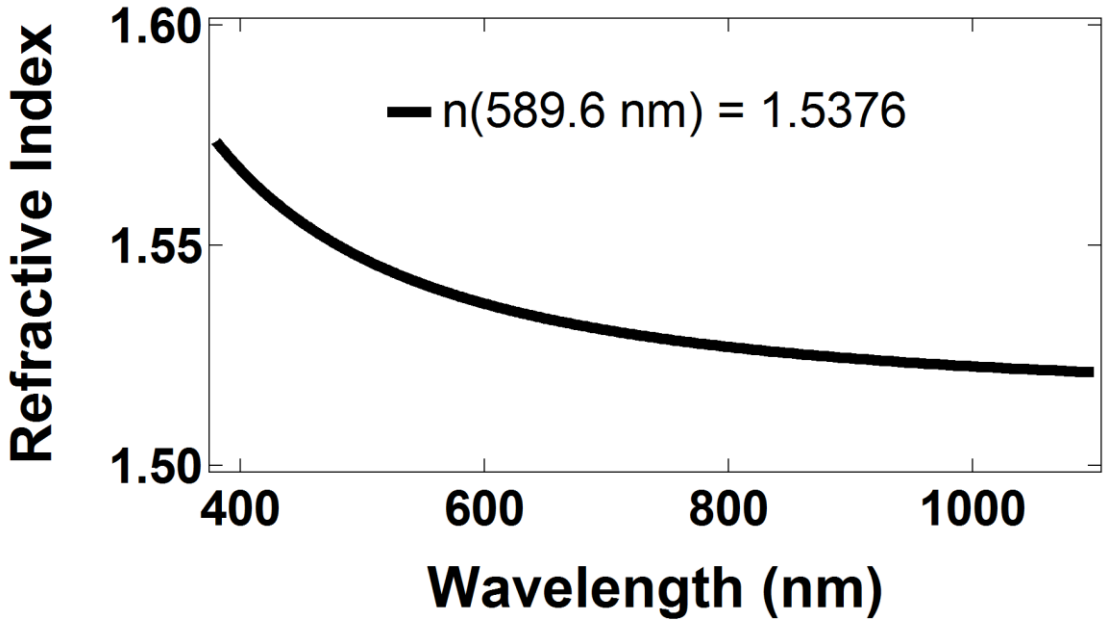

Figure S2.13: The refractive index of the RfA1 films measured at Filmetrics (San Diego, CA) using a Filmetrics F20-UV spectrometer with a deuterium and tungsten-halogen white light source (effective wavelength range of λ = 200 nm to λ = 1100 nm). The refractive index was measured at λ = 632.8 nm with a resolution less than 1 nm. The data was acquired normal to the substrate surface.

2.6 Acknowledgements

This chapter is an adaptation of the material as it appears in: L. Phan, W. G. Walkup IV, D. D. Ordinario, E. Karshalev, J.-M. Jocson, A. M. Burke, A. A. Gorodetsky, *Adv. Mater.*. 2013, **25**, 5621–5625. The co-authors listed in this publication directed and supervised research which forms the basis for the material in the chapter. Author Contributions: L. P. and A. A. G. conceptualized and designed the experiments; L. P., W. G. W. IV, D. D. O., E. K., and J.-M. J. performed the research; L. P. and W. G. W. IV designed the genes, cloned the genes, expressed the protein, and purified the protein; L. P. and A. A. G. analyzed the data; thoughtful conversation was carried out with A. M. B., and L. P. and A. A. G. wrote the paper.

2.7 References

1. S. Kinoshita, S. Yoshioka, Structural Colors in Biological Systems: Principles and Applications, Osaka University Press, Osaka, 2005.
2. P. Vukusic, J. R. Sambles, *Nature* 2003, **424**, 852–855.
3. P. Ball, *Sci. Am.* 2012, **306**, 74–79.
4. A. Saito, *Sci. Technol. Adv. Mater.* 2011, **12**, 064709/1–064709/13.
5. Y. Zhao, Z. Xie, H. Gu, C. Zhu, Z. Gu, *Chem. Soc. Rev.* 2012, **41**, 3297–3317.
6. H. Fudouzi, *Sci. Technol. Adv. Mater.* 2011, **12**, 064704/1–064704/7.
7. S. P. Mahulikar, H. R. Sonawane, G. A. Rao, *Prog. Aerosp. Sci.* 2007, **43**, 218–245.
8. V. Rubeziene, G. Minkuviene, J. Baltusnikaite, I. Padleckiene, Mater. Sci. 2009, 15, 173–177.
9. S. M. Burkinshaw, G. Hallas, A. D. Towns, *Rev. Prog. Color. Relat. Top.* 1996, **26**, 47–53.
10. S. Daehne, U. Resch-Genger, O. S. Wolfbeis, eds, Near-Infrared Dyes for High Technology Applications, Vol. **52**, Kluwer Academic Publishers, Dordrecht, 1998.
11. E. Kreit, L. M. Mäthger, R. T. Hanlon, P. B. Dennis, R. R. Naik, E. Forsythe, J. Heikenfeld, *J. R. Soc. Interface* 2012, **10**, 1–13.
12. L. M. Mäthger, E. J. Denton, N. J. Marshall, R. T. Hanlon, *J. R. Soc. Interface* 2009, **6**, 149–163.
13. W. J. Crookes, L. L. Ding, Q. L. Huang, J. R. Kimbell, J. Horwitz, M. J. McFall-Ngai, *Science* 2004, **303**, 235–238.
14. R. M. Kramer, W. J. Crookes-Goodson, R. R. Naik, *Nat. Mater.* 2007, **6**, 533–538.

15. A. R. Tao, D. G. DeMartini, M. Izumi, A. M. Sweeney, A. L. Holt, D. E. Morse, *Biomaterials* 2010, **31**, 793–801.
16. M. Izumi, A. M. Sweeney, D. G. DeMartini, J. C. Weaver, M. L. Powers, A. R. Tao, T. V. Silvas, R. M. Kramer, W. J. Crookes-Goodson, L. M. Mäthger, R. R. Naik, R. T. Hanlon, D. E. Morse, *J. R. Soc. Interface* 2010, **7**, 549–560.
17. G. Qin, P. B. Dennis, Y. Zhang, X. Hu, J. E. Bressner, Z. Sun, W. J. Crookes-Goodson, R. R. Naik, F. G. Omenetto, D. L. Kaplan, *J. Polym. Sci. Polym. Phys.* 2013, **51**, 254–264.
18. D. G. DeMartini, D. V. Krogstad, D. E. Morse, *Proc. Natl. Acad. Sci. USA* 2013, **110**, 2552–2556.
19. L. M. Mäthger, R. T. Hanlon, *Cell Tissue Res.* 2007, **329**, 179–186.
20. D. R. Dreyer, S. Park, C. W. Bielawski, R. S. Ruoff, *Chem. Soc. Rev.* 2010, **39**, 228–240.
21. Y. Wang, Z. Li, J. Wang, J. Li, Y. Lin, *Trends Biotechnol.* 2011, **29**, 205–212.
22. H. A. MacLeod, Thin-Film Optical Filters, 3rd ed., Taylor & Francis, Boca Raton, 2001.
23. T. E. Creighton, Proteins: Structures and Molecular Properties, 2nd ed., W. H. Freeman & Co., New York, 1993.
24. Y. Kang, J. J. Walish, T. Gorishnyy, E. L. Thomas, *Nat. Mater.* 2007, **6**, 957–960.
25. C. Kang, E. Kim, H. Baek, K. Hwang, D. Kwak, Y. Kang, E. L. Thomas, *J. Am. Chem. Soc.* 2009, **131**, 7538–7539.
26. D. Kaplan, K. McGrath, in *Protein-Based Materials – Bioengineering of Materials*, Birkhäuser, Boston, **1996**.
27. J. J. Walish, Y. Kang, R. A. Mickiewicz, E. L. Thomas, *Adv. Mater.* 2009, **21**, 3078–3081.
28. E. Kim, C. Kang, H. Baek, K. Hwang, D. Kwak, E. Lee, Y. Kang, E. L. Thomas, *Adv. Funct. Mater.* 2010, **20**, 1728–1732.

29. E. P. Chan, J. J. Walish, E. L. Thomas, C. M. Stafford, *Adv. Mater.* 2011, **23**, 4702–4706.

30. Y. Ahn, E. Kim, J. Hyon, C. Kang, Y. Kang, *Adv. Mater.* 2012, **24**, 127–130.

31. H. S. Lim, J. H. Lee, J. J. Walish, E. L. Thomas, *ACS Nano.* 2012, **6**, 8933–8939.

32. K. Svennersten, K. C. Larsson, M. Berggren, A. Richter–Dahlfors, *Biochim. Biophys. Acta* **2011**, *1810*, 276–285.

33. A. Lipson, S. G. Lipson, H. Lipson, *Optical Physics*, 4th ed., Cambridge University Press, Cambridge, **2010**.

CHAPTER 3 Infrared Invisibility Stickers Inspired by Cephalopods

3.1: Abstract

The skin morphology of cephalopods endows them with remarkable dynamic camouflage capabilities. Cephalopod skin has therefore served as an inspiration for the design of camouflage devices that function in the visible region of the electromagnetic spectrum. In contrast, despite the importance of infrared signaling and detection for numerous industrial and military applications, there have been fewer attempts to translate the principles underlying cephalopod adaptive coloration to infrared camouflage systems. Herein, we draw inspiration from the structures and proteins found in cephalopod skin to fabricate biomimetic camouflage coatings on transparent and flexible adhesive substrates. The substrates can be deployed on arbitrary surfaces, and we can reversibly modulate their reflectance from the visible to the near infrared regions of the electromagnetic spectrum with a mechanical stimulus. These stickers make it possible to disguise common objects with varied roughnesses and geometries from infrared visualization. Our findings represent a key step towards the development of wearable biomimetic color- and shape-shifting technologies for stealth applications.

3.2: Introduction

Cephalopods, such as the squid *Doryteuthis* (*Loligo*) *pealeii* and the cuttlefish Sepia officinalis, are renowned as masters of disguise.[1–5] These animals can alter their patterning, coloration, shape, and texture, enabling them to emulate nearly any object or environment.[1–5] Cephalopods' remarkable camouflage capabilities stem from the unique organization of their skin, which consists of transparent dermal layers containing cells known as iridophores, leucophores, and chromatophores.[1–5] These cells function in concert to control cephalopod skin coloration, with

the iridophores/leucophores modulating the reflection of light and the chromatophores modulating the transmission of light.[2,6–8] Moreover, the mechanical flexibility of the dermal layers affords an additional level of control by allowing cephalopods to reconfigure their skin morphology in three dimensions.[9,10] The sophisticated natural design of cephalopod skin thus gives it remarkable dynamic adaptability, which is enviable from the viewpoint of both artificial and natural systems.

The mechanisms that cephalopods employ to induce optical changes in iridophores and chromatophores are particularly fascinating. Iridophores are actuated primarily via chemical means.[1–8] The iridophores' plasma membrane folds to encompass lamellar-like platelets from a protein known as reflectin,[11–18] which alternate with extracellular space to form Bragg reflector-type structures. Reversible phosphorylation of reflectin changes the size and spacing of the lamellae that make up the reflectors, dynamically shifting the iridophores' coloration across the visible spectrum.[11–18] On the other hand, chromatophores are actuated primarily via mechanical means.[1–8] Chromatophores contain a network of tethered, reflectin-filled pigment granules and are fringed by radial muscle fibers, which expand these cells from barely visible spherical points to thin colored plates.[6–8,19] This areal expansion enables chromatophores to function as dynamic spectral filters. The unique properties of iridophores and chromatophores have inspired efforts seeking to develop biomimetic camouflage that functions not only in the visible[20–24] but also in the infrared[18] regions of the electromagnetic spectrum.

Herein, we draw inspiration from cephalopod skin and introduce a new type of reflectin-based, mechanically-reconfigurable infrared camouflage. We first use standard film fabrication protocols to coat conformable and adhesive fluorinated ethylene propylene (FEP) tape[25–27] with reflectin; the reflectance of the resulting substrates can span both the visible and infrared regions of the electromagnetic spectrum. We then use the coated tape to endow fabrics with predetermined

infrared reflective patterning. We subsequently modulate the coloration of our substrates between the near infrared and the visible with a simple mechanical stimulus. Finally, we show that the mechanically-deformed reflectin-coated substrates can be returned to their initial state through gentle heating. In their totality, our findings constitute a foundation for the next generation of color- and shape-shifting infrared camouflage systems.

3.3: Results and Discussion

We began our studies by heterologously expressing a histidine-tagged *Doryteuthis* (*Loligo*) *pealeii* reflectin A1 isoform in *E. coli* according to previously reported protocols.[17,18] We first extracted crude reflectin from *E. coli* inclusion bodies. The protein was then sequentially purified by immobilized metal affinity chromatography under denaturing conditions and high performance liquid chromatography (HPLC). The identity of the purified protein was confirmed by in-gel tryptic digestion and tandem mass spectrometry. Notably, our optimized expression and purification procedure yielded ~1 g of reflectin per liter of *E. coli* cell culture, with a purity of over 99%. This high yield and excellent purity facilitated subsequent fabrication of protein-based coatings on flexible substrates.

We adapted our previously established procedures[17,18] to fabricate reflectin films on FEP substrates. We specifically chose FEP as the substrate due to its transparency, chemical inertness, flexibility, conformability, temperature stability, and tensile strength.[25–27] Moreover, FEP is commercially available as a sticky tape, with an adhesive layer on one side, making it straightforward to bond this material to arbitrary objects (Figure 3.1A). In brief, we first coated a thin layer (<5 nm) of graphene oxide directly onto the FEP tape, forming negatively-charged and amphiphilic surfaces that were well suited for the assembly of positively-charged reflectin (Figure

3.1B). We then used a modified doctor blade approach to spread reflectin directly onto the graphene oxide-coated surfaces (Figure 3.1B). This process enabled the fabrication of relatively uniform reflectin films on adhesive polymer substrates (Figure 3.2 and Figure S3.1).

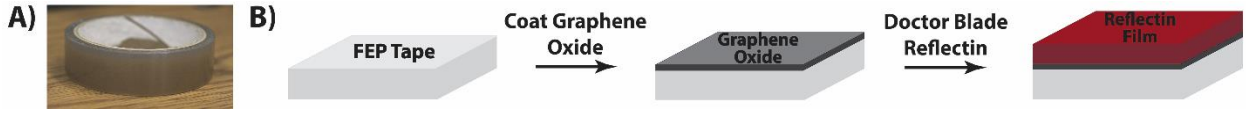

Figure 3.1: A) A picture of a commercially available roll of FEP tape. B) A schematic of the fabrication of reflectin films on flexible FEP substrates. The process consists of depositing negatively-charged graphene oxide onto the tape, followed by doctor blading of positively-charged reflectin directly onto this modified surface.

Next, we investigated and characterized the optical properties of the coated tape. Figure 3.2 shows an optical image and a corresponding reflectance spectrum obtained for a typical reflectin film on FEP. This substrate featured blue coloration over an area of square centimeters, with a peak reflectance wavelength of ~400 nm. The peak reflectance corresponded to a theoretical reflectin film thickness of ~65 nm, which was in excellent agreement with the experimentally measured value of ~64 nm. Our analysis indicated that the reflectance of the coated tape was governed by well-known thin film interference theory (see Figure S3.2 and Supplementary Information for calculation details).[28]

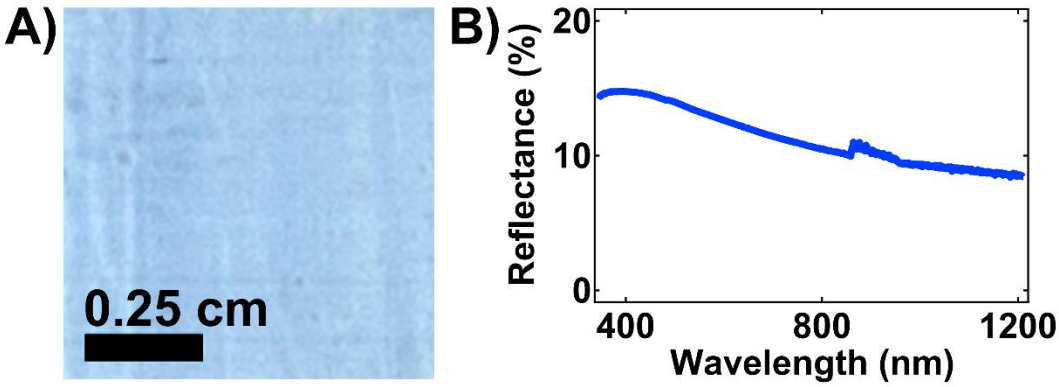

Figure 3.2: A) A large area optical camera image of a typical blue reflectin-coated FEP substrate. B) The corresponding reflectance spectrum for the substrate, with a peak reflectance wavelength of ~400 nm. The reflectin film thickness was ~64 nm, as determined by atomic force microscopy.

Guided by our initial studies, we next prepared infrared-reflecting substrates by fabricating thicker reflectin films on FEP tape. Figure 3.3A shows one such substrate, which has been adhered to a glass slide as a demonstration of its transparency (note that the underlying camouflage pattern is clearly visible). The reflectance spectrum of this ~163 nm-thick film on FEP featured a peak wavelength of ~1030 nm (Figure 3.3B), indicating that the coloration of the coated substrates could be readily shifted into the near infrared simply by increasing the reflectin films' thickness.

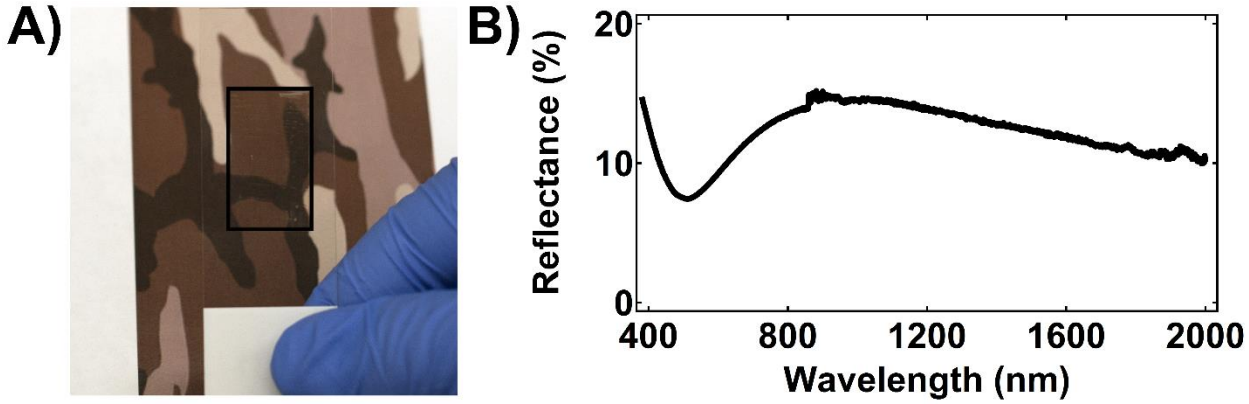

Figure 3.3: A) An optical camera image of a typical clear reflectin-coated FEP substrate. The coated tape, which is indicated by the black box, has been adhered to a glass slide, and the underlying camouflage pattern is visible, demonstrating the substrate's transparency. B) The corresponding reflectance spectrum for the substrate, with a peak reflectance of ~1030 nm in the near infrared region of the electromagnetic spectrum. The reflectin film thickness was ~163 nm, as determined by atomic force microscopy.

We proceeded to demonstrate that our reflectin-coated FEP tape could enhance the camouflage properties of any object under infrared visualization. Here, we sought inspiration from the organization of cephalopod skin, where different arrangements of ellipsoidal chromatophores lead to a virtually unlimited array of colors and geometric patterns.[1–8] Thus, we decided to modify cloth from a camouflage fatigue with a predetermined infrared-reflecting pattern fashioned from the reflectin-coated FEP tape.

For these experiments, we visualized our substrates with an optical camera under either white light or infrared light illumination. Figure 3.4A shows an optical camera image of camouflage cloth modified with three different types of objects. The cloth featured an adhered

rectangular piece of FEP tape without a reflectin coating (Figure 3.4A, left), an adhered checkerboard pattern of five infrared-reflecting FEP tape squares with a reflectin coating (Figure 3.4A, middle), and a plant leaf (Figure 3.4A, right). The uncoated and reflectin-coated pieces of FEP tape appeared clear and were difficult to distinguish from one another. However, all six pieces of tape were quite distinct from the green plant leaf. Figure 3.4B shows an infrared image obtained of the same camouflage cloth. Under infrared visualization, the uncoated FEP tape (Figure 3.4B, left) and the underlying fatigue were effectively no longer visible, while the checkerboard pattern of reflectin-coated FEP tape (Figure 3.4B, middle) and the leaf (Figure 3.4B, right) were quite distinct and appeared bright. Together, these images indicated that our reflectin-coated FEP tape could be deployed to produce infrared-reflective patterning on objects with virtually any shape, roughness, geometry, or size.

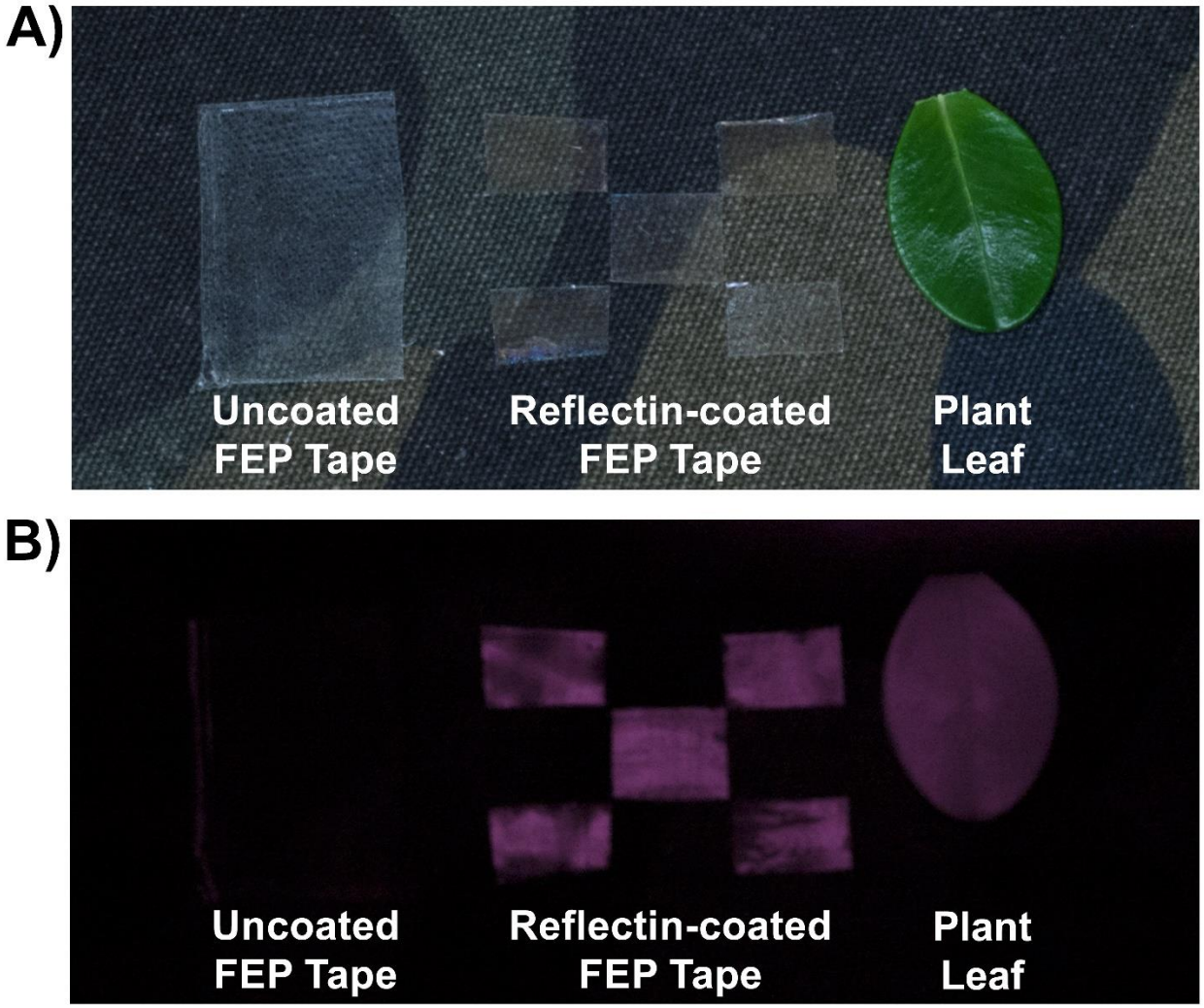

Figure 3.4: A) An optical camera image of a camouflage fatigue modified with an adhered piece of FEP tape without reflectin (left), an adhered checkerboard pattern of five reflectin-coated FEP tape squares (middle), and a plant leaf (right). Note that the uncoated tape on the left and the reflectin-coated tape in the middle appear similar. B) An infrared camera image of the same camouflage fatigue under infrared illumination. Note that the infrared-reflecting checkerboard pattern (middle) and the infrared-reflecting leaf (right) are visible while the uncoated FEP tape (left) cannot be readily distinguished from the background.

We next demonstrated that a simple exogenous stimulus could modulate the coloration and reflectance of our coated substrates. Here, we drew inspiration both from the previous demonstrations of mechanochromism for photonic gels[29–31] and from the function of reflectin-containing pigment granule networks found in chromatophores, which cephalopods dynamically expand and contract to alter the patterning and coloration of their skin.[19] Thus, we investigated the effect of an applied strain on the optical properties of our reflectin-coated FEP tape.

Figure 3.5 shows camera images of a piece of reflectin-coated FEP tape (positioned on top of a camouflage fatigue) in the absence of an applied uniaxial strain. Under optical imaging conditions, the coated substrate appeared clear, and the underlying fatigue was readily visible (Figure 3.5A). However, under infrared imaging conditions, the substrate appeared bright, and the underlying camouflage fatigue appeared dark, effectively functioning as an internal standard (inset of Figure 3.5A). As expected, the unstrained tape possessed a reflectance peak in the near infrared region of the electromagnetic spectrum, which was centered at ~980 nm (Figure 3.5B). This peak reflectance wavelength corresponded to a theoretical reflectin film thickness of ~162 nm, which was in good agreement with the experimentally measured value of ~160 nm.

Figure 3.5 also shows camera images of the same piece of reflectin-coated FEP tape, where the tape has been subjected to a uniaxial strain (tension) ε_x of ~0.57. Under optical imaging conditions, the coated substrate acquired an orange color, and the underlying camouflage fatigue was obscured (Figure 3.5C). Moreover, under infrared imaging conditions, the brightness of the tape was reduced by ~40% (inset of Figure 3.5C). The strained tape now featured a blue-shifted peak reflectance wavelength of ~705 nm in the visible region of the electromagnetic spectrum (Figure 3.5D). The peak reflectance wavelength corresponded to a theoretical reflectin film thickness of ~116 nm, which was in good agreement with the experimentally measured value of ~120 nm.

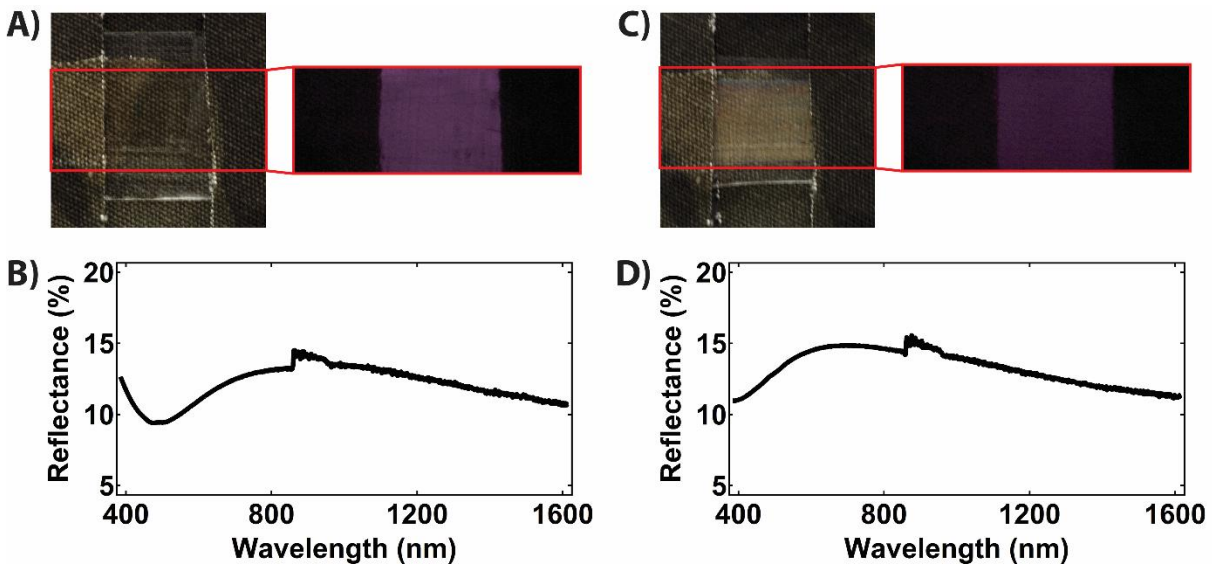

Figure 3.5: A) An optical camera image of a camouflage fatigue overlaid with a piece of reflectin-coated FEP tape in the absence of uniaxial strain. The tape is transparent, enabling visualization of the underlying fatigue. The inset shows an infrared image of a portion of the tape-modified fatigue (indicated by the red box). Note that the unstrained infrared-reflecting tape appears bright under infrared visualization. The unstrained reflectin film thickness was ~160 nm, as determined by atomic force microscopy. B) The corresponding reflectance spectrum for the reflectin-coated FEP tape in the absence of uniaxial strain. The peak reflectance lies in the near infrared at ~980 nm. C) An optical camera image of the same camouflage fatigue and reflectin-coated FEP tape in the presence of uniaxial strain. The tape is no longer transparent and appears orange, obscuring the underlying fatigue. The inset shows an infrared image of a portion of the tape-modified fatigue (indicated by the red box). Note that the strained infrared-reflecting tape is more difficult to see and appears dark under infrared visualization. The strained reflectin film thickness was ~120 nm, as determined by atomic force microscopy. D) The corresponding reflectance spectrum for the reflectin-coated FEP tape in the presence of uniaxial strain. The peak reflectance lies in the visible at ~705 nm, in agreement with the blue shift of the substrate's coloration.

Based on our measurements and observations, we propose a simple model that accounts for the strain-dependent optical properties of reflectin-coated FEP substrates, as illustrated in Figure 3.6. Given that aggregated reflectin's behavior resembles that of a gel phase,[13] the application of a uniaxial strain (tension) to the reflectin-coated FEP tape stretches not only the relatively rigid tape but also the softer overlaid film.[29] Therefore, under a strain of $\varepsilon x = \Delta L/L$, the film will be elongated by a factor of $1 + \varepsilon$, from L to $L + \Delta L$ (where L is the initial length and ΔL is the change in length) (Figure 3.6).[32] Due to the Poisson effect, the reflectin film's thickness will simultaneously decrease by a factor of $1 - \nu\varepsilon$, from t to $t - \Delta t$ (where t is the initial thickness, Δt is the change in thickness, and ν is Poisson's ratio) (Figure 3.6).[32] Indeed, for the film in Figure

3.5, the strain of εx = ~0.57 was accompanied by a reduction in thickness of ~25%. This experimental thickness decrease was in agreement with the theoretically predicted one of ~27% (assuming a nearly ideal Poisson's ratio of 0.48).[25–27] Overall, our calculations indicated that the above straightforward model, in conjunction with thin film interference theory, accurately described the optomechanical behavior of reflectin-coated FEP substrates.

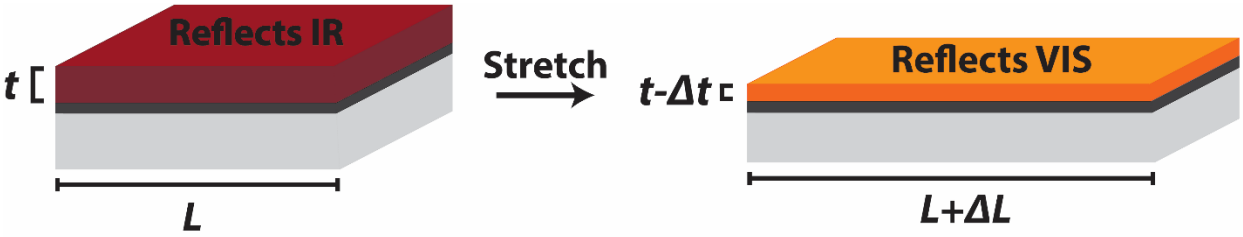

Figure 3.6: Schematic of the postulated mechanism that underlies the coloration changes for mechanically strained reflectin-coated FEP substrates. The application of a uniaxial strain (tension) εx induces an increase in the length of the reflectin film from L to L + ΔL and a decrease in the film's thickness from t to t − Δt, as dictated by the Poisson effect. Under tension, the color and reflectance spectrum of the coated substrate display a blue shift.

To demonstrate the general applicability of our approach, we also explored the possibility of modulating the reflectance of our strained (and deformed) reflectin films with alternative stimuli. These experiments were inspired by the general mechanical flexibility and malleability of cephalopod skin.[1–8] Here, we were gratified to discover that gentle annealing with a heat gun returned our plastically deformed FEP substrates (and presumably the overlaid reflectin films) to their initial, unstretched state (Figure S3.3). This change in substrate geometry was accompanied by a shift of the coloration (and reflectance) back from the visible to the near infrared (Figure S3.3). In essence, our deformed reflectin films could be “healed” with an exogenous stimulus to recover their original optical properties.

3.4: Conclusion

In summary, we have introduced a new biomimetic infrared camouflage system, which possesses a number of potentially favorable and unique features. First, our readily-accessible fabrication strategy relies upon commercial materials and does not require specialized facilities or equipment, making it straightforward to coat optically-uniform, infrared-reflecting films on flexible substrates over square centimeter areas. Second, the reflectin-coated FEP substrates are adhesive, soft, and conformable, so they can be applied to surfaces or objects with varied roughnesses, shapes, sizes, and geometries, much like common household tape or stickers. Third, the breadth of the reflectance peaks for our coated substrates ensures that their appearance will be only weakly dependent on the viewing angle under infrared visualization, which may prove advantageous in certain stealth situations. Fourth, the effective visibility of the reflectin-coated substrates, when imaged under either white light or infrared light illumination, can be tuned via the application of a uniaxial strain, rather than a harsh chemical stimulus.[18] We are aware of no other examples where a soft material's infrared reflectance is modulated between the visible and the infrared via the application of exogenous mechanical stimuli. Fifth, the substrates can be returned to their initial state through gentle heating, laying the groundwork for the development of damage-resistant infrared camouflage devices that respond to multiple stimuli. Finally, our work constitutes a rare example of the translation of cephalopod adaptive coloration principles specifically to infrared, rather than visible, camouflage.[18] Indeed, the dearth of previous literature precedent in this area is quite unexpected given the widely acknowledged importance of infrared signaling and detection for industrial and military applications.[33–38] Based on the above considerations, our mechanically reconfigurable infrared invisibility stickers may represent a

significant step forward on the path to biomimetic adaptable optical devices and disposable camouflage technologies.

3.5 Supplementary Information

Design and Cloning of the Reflectin A1 Gene: An *E. coli* codon optimized gene coding for 6x histidine tagged wild type reflectin A1 protein from *Doryteuthis* (formerly *Loligo*) *pealeii* (Genbank: ACZ57764.1) was synthesized and cloned into pJExpress414 vector (DNA2.0).

Expression and Purification of Reflectin A1: A general previously reported protocol was used for the expression and purification of wild-type wild type reflectin A1[17,18]. In brief, the pJExpress414 expression vectors containing wild type wild-type reflectin were transformed into BL21(DE3) cells (Novagen). Reflectins were expressed at 37 °C using Overnight Express Instant Terrific Broth (TB) media (Novagen) supplemented with 100 μg mL^{-1} Carbenicillin. Reflectin was completely insoluble when expressed at 37 °C and was sequestered in inclusion bodies prepared using Novagen BugBuster® according to the manufacturer's suggested protocol. Reflectin inclusion bodies were then solubilized in denaturing buffer (pH 7.4, 50 mM Sodium Phosphate, 300 mM NaCl, 6M guanidine hydrochloride) and purified under denaturing conditions on HisPur Cobalt Resin (Thermo Scientific) immobilized metal affinity chromatography (IMAC) gravity columns according to the manufacturer's protocols. The protein was eluted by using denaturing buffer supplemented with 250 mM imidazole. The fractions containing reflectin were pooled and concentrated on Millipore Amicon Concentrators before further purification with high-performance liquid chromatography (HPLC) on an Agilent 1260 Infinity system using an Agilent reverse phase C18 column with a gradient evolved from 95% Buffer A:5% Buffer B to 5% Buffer

A:95% Buffer B at a flow rate of 1 mL min^{-1} over 30 minutes (Buffer A: 99.9% H2O, 0.1% TFA; Buffer B: 95% acetonitrile, 4.9% H2O, 0.1% TFA). The pure reflectin fractions were pooled, flash frozen in liquid nitrogen, and lyophilized. Protein concentrations and yields were quantified via a Bradford protein assay with bovine serum albumin (BSA) as a standard (BioRad).

Characterization of Reflectin A1: A general previously reported protocol was used for assaying the purity and confirming the sequence of reflectin A1[17,18]. In brief, purified and unpurified reflectin samples were analyzed by SDS-PAGE and GelCode Blue Staining (Thermo) using an Invitrogen XCell SureLock Mini using NuPAGE Novex 4-12% Bis-Tris gels, with NuPAGE MOPS as the running buffer under reducing conditions. Stained protein bands were subjected to in-gel tryptic digestion, performed according to literature procedures[17,18]. After digestion, the peptides were separated on a C18 chromatography column and analyzed by mass spectrometry on a Thermo Orbitrap instrument outfitted with an electrospray ionization source. The resulting sequence coverage was 94% for the wild type wild-type reflectin A1.

Fabrication of Reflectin-Coated Fluorinated Ethylene Propylene Substrates: In a typical procedure, a strip of Fluorinated Ethylene Propylene (FEP) tape (McMaster-Carr) was first adhered to a glass substrate (Fisher), in preparation for coating. Spacer rails of Teflon tape (McMaster-Carr) were then applied to the edges of the FEP tape. The tape was in turn coated with graphene oxide (Graphene Marketplace) on a hot plate at 60 ºC to provide an adhesion layer for the protein. The reflectin protein solution was cast onto the FEP tape in front of the blade, which was translated at a constant speed across the surface to produce thin films. To promote water

evaporation and uniform film formation, the coating procedure was performed at 80 °C. The film thickness was controlled by varying the reflectin concentration.

Atomic Force Microscopy Characterization of Reflectin-Coated Substrates: The thicknesses of all reflectin films were measured with atomic force microscopy (AFM) by examining trenches scribed directly into the films. Topographical images were also collected to confirm uniformity for all substrates. The measurements were performed with iridium coated silicon probes (Asylum Research ASYELEC-01) with a spring constant of 2 N m^{-1}, resonance frequency of 70 kHz, and tip radius of 28 nm were used. The scans were rastered either at 0.17 Hz or at 1.0 Hz and normalized using polynomial subtraction for improved image quality; typical AFM topography scans for blue and yellow reflectin films are shown in Supplementary Figure S3.1.

Optical Characterization of Reflectin-Coated Substrates: The reflectin-coated substrates were characterized with optical microscopy and reflectance measurements according to established protocols.[18] Optical images were obtained on a Carl Zeiss Axio Imager A1M microscope (outfitted with a Epiplan 20X lens, NA = 0.4) and processed with the manufacturer's AxioVision AC4.5 software. Reflectance spectra were measured in the presence and absence of applied strain on one of three instruments: 1) an Ocean Optics SD2000 Miniature Fiber Optic Spectrometer, outfitted with an LS-1 tungsten-halogen white light source and a R400-7 Reflection/Backscattering Probe (effective wavelength range of λ = 340 nm to λ = 950 nm); 2) a Perkin-Elmer Lambda 950 Spectrometer, outfitted with deuterium and tungsten-halogen white light sources and a 60 mm integrating sphere (effective wavelength range of λ = 190 nm to λ = 3300 nm); and 3) a Filmetrics F40-NSR microscope system, outfitted with a Tungsten-Halogen white light source (effective

wavelength range of λ = 400 nm to λ = 800 nm). Measurements on the Filmetrics F40-NSR microscope system allowed for confirmation of the film thickness determined by AFM and profilometry. The integrating sphere reflectance data were acquired 8º to the substrate surface at the reflectance port, and all measurements were referenced to a SpectraLabs Spectralon standard (unless otherwise noted).

Detailed Description of the Reflectin Film Thickness Calculations: The theoretical film thicknesses were calculated based on thin-film interference theory[25,26]. Our system closely follows the well-known oil on water example due to reflectin's refractive index of ~1.54 and FEP's refractive index of ~1.33.[25,26] Thus, at non-normal incidence, the reflected light obeys the formula:

$$\left(m - \frac{1}{2}\right) * \lambda = 2 * n * d * \cos(\beta)$$

where *m* is an integer that describes wavelength order, λ is the peak reflected wavelength, *n* is the refractive index of the film, *d* is the film thickness, and β is the angle in the film (Supplementary Figure S3.2). The graphene oxide adhesion layer used in our experiments was very thin, so it did not dramatically influence the calculated values. The refractive indices used for the calculations were obtained from the literature[25,26] and confirmed at Filmetrics (San Diego, CA) using a Filmetrics F20-UV spectrophotometer.

Description of the Imaging and Stretching Experiments: The reflectin and graphene oxide-coated FEP tape was separated from the glass slide and mounted on two anchoring substrates. The camouflage patterned fabric was placed underneath the film as well as on the sides of it in order to highlight only the active area of the film. The film was first imaged in the absence of strain and with a standard camera under white light illumination, then with an infrared camera under infrared

light illumination. The infrared imaging experiments employed a Nikon D-70 camera equipped with a 35 50 mm f/1.8 AF-S DX Lens (Nikon) and a 52 mm RM-72 infrared filter (Hoya). The infrared illumination light source consisted of a home-built 26 LED array (XtraLED). The images were captured with an exposure time of 5 seconds, aperture setting of f/8, and ISO of 200. The film was then stretched, inducing a uniaxial strain (tension). The film was subsequently imaged again with standard and infrared cameras, as described above.

Description of the Heat Regeneration Experiments: The reflectin and graphene oxide-coated FEP tape was separated and stretched as described above. After the final desired strain was reached, the anchoring substrates were unlocked and the sample was regenerated via gentle heating (Grizzly Industrial, Inc., model H0800) for a maximum duration of 2 seconds at low setting.

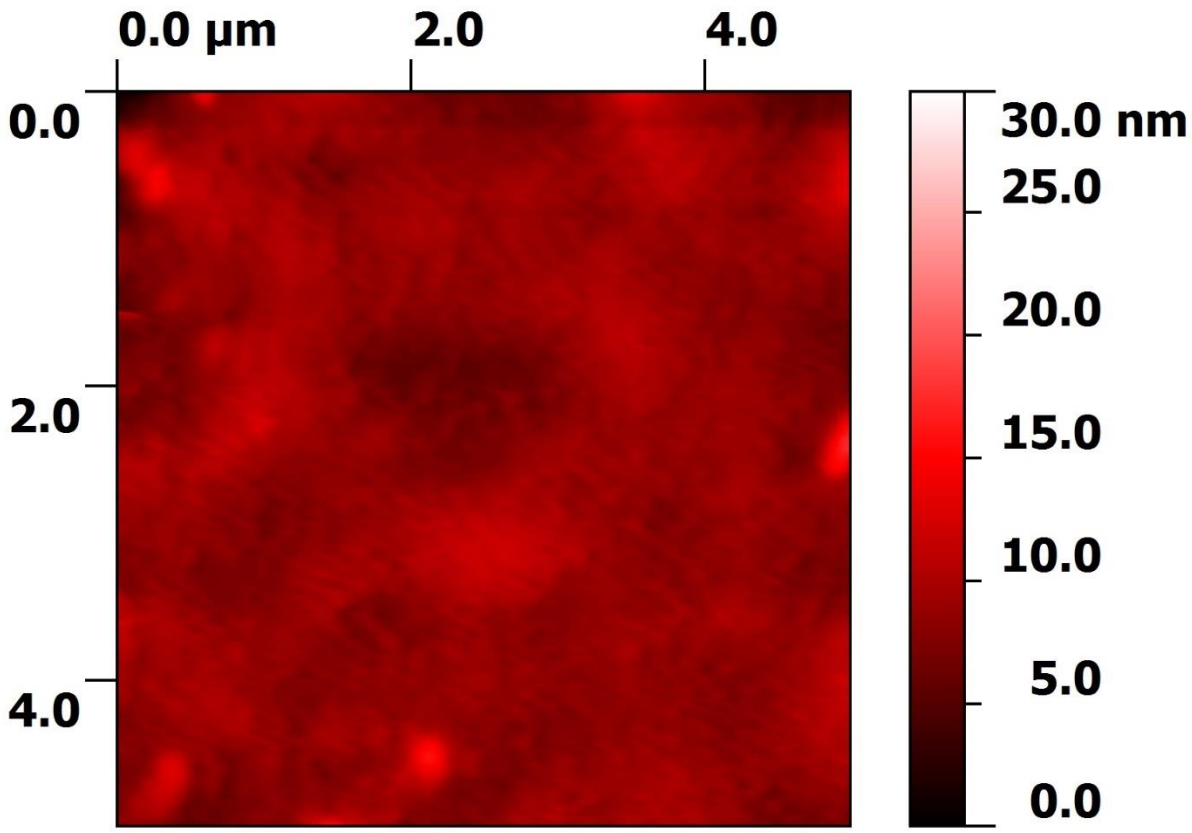

Figure S3.1: A typical atomic force microscopy images for a reflectin film on fluorinated ethylene propylene substrate. The film corresponds to Figure 3.2 in the main text. The rms roughness was ~ 1.5 nm.

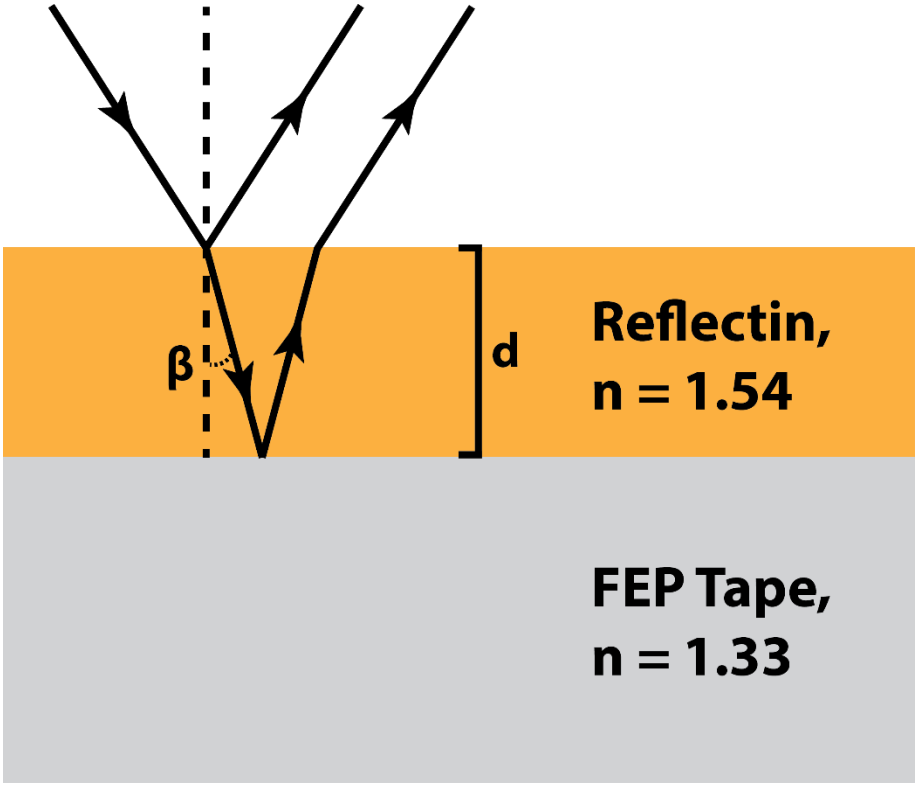

Figure S3.2: Schematic of the thin film interference that occurs in the reflectin film and FEP tape system, which shares similar refractive index values to the classic oil on water example. λ (not shown) is the peak reflected wavelength, *n* is the refractive index of the film, *d* is the film thickness, and β is the angle of reflected light in the film.

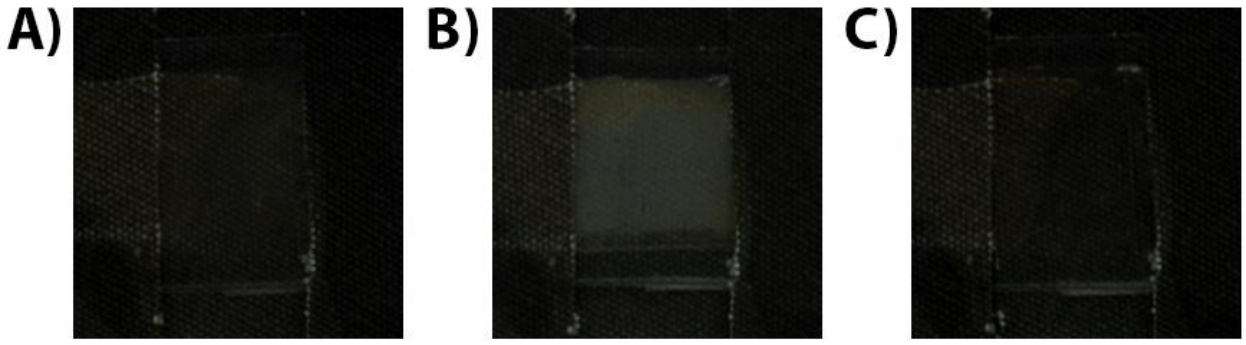

Figure S3.3: A) A standard camera image of a camouflage fatigue overlaid with a piece of reflectin-coated fluorinated ethylene propylene tape in the absence of uniaxial strain. The tape is transparent and nearly invisible, enabling visualization of the underlying fatigue. B) A standard camera image of the same camouflage fatigue and reflectin-coated fluorinated ethylene propylene tape in the presence of uniaxial strain. The tape is no longer transparent and appears colored, obscuring the underlying fatigue. C) A standard camera image of the same camouflage fatigue and reflectin-coated fluorinated ethylene propylene tape in the absence of uniaxial strain after gentle heating at 60°C using a heat gun. The tape has recovered its transparency, again enabling visualization of the underlying fatigue.

3.6: Acknowledgements

This chapter is an adaptation of the material as it appears in: L. Phan, D. D. Ordinario, E. Karshalev, W. G. Walkup IV, M. A. Shenk, A. A. Gorodetsky, *J. Mater. Chem. C* 2015, **3**, 6493-6498. The co-authors listed in this publication directed and supervised research which forms the basis for the material in the chapter. Author Contributions: L. P. and A. A. G. conceptualized and designed the experiments; L. P., D. D. O., E. K., W. G. W. IV, and M. A. S. performed the research; L. P. and W. G. W. IV designed the genes, cloned the genes, expressed the protein, and purified the protein; L. P. and A. A. G. analyzed the data; and L. P. and A. A. G. wrote the paper.

3.7: References

1. E. Kreit, L. M. Mäthger, R. T. Hanlon, P. B. Dennis, R. R. Naik, E. Forsythe and J. Heikenfeld, Biological *vs.* Electronic Adaptive Coloration: How Can One Inform the Other?, *J. R. Soc., Interface*, **2013**, *10*, 20120601.
2. L. M. Mäthger, E. J. Denton, N. J. Marshall and R. T. Hanlon, Mechanisms and Behavioural Functions of Structural Coloration in Cephalopods, *J. R. Soc., Interface*, **2009**, *6*, S149–S163.
3. R. T. Hanlon and J. B. Messenger, *Cephalopod Behaviour*, Cambridge University Press, Cambridge, 1998.
4. R. T. Hanlon, C.-C. C. Chiao, L. M. Mäthger, K. C. Buresch, A. Barbosa, J. J. Allen, L. Siemann and C. Chubb, Rapid Adaptive Camouflage in Cephalopods, in *Animal Camouflage: Mechanisms and Function*, ed. M. Stevens and S. Merialaita, Cambridge University Press, Cambridge, 2011, ch. 4, pp. 145–163.
5. R. T. Hanlon, Cephalopod Dynamic Camouflage, *Curr. Biol.*, **2007**, *17*, R400–R404.

6. G. R. R. Bell, A. M. Kuzirian, S. L. Senft, L. M. Mäthger, T. J. Wardill and R. T. Hanlon, Chromatophore Radial Muscle Fibers Anchor in Flexible Squid Skin, *Invertebr. Biol.*, **2013**, *132*, 120–132.
7. G. Lanzani, *Nat. Mater.* **2014**, *13*, 775–776.
8. G. G. Malliaras, *Biochim. Biophys. Acta* **2013**, *1830*, 4286–4287.
9. K. Svennersten, K. C. Larsson, M. Berggren, A. Richter-Dahlfors, *Biochim. Biophys. Acta* **2011,** *1810*, 276–285.
10. V. F. Petrenko N. Maeno, *J. Phys. Colloq.* **1987**, *48*, C1-115–C1-119.
11. Z. G. Chiragwandi, O. Nur, M. Willander, N. Calander, *Appl. Phys. Lett.* **2003**, *83*, 5310–5312.
12. R. Fan, S. Huh, R. Yan, J. Arnold, P. Yang, *Nat. Mater.* **2008,** *7*, 303–307.
13. C. Zhong, Y. Deng, A. F. Roudsari, A. Kapetanovic, M. P. Anantram, M. Rolandi, *Nat. Commun.* **2011**, *2*, 476.
14. Y. Deng, E. Josberger, J. Jin, A. F. Rousdari, B. A. Helms, C. Zhong, M. P. Anantram, M. Rolandi, *Sci. Rep.* **2013**, *3*, 2481.
15. A. M. Deml, A. L. Bunge, M. A. Reznikov, A. Kolessov, R. P. O'Hayre, *J. Appl. Phys.* **2012**, *111*, 074511.
16. W. J. Crookes, L.-L. Ding, Q. L. Huang, J. R. Kimbell, J. Horwitz, M. J. McFall-Ngai, *Science* **2004**, *303*, 235–238.
17. R. M. Kramer, W. J. Crookes-Goodson, R. R. Naik, *Nat. Mater.* **2007**, *6*, 533–538.
18. A. R. Tao, D. G. DeMartini, M. Izumi, A. M. Sweeney, A. L. Holt, D. E. Morse, *Biomaterials* **2010**, *31*, 793–801.

19. M. Izumi, A. M. Sweeney, D. DeMartini, J. C. Weaver, M. L. Powers, A. Tao, T. V. Silvas, R. M. Kramer, W. J. Crookes-Goodson, L. M. Mäthger, R. R. Naik, R. T. Hanlon, D. E. Morse, *J. R. Soc. Interface* **2010**, *7*, 549–560.
20. L. Phan, W. G. WalkupIV, D. D. Ordinario, E. Karshalev, J.-M. Jocson, A. M. Burke, A. A. Gorodetsky, *Adv. Mater.* **2013**, *25*, 5621–5625.
21. D. D. Ordinario, L. Phan, W. G. Walkup IV, J. M. Jocson, E. Karshalev, N. Hüsken, and A. A. Gorodetsky, *Nat. Chem.* **2014**, *6*, 596–602.
22. S. Cukierman, *Biochim. Biophys. Acta, Bioenerg.* **2006**, *1757*, 876–885.
23. E. Stavrinidou, P. Leleux, H. Rajaona, D. Khodagholy, J. Rivnay, M. Lindau, S. Sanaur, G. G. Malliaras, *Adv. Mater.* **2013**, *25*, 4488–4493.
24. I. Kymissis, in *Organic Field Effect Transistors: Theory, Fabrication and Characterization, Integrated Circuits and Systems*, Springer, New York, **2009**.
25. A. Lipson, S. G. Lipson, H. Lipson, Optical Physics, 4th ed., Cambridge University Press, Cambridge, 2010.
26. http://hyperphysics.phy-astr.gsu.edu/hbase/phyopt/oilfilm.html#c1

CHAPTER 4 Protochromic Devices from Reflectin

4.1: Abstract

Cephalopods possess remarkable camouflage capabilities, which are enabled by their complex innervated skin architectures and advanced controlling nervous systems. As such, cephalopod skin constitutes an exciting source of inspiration for biomimetic camouflage technologies. Herein, we emulate aspects of optically-active ultrastructures found in squid skin cells and design color-changing bioelectronic devices, which consist of a proton-transporting active layer contacted by a proton-conducting actuating electrode. We observe and quantify distinct shifts in the reflectance and coloration of our devices, which we attribute to changes in thickness induced by the direct electrical injection/extraction of protons. Our findings may hold relevance for developing novel color-changing technologies, understanding ion-transporting biological systems, and engineering improved bioelectronic platforms.

4.2: Introduction

Cephalopods, such as the squid *Doryteuthis (Loligo) pealeii*, have captured the imaginations of scientists and the general public due to their advanced vertebrate-like neurophysiology and unrivaled ability to blend into nearly any environment.[1-6] These animals' camouflage capabilities are enabled by a sophisticated skin structure, wherein multiple different cell types (leucophores, chromatophores, and/or iridophores) perform distinct optical functions but work in concert to control the skin's overall appearance.[4,5] For example, the skin of *D. pealeii* contains iridophores, which modulate the reflection of light, and chromatophores, which modulate the transmission of light.[7-9] Interestingly, both of these cell types are hierarchically controlled by

a network of nerve fibers, which directly interfaces the cells with the central nervous system.[10,11] This sophisticated architecture enables longfin inshore squid skin to effectively serve as a bioelectronic display with capabilities that are enviable from the perspective of manmade dynamic camouflage systems.[5] Given such functionality, cephalopod skin in general has emerged as a tremendous source of inspiration for camouflage devices from both artificial and naturally-occurring materials.[12-17]

As targets for replication in bioelectronic camouflage devices, cephalopod iridophores are particularly interesting because their ultrastructure facilitates the transduction of chemical signals

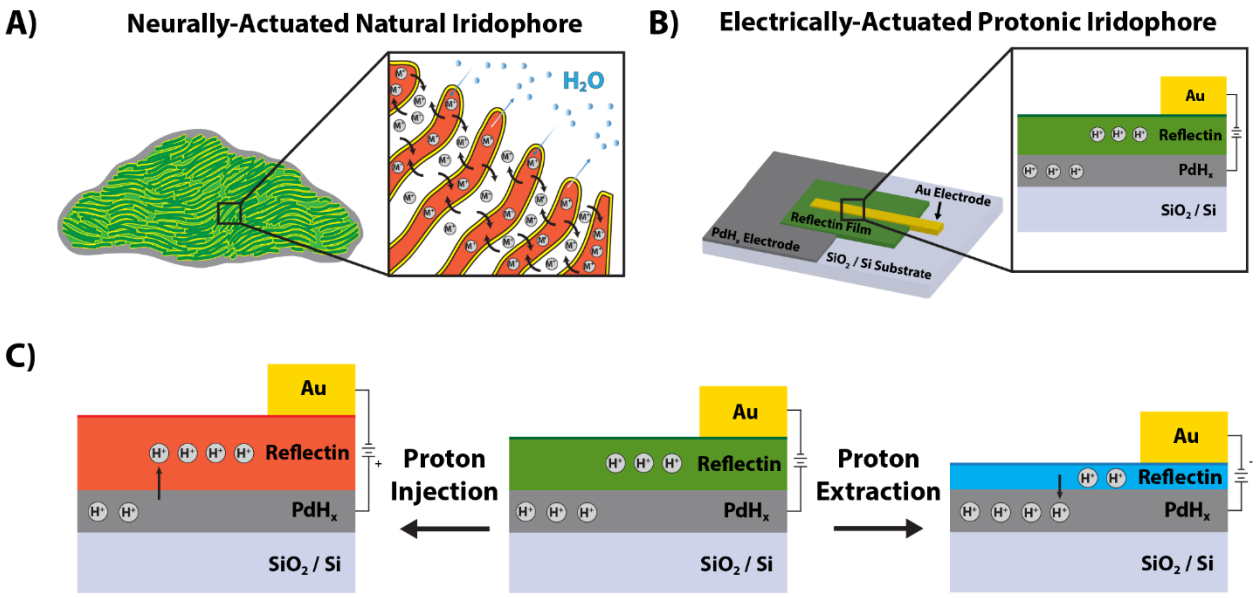

Figure 4.1: A) A simplified, general schematic of a neurally-activated natural iridophore. The color of the iridophore is determined by its constituent Bragg reflector-like structures, which consist of alternating membrane-enclosed reflectin platelets and deep invaginations into the cellular interior. B) A simplified, general schematic of an electrically-actuated protonic iridophore. This protonic device consists of a proton-injecting PdH_x actuation electrode (in analogy to an ion-permeable membrane), a proton-conducting RfA1 active layer (in analogy to a single iridophore platelet) and an ion-blocking Au electrode (as a stable reference). C) A schematic of the effect of direct proton injection and extraction on the thickness and reflectance of a device-integrated RfA1 active layer (center). The injection of protons leads to an increase in thickness and a red shift in reflectance for the RfA1 layer (left), while the extraction of protons leads to a decrease in thickness and a blue shift in reflectance for the RfA1 layer (right).

into mechanical and optical effects.[18,19] To illustrate this point, a schematic of a squid iridophore is shown in Figure 4.1A. The cell's plasma membrane folds into a periodic arrangement, wherein membrane-enclosed platelets from proteins called reflectins alternate with deep invaginations into the cellular interior.[18-30] This structure effectively constitutes a biological Bragg reflector comprised of layers from high and low refractive index materials.[18,19] The reflector is activated via a neurally-controlled signaling cascade that leads to phosphorylation and then condensation of the reflectin proteins (Figure 4.1A).[18,19] The accompanying flux of ions across the cell membrane and subsequent expulsion of water into the invaginations change the size, spacing, and refractive index of the platelets, modulating the reflector's optical properties (Figure 4.1A).[18,19] This rapid and fully reversible process affords exquisite control over the wavelength of light reflected by the iridophores, allowing the cells to tune their coloration across the entire visible spectrum.[18,19]

Herein, we present a new class of cephalopod-inspired protochromic devices with optical characteristics that are electrically controlled. We first draw inspiration from the ultrastructures of squid iridophores and design device architectures featuring a proton-transporting reflectin A1 (RfA1) active layer contacted by a proton-conducting palladium hydride (PdH_x) actuating electrode. We subsequently fabricate such devices and optically characterize them both without and with applied electrical biases. We observe and quantify distinct shifts in the reflectance and coloration of our devices, which we attribute to changes in thickness induced by the direct electrical injection or extraction of protons. Our findings may hold relevance for developing novel color-changing technologies, understanding ion-transporting biological systems, and engineering improved bioelectronic platforms.

4.3: Results and Discussion

In an initial step towards emulating the iridophores' highly-evolved natural architecture, we rationally designed color-changing bioelectronic devices, such as the one illustrated in Figure 4.1B, which could be actuated by ionic fluxes originating not from a squid's central nervous system but from an external electronic circuit. For our approach, we were conceptually encouraged by 1) prior demonstrations that the neurally-controlled influx/efflux of ions alters the dimensions and optical properties of single iridophore platelets[18] and 2) the report that acetic acid-induced injection of protons into RfA1-based coatings modulates their thickness and reflectance *in vitro*.[16] Furthermore, our device design leveraged recent advances in bioprotonics, wherein PdH_x electrodes exchange protons with cephalopod-derived proton conductors, such as maleic chitosan and RfA1 (note that the chemical injection of protons via acid vapor, while highly effective, is impractical for interfacing with external electronics).[26-29,31,32,35-38] Thus, in lieu of a single protein-based platelet, our device incorporated a thin film of RfA1 as the color-changing active component, and in lieu of a surrounding ion-permeable membrane, our device incorporated a PdH_x electrode as the electrically-conducting actuating component (the ion-blocking gold electrode functioned as a stable reference) (Figure 4.1B). For this device, we expected that applied voltages would induce proton exchange between the PdH_x electrode and the RfA1 active layer, thereby leading to protonation/deprotonation of RfA1's amino acids (note that RfA1 possesses a pI of ~ 9)[19,23-25] and likely altering electrostatic interactions within the film's interior. Specifically, under a positive applied voltage, the injection of protons would increase the net positive charge and swell the film, leading to a red-shift in reflectance, and under a negative applied voltage, the extraction of protons

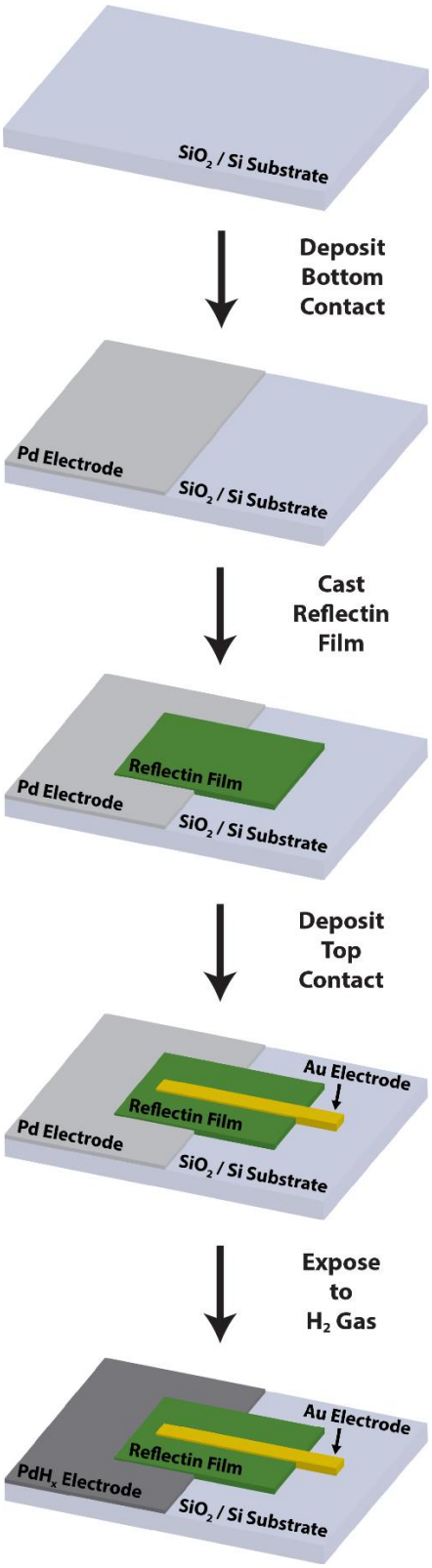

Figure 4.2: The general fabrication scheme for a protochromic device with a PdH_x/RfA1/Au architecture. The strategy consists of the deposition of a Pd bottom contact, the casting of an RfA1 film, the deposition of an Au top contact, and exposure to H_2 gas.

would decrease the positive charge and condense the film, leading to a blue-shift in reflectance (Figure 4.1C). The resulting stimuli-responsive protochromic devices would effectively constitute highly simplified protonic iridophores, with optical functionality roughly analogous to that of the natural system.

We began our experiments by fabricating the desired color-changing bioelectronic devices according to the scheme in Figure 4.2 (see the experimental section for additional details). In our approach, we adapted protocols previously validated for the fabrication of RfA1-based protonic devices.[26-29] First, as the bottom electrode, we deposited a chromium (Cr) adhesion layer followed by a palladium (Pd) layer onto a silicon dioxide/silicon (SiO_2/Si) substrate via electron-beam evaporation. Next, as the active layer, we cast a film of RfA1 onto a portion of the Pd-modified surface, scribing away excess material when necessary. In turn, as the top electrode, we deposited an Au layer directly onto the Pd- and RfA1-modified surface, again via electron-beam evaporation (note that a layered, low-temperature deposition strategy mitigated damage to the protein film, yielding pristine devices like the one shown in Figure 4.3). Finally, for the electrical measurements, we converted the electron-injecting Pd contacts to proton-injecting PdH_x contacts through exposure to hydrogen gas in situ.[26-29,31,32,36-38] The overall procedure furnished devices with a sandwich-type PdH_x/RfA1/Au architecture.

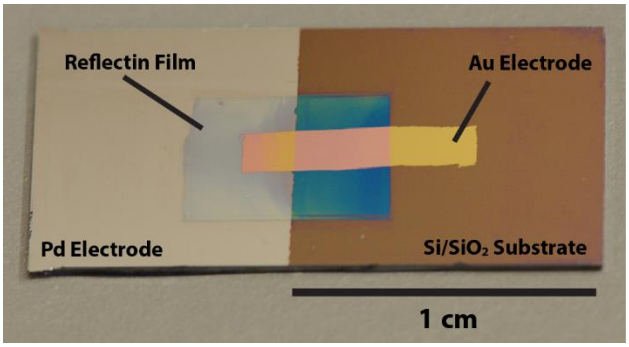

Figure 4.3: A photograph of a representative device, where an RfA1 film is sandwiched between a palladium bottom contact and a gold top contact.

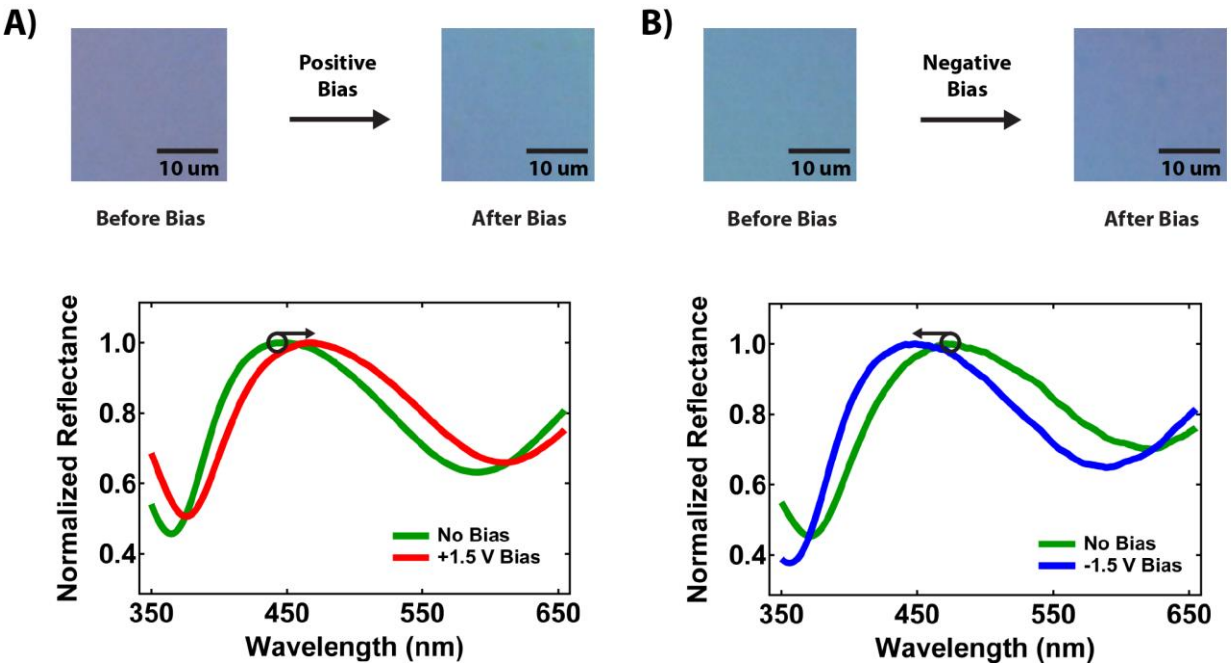

Figure 4.4: A) Top: Optical images of a device-integrated RfA1 film before (left) and after (right) the application of a positive voltage. Note the change in the film color from violet to blue. Bottom: The reflectance spectra for a device-integrated RfA1 film before (green curve) and after (red curve) the application of a positive voltage, demonstrating a red-shift. B) Top: Optical images of a device-integrated RfA1 film before (left) and after (right) the application of a negative voltage. Note the change in the film color from blue to violet. Bottom: The reflectance spectra for a device-integrated RfA1 film before (green curve) and after (blue curve) the application of a negative voltage, demonstrating a blue-shift.

With the desired devices in hand, we first evaluated the optical properties of their constituent RfA1 films without actuation. The optical microscopy images and corresponding reflectance spectra for two hydrated RfA1 films are shown in Figure 4.4A and Figure 4.4B in the absence of an applied voltage (green traces). From the reflectance spectras' peak wavelengths of 448 nm and 471 nm, we calculated expected hydrated thicknesses of 303 nm for the film in Figure 4.4A and 319 nm for the film in Figure 4.4B (see the experimental section for Calculation Details). In turn, we used atomic force microscopy (AFM) to measure the dry thicknesses of the two films and obtained values of 201 nm and 248 nm, which corresponded to approximate hydrated thicknesses of 281 nm for the film in Figure 4.4A and 347 nm for the film in Figure 4.4B (when accounting for swelling). Based on the agreement between the calculated and measured

thicknesses, we inferred that the reflectance and coloration of our device-integrated RfA1 films were dictated largely by thin film interference, in agreement with previous reports for reflectin-based coatings in vitro.[16,17]

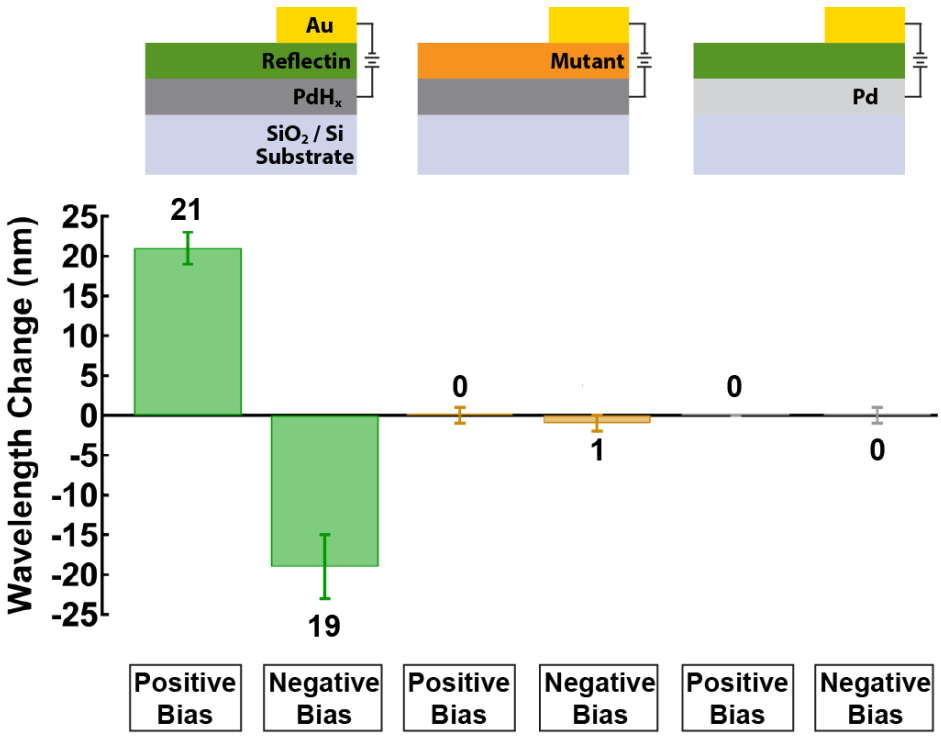

Figure 4.5: The average change in the peak reflectance wavelength for devices with PdH_x/RfA1/Au (left), PdH_x/m-RfA1/Au (middle), and Pd/RfA1/Au (right) architectures under both negative and positive applied biases. The error bars correspond to the standard deviations obtained for a minimum of 5 measurements.

We proceeded to investigate the effect of electrical actuation on the reflectance and coloration of our device-integrated RfA1 films. After application of a positive voltage for a representative film, we observed a distinct change in film coloration from violet to blue and an accompanying ~ 19 nm red shift in the peak reflectance (Figure 4.4A); note that the measurements were readily reproducible, as evidenced by an average shift of ~ 21 ± (2) nm across 7 independent devices (Figure 4.5). Assuming no substantial change in the refractive index, we estimated that the thickness of the device-integrated film in Figure 4.4A increased by 12 nm from 303 nm to 315 nm. In contrast, after application of a negative voltage for a representative film, we observed a distinct

change in the film coloration from blue to violet and an accompanying ~ 23 nm blue shift in the peak reflectance (Figure 4.4B); note that the measurements were again readily reproducible, as evidenced by an average shift of ~ 19 ± (4) nm across 7 independent devices (Figure 4.5). Assuming no substantial change in the refractive index, we estimated that the thickness of the device-integrated film in Figure 4.4B decreased by 16 nm from 319 nm to 303 nm. Based on our measurements, we postulated that the observed changes in reflectance and coloration likely resulted from swelling or condensation of the RfA1 layers, as induced by the direct electrical injection (positive voltages) or extraction (negative voltages) of protons, respectively.

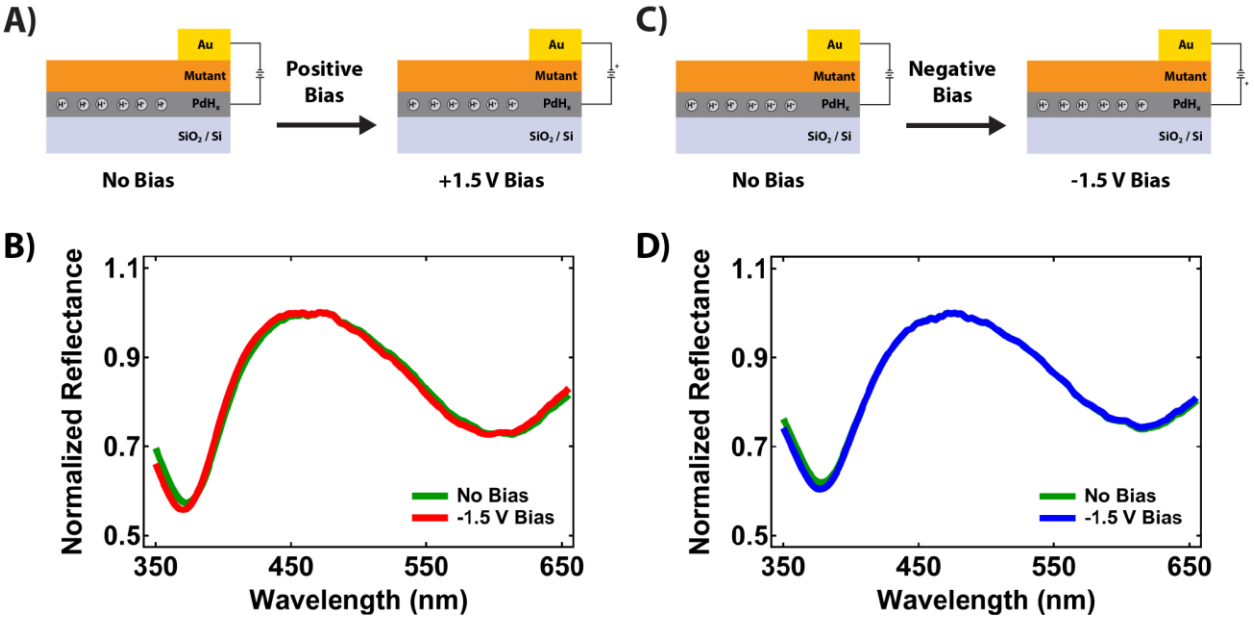

Figure 4.6: A) A schematic of a device with a PdH_x/m-RfA1/Au architecture before and after application of a positive voltage. The active layer is not capable of transporting protons. B) The representative reflectance spectra for a device-integrated m-RfA1 film with palladium hydride and gold contacts before (green curve) and after (red curve) the application of a positive voltage. The spectra are nearly identical. C) A schematic of a device with a PdH_x/m-RfA1/Au architecture before and after application of a negative voltage. The active layer is not capable of transporting protons. D) The representative reflectance spectra for a device-integrated m-RfA1 film with palladium hydride and gold contacts before (green curve) and after (blue curve) the application of a negative voltage. The spectra are nearly identical.

In an initial key control experiment, we verified the importance of the proton-transporting RfA1 active layer for the functionality of our devices. For this purpose, we used a mutant RfA1

variant (m-RfA1) for which the proton-donating aspartic acid and glutamic acid residues were substituted with alanines, making the mutant a far less effective proton conductor than wild-type RfA1.[26] Thus, we fabricated and tested analogues of our devices with a PdH_x/m-RfA1/Au architecture, for which the reflectance spectra both without and with applied voltages are shown in Figure 4.6. Regardless of the voltage, we found only negligible changes in the films' reflectance, with a red shift of 0 ± (1) nm in the peak wavelength across 5 devices for positive voltages and a blue shift of 1 ± (1) nm in the peak wavelength across 5 devices for negative voltages (Figure 4.5). These measurements indicated that the effective transport of protons through the active layer was necessary for the observed shifts in reflectance and coloration.

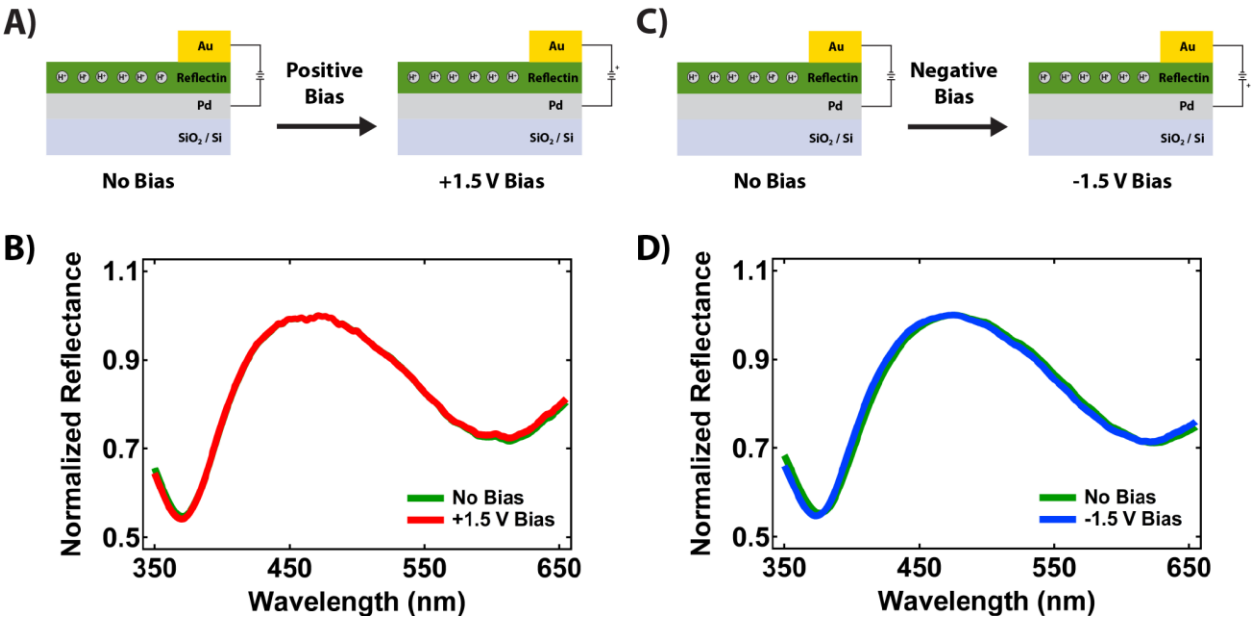

Figure 4.7: A) A schematic of a device with a Pd/RfA1/Au architecture before and after application of a positive voltage. The electrode is not capable of injecting protons into the device. B) The representative reflectance spectra for a device-integrated RfA1 film with palladium and gold contacts before (green curve) and after (red curve) the application of a positive voltage. The spectra are nearly identical. C) A schematic of a device with a Pd/RfA1/Au architecture before and after application of a negative voltage. The electrode is not capable of injecting protons into the device. D) The representative reflectance spectra for a device-integrated RfA1 film with palladium and gold contacts before (green curve) and after (blue curve) the application of a negative voltage. The spectra are nearly identical.

In another key control experiment, we verified the importance of proton injection/extraction for the functionality of our devices. For this purpose, we used Pd electrodes

that had not been exposed to hydrogen gas, making them incapable of proton exchange as electrical contacts.[27,36] Thus, we fabricated and tested analogues of our devices with a Pd/RfA1/Au architecture, for which the reflectance spectra both without and with applied voltages are shown in Figure 4.7. Regardless of the voltage, we again found no change in the films' reflectance spectra, with a red shift of 0 ± (0) nm in the peak wavelength across 5 devices for positive voltages and a blue shift of 0 ± (1) nm in the peak wavelength across 5 devices for negative voltages (Figure 4.5). These measurements confirmed that the effective exchange of protons between the electrodes and active layer was required for the observed shifts in reflectance and coloration.

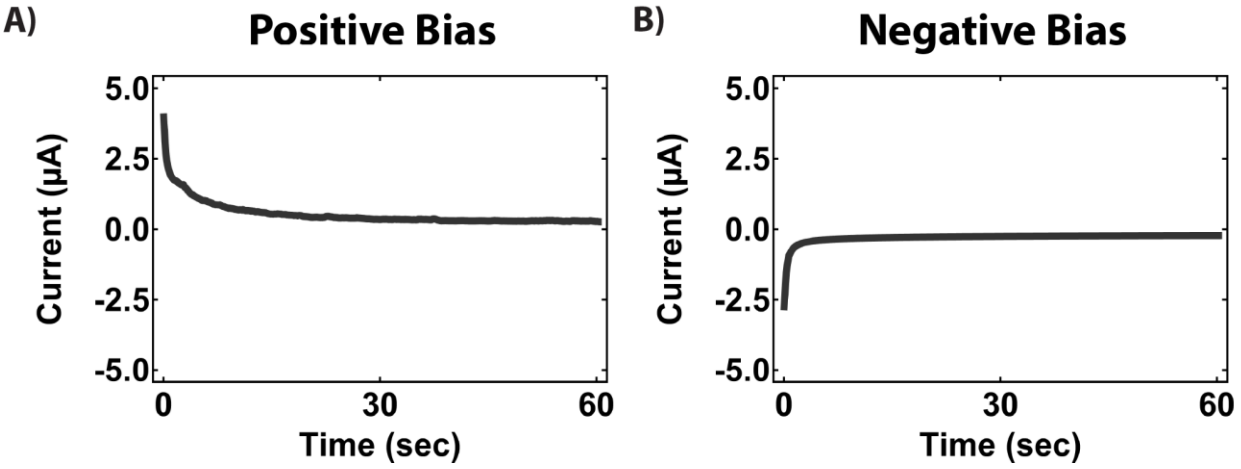

Figure 4.8: Temporal evolution of the current vs. voltage characteristics recorded for a device with a PdH_x/RfA1/Au architecture under A) a positive and B) a negative applied voltage.

Finally, we directly quantified the proton flux that accompanied the changes in the reflectance and coloration of the device-integrated RfA1 films. As examples, the current (I) versus time (t) curves recorded for PdH_x/RfA1/Au devices upon electrical actuation are shown in Figure 4.8. After the application of a positive voltage, we observed a time-dependent evolution of the current, with the initial spike due to a rapid interfacial influx of protons into the RfA1 layer from the PdH_x electrode and the eventual decay likely due to quasi-steady-state diffusional proton transport (Figure 4.8). From integration of the spike in the I-t curves, we calculated that the total

injected charge carrier density was n_{H+} = 13.9 ± 1 x 10^{17} protons/cm^3 across 5 devices (see the experimental section for calculation details).[31,32] In analogous fashion, after the application of a negative voltage, we again observed a time-dependent evolution of the current, with the initial spike due to a rapid interfacial efflux of protons from the RfA1 layer into the PdH_x electrode and the eventual plateau likely due to slow quasi-steady-state diffusional proton transport (Figure 4.8). From integration of the spike in the I-t curves, we calculated that the total extracted charge carrier density was n_{H+} = 8.6 ± 1 x 10^{17} protons/cm^3 across 4 devices (see the experimental section for Calculation Details).[31,32] Interestingly, the extracted proton concentration was similar, albeit not identical, to the values of n_{H+} = ~ 1 – 3 x 10^{17} protons/cm^3 previously obtained from the I-V characteristics of RfA1-based protonic transistors (note that the difference between the values likely arose from the distinct device configurations and interrogation strategies).[26-28] Altogether, our analysis further corroborated the notion that proton exchange between the PdH_x electrode and RfA1 active layers directly accounted for the observed shifts in reflectance and coloration.

4.4: Conclusion

In summary, we have rationally designed and characterized highly simplified protonic iridophores, for which the optical properties are modulated via an electrically-induced influx/efflux of protons, and our observations hold significance for several reasons. First, our measurements represent the only demonstration of the direct electrical triggering of reflectance and coloration changes for individual reflectin films. Given that reflectin-based coatings have been previously actuated through mechanical and chemical means, the reported results highlight the reflectins' potential as adaptive optical materials and represent an initial step towards multi-layer camouflage devices that respond to multiple exogenous stimuli. Second, our measurements lend

additional support (albeit indirectly and within an in vitro context) for the mechanism proposed to explain iridophore activation within squid skin, wherein the trans-membrane flux of ions plays a prominent role. Through the use of electrodes that inject/extract other cations, the described strategy could prove valuable for understanding how distinct charged species affect the condensation behavior and optical properties of reflectin platelets. Third, our experiments suggest that reflectin-based devices are well positioned for the sensitive spectroelectrochemical monitoring of ion (proton) fluxes, at both the local and global levels. Due to the intrinsic biocompatibility of reflectin, the described strategy may thus afford new opportunities for the interrogation of ion signaling pathways in device-interfaced living cells or ion-transporting biomolecules. Finally, our simplified devices effectively constitute model organic-inorganic interfaces, which facilitate the direct monitoring of proton injection/extraction. The overall approach may be suitable for the study of interfacial ion transport, as relevant for the operating mechanism of various bioelectronic platforms. Altogether, our observations may hold relevance for designing advanced bioinspired camouflage technologies, understanding the function of ion-transporting biological systems, and engineering improved bioelectronic devices.

4.5 Supplementary Information

Production of Wild-Type and Mutant Reflectins: Wild-type reflectin A1 and mutant reflectin A1 (in which the aspartic acid and glutamic acid residues were substituted with alanines) were expressed, purified, and characterized according to a general established protocol.[26-28] In brief, the pJExpress414 expression vectors containing either the wild type or mutant reflectin were transformed into BL21(DE3) cells (Novagen). The reflectins were expressed at 37 °C using Overnight Express Instant Terrific Broth (TB) media (Novagen) supplemented with 100 μg mL^{-1}

Carbenicillin. The reflectins were completely insoluble when expressed at 37 °C and were sequestered in inclusion bodies prepared using Novagen BugBuster® according to the manufacturer's suggested protocol. The inclusion bodies were then solubilized in denaturing buffer (pH 7.4, 50 mM Sodium Phosphate, 300 mM NaCl, 6M guanidine hydrochloride) and purified under denaturing conditions on HisPur Cobalt Resin (Thermo Scientific) immobilized metal affinity chromatography (IMAC) gravity columns according to the manufacturer's protocols. The protein was eluted by using denaturing buffer supplemented with 250 mM imidazole. The fractions containing reflectin were pooled and concentrated on Millipore Amicon Concentrators before further purification with high-performance liquid chromatography (HPLC) on an Agilent 1260 Infinity system using an Agilent reverse phase C18 column with a gradient evolved from 95% Buffer A:5% Buffer B to 5% Buffer A:95% Buffer B at a flow rate of 1 mL min^{-1} over 30 minutes (Buffer A: 99.9% H_2O, 0.1% TFA; Buffer B: 95% acetonitrile, 4.9% H_2O, 0.1% TFA). The pure reflectin fractions were pooled, flash frozen in liquid nitrogen, and lyophilized. The identity of the purified proteins was confirmed by in-gel tryptic digestion and tandem mass spectrometry on a Thermo Orbitrap instrument outfitted with an electrospray ionization source. The protein concentrations and yields were quantified via the Bradford protein assay with bovine serum albumin (BSA) as a standard (BioRad).

Fabrication of Reflectin-Based Devices: The two-terminal devices were fabricated in a sandwich configuration by drawing upon preciously-reported procedures.[26-28] In brief, SiO_2/Si substrates (International Wafer Service, Inc.) were first cleaned in Piranha solution (1:3 hydrogen peroxide to sulfuric acid) and washed thoroughly. Subsequently, contacts consisting of a 4 nm chromium adhesion layer overlaid with a 40 nm palladium layer were electron-beam evaporated using a

Temescal FC-2000 Bell Jar Deposition System onto the clean substrates through a shadow mask. Next, a film of either wild-type RfA1 or mutant RfA1 was coated evenly between the palladium contact and the substrate surface. Subsequently, a 40 nm gold contact was deposited over the substrate surface and the RfA1 film, partially overlapping areas where the RfA1 film contacted the palladium contact. To prevent degradation of the RfA1 film during, the gold top contact was deposited via a layered strategy, i.e. 1 nm, 2 nm, 3 nm, 4 nm, and 5 nm layers of gold were first deposited sequentially, followed by 25 nm of gold in 5 nm increments. To further mitigate the possibility of film degradation, the film was allowed to cool for 5 minutes after the deposition of each layer, and the temperature of the evaporation chamber was kept below 30° C at all times. Finally, to form proton-injecting PdH_x electrodes the devices were exposed to a 5% hydrogen/95% argon atmosphere in situ.

Physical Characterization of Reflectin-based Devices: The thicknesses of the RfA1 films were determined from the analysis of topographical scans obtained with an Asylum Research MFP-3D Atomic Force microscope. The AFM data was analyzed with the Gwyddion software package. The topological scans were rastered at 0.50 Hz and normalized using polynomial subtraction for improved image quality.

Imaging of Reflectin-Based Devices: The devices were imaged with a D800 camera (Nikon) equipped with a 105 mm f/2.8 AF-S Micro-Nikkor (Nikon). The images were captured with an exposure time of 1/25 second, aperture setting of f/11, and ISO of 1600.

Spectroscopic Characterization of Reflectin-Based Devices: The device-integrated RfA1 films were characterized with optical microscopy and reflectance measurements both with and without applied voltages (see below). The optical images were obtained with a Craic Technologies 20/20 PV™ UV-visible-NIR Microspectrophotometer (outfitted with a Zeiss Ultrafluar 10X lens, NA = 0.2) and processed with the manufacturer's ImageUV software. The reflectance spectra were measured both with and without applied voltages with a Craic Technologies 20/20 PV™ UV-visible-NIR Microspectrophotometer outfitted with a tungsten halogen white light source (effective wavelength range of λ = 350 nm to λ = 1700 nm). During the measurements, the devices were housed in a custom built enclosure, which maintained the relative humidity at 90 %. The reflectance data were acquired normal to the substrate surface and were referenced to a Thorlabs 25.4 mm Protected Aluminum Mirror (unless otherwise noted).

Electrical Characterization of Reflectin-based Devices: The devices were characterized by using a 2400 Series SourceMeter Source Measure Unit (SMU) (Keithley Instruments). For the electrical measurements, the current as a function of time was recorded after application of either negative voltages of -1.5 V or positive voltages of +1.5 V. During the measurements, the devices were housed in a custom built enclosure, which maintained the relative humidity at 90 %.

Analysis of the Current-Voltage Data: The charge extracted from or injected into the RfA1 films was calculated from the initial current spike according to the methods of Rolandi and co-workers[31,32] by using the following equation:

$$Q = \int_{t=0}^{t=t_{spike}} I_o dt \quad (1)$$

where Q is the total amount of charge in Coulombs, t_{spike} is the time in seconds, and I_o is the measured current in Amps. The total charge Q was in turn converted to the total proton concentration per unit volume (protons cm^{-3}).

Estimation of Reflectin Film Thickness: The thicknesses of the RfA1 films were estimated by using thin-film interference theory.[33] First, we calculated the refractive index of hydrated RfA1 films according to the method of Sackmann and co-workers[34] by using the following equation:

$$n_F = n_M \sqrt{1 + \frac{3\frac{h_o}{h}}{\left(\frac{n_o^2 + 2n_M^2}{n_o^2 - n_M^2}\right) - \frac{h_o}{h}}} \quad (2)$$

where n_F is the refractive index of the hydrated film, n_o is the refractive index of the pure solute, n_M is the refractive index of the pure solvent, h_o is the dry film thickness at low relative humidity, and h is the layer thickness at increased relative humidity. Next, we calculated the film thicknesses by using the following equation (which reasonably approximates the optical properties of our films at near-normal incidence):

$$2 \cdot n_F \cdot d = m \cdot \lambda \quad (3)$$

where d is the thickness, n_F is the refractive index, m is an integer, and λ is the peak wavelength.

4.6: Acknowledgements

This chapter is an adaptation of the material as it appears in the manuscript draft submitted to Advanced Optical Materials. The co-authors listed in this publication directed and supervised research which forms the basis for the material in the chapter. Author Contributions: D. D. O., P. E. S., and A. A. G. conceptualized and designed the experiments; D. D. O., E. M. L., and L. P.

performed the research; M. N., J. P. L., and M. J. A. helped prepare material for experiments, D. D. O. and A. A. G. analyzed the data; and D. D. O., P. E. S., and A. A. G. wrote the paper.

4.7: References

1. N. J. Abbott, R. Williamson, L. Maddock, in *Cephalopod Neurobiology: Neuroscience Studies in Squid, Octopus, and Cuttlefish*, Oxford University Press, Oxford, **1995**.
2. R. T. Hanlon, J. B. Messenger, in *Cephalopod Behaviour*, Cambridge University Press, United Kingdom, **1998**.
3. G. Kaufman, C. Orlt, *Kings of Camouflage*, Producers. "Cuttlefish: The Brainy Bunch" [Television Broadcast], Public Broadcasting Service (PBS), **2011**.
4. L. M. Mäthger, E. J. Denton, N. J. Marshall, R. T. Hanlon, *J. R. Soc. Interface* **2009**, *6*, 149.
5. E. Kreit, L. M. Mäthger, R. T. Hanlon, P. B. Dennis, R. R. Naik, E. Forsythe, J. Heikenfeld, *J. R. Soc. Interface* **2013**, *10*, 20120601.
6. L. Phan, R. Kautz, E. M. Leung, K. L. Naughton, Y. Van Dyke, A. A. Gorodetsky, *Chem. Mater.* Accepted.
7. R. T. Hanlon, *Malacologia* **1982**, *23*, 89.
8. L. M. Mäthger, R. T, Hanlon, *Cell Tissue Res.* **2007**, *329*, 179.
9. R. A. Cloney, S. L. Brocco, *Am. Zool.* **1983**, *23*, 581–592.
10. J. B. Messenger, *Biol. Rev. Cambridge Philos Soc.* **2001**, *76*, 473.
11. T. J. Wardill, P. T. Gonzalez-Bellido, R. J. Crook, R. T. Hanlon, *Proc. R. Soc. B* **2012**, *279*, 4243.

12. C. Yu, Y. Li, X. Zhang, X. Huang, V. Malyarchuk, S. Wang, Y. Shi, L. Gao, Y. Su, Y. Zhang, H. Xu, R. T. Hanlon, Y. Huang, J. A. Rogers, *Proc. Natl. Acad. Sci. U. S. A.* **2014**, 111, 12998.
13. S. Zheng, D. Zhang, W. Huang, Z. Wang, S. G. Freire, X. Yu, A. T. Smith, E. Y. Huang, H. Nguon, L. Sun, *Nat. Commun.* **2016**, *7*, 11802.
14. Q. Wang, G. R. Gossweiler, S. L. Craig, X. Zhao, *Nat. Commun*. **2014**, *5*, 4899.
15. R. M. Kramer, W. J. Crookes-Goodson, R. R. Naik, *Nat. Mater*. **2007**, *6*, 533.
16. L. Phan, W. G. Walkup IV, D. D. Ordinario, E. Karshalev, J-M. Jocson, A. M. Burke, A. A. Gorodetsky, *Adv. Mater*. **2013**, *25*, 5621.
17. L. Phan, D. D. Ordinario, E. Karshalev, W. G. Walkup IV, M. A. Shenk, A. A. Gorodetsky, *J. Mater. Chem. C* **2015**, *3*, 6493.
18. D. G. DeMartini, D. V. Krogstad, D. E. Morse, *Proc. Natl. Acad. Sci. USA* **2013**, *110*, 2552.
19. D. G. DeMartini, M. Izumi, A. T. Weaver, E. Pandolfi, D. E. Morse, *J. Biol. Chem.* **2015**, *290*, 15238.
20. G. Qin, P. B. Dennis, Y. Zhang, X. Hu, J. E. Bressner, Z. Sun, W. J. Crookes-Goodson, R. R. Naik, F. G. Omenetto, D. L. Kaplan, *J. Polym. Sci., Part B: Polym. Phys.* **2013**, *51*, 254.
21. L. Phan, R. Kautz, J. Arulmoli, I. H. Kim, D. T. T. Le, M. A. Shenk, M. M. Pathak, L. A. Flanagan, F. Tombola, A. A. Gorodetsky, *ACS Appl. Mater. Interfaces* **2016**, *8*, 278.
22. W. J. Crookes, L. L. Ding, Q. L. Huang, J. R. Kimbell, J. Horwitz, M. J. McFall-Ngai, *Science* **2004**, *303*, 235.
23. A. R. Tao, D. G. DeMartini, M. Izumi, A. M. Sweeney, A. L. Holt, D. E. Morse, *Biomaterials* **2010**, *31*, 793.

24. M. Izumi, A. M. Sweeney, D. G. DeMartini, J. C. Weaver, M. L. Powers, A. R. Tao, T. V. Silvas, R. M. Kramer, W. J. Crookes-Goodson, L. M. Mäthger, R. R. Naik, R. T. Hanlon, D. E. Morse, *J. R. Soc. Interface* **2010**, *7*, 549.

25. R. Levenson, C. Bracken, N. Bush, D. E. Morse, *J. Biol. Chem.* **2016**, *291*, 4058.

26. D. D. Ordinario, L. Phan, W. G. Walkup IV, J-M. Jocson, E. Karshalev, N. Hüsken, A. A. Gorodetsky, *Nat. Chem*. **2014**, *6*, 596.

27. D. D. Ordinario, L. Phan, J-M. Jocson, T. Nguyen, A. A. Gorodetsky, *APL Mater*. **2015**, *3*, 014907.

28. D. D. Ordinario, L. Phan, Y. Van Dyke, T. Nguyen, A. G. Smith, M. Nguyen, N. M. Mofid, M. K. Dao, A. A. Gorodetsky, *Chem. Mater.* **2016**, *28*, 3703.

29. D. D. Ordinario, L. Phan, W. G. Walkup IV, Y. Van Dyke, E. M. Leung, M. Nguyen, A. G. Smith, J. Kerr, M. Naeim, I. Kymissis, A. A. Gorodetsky, *RSC Adv.* **2016**, *6*, 57103.

30. K. L. Naughton, L. Phan, E. M. Leung, R. Kautz, Q. Lin, Y. Van Dyke, B. Marmiroli, B. Sartori, A. Arvai, S. Li, M. E. Pique, M. Naeim, J. P. Kerr, M. J. Aquino, V. A. Roberts, E. D. Getzoff, C. Zhu, S. Bernstorff, A. A. Gorodetsky, *Adv. Mater*. **2016,** doi: 10.1002/adma.201601666.

31. E. Josberger, Y. Deng, W. Sun, R. Kautz, M. Rolandi, *Adv. Mater*. **2014**, *26*, 4986.

32. T. Miyake, E. Josberger, S. Keene, Y. Deng, M. Rolandi, *APL Mater.* **2015**, *3*, 014906.

33. A. Lipson, S. G. Lipson, H. Lipson, in *Optical Physics*, 4th ed.; Cambridge University Press: Cambridge, **2010**.

34. G. Mathe, A. Albersdörfer, K. R. Neumaier, E. Sackmann, *Langmuir* **1999**, *15*, 8726.

35. Z. Hemmatian, T. Miyake, Y. Deng, E. Josberger, S. Keene, R. Kautz, C. Zhong, J. Jin, M. Rolandi, *J. Mater. Chem. C* **2015**, *3*, 6407.

36. C. Zhong, Y. Deng, A. F. Roudsari, A. Kapetanovic, M. P. Anantram, M. Rolandi, *Nat. Commun*. **2011**, *2*, 476.

37. Y. Deng, E. Josberger, J. Jin, A. F. Rousdari, B. A. Helms, C. Zhong, M. P. Anantram, M. Rolandi, *Sci. Rep*. **2013**, *3*, 2481.

38. Y. Deng, B. Helms, M. Rolandi, *J. Polym. Sci., Part A: Polym. Chem.* **2015**, *53*, 211.

CHAPTER 5 Reflectin as a Material for Neural Stem Cell Growth

5.1: Abstract

Cephalopods possess remarkable camouflage capabilities, which are enabled by their complex skin structure and sophisticated nervous system. Such unique characteristics have in turn inspired the design of novel functional materials and devices. Within this context, recent studies have focused on investigating the self-assembly, optical, and electrical properties of reflectin, a protein that plays a key role in cephalopod structural coloration. Herein, we report the discovery that reflectin constitutes an effective material for the growth of human neural stem/progenitor cells. Our findings may hold relevance both for understanding cephalopod embryogenesis and for developing improved protein-based bioelectronic devices.

5.2: Introduction

Cephalopods (squid, octopuses, and cuttlefish) are renowned as much for their stunning camouflage displays as for their vertebrate-like behavioral characteristics.[1-6] These abilities stem from the cephalopods' sophisticated nervous system, which has evolved to exhibit a number of anatomical and functional similarities with the nervous systems of vertebrates.[4,6-11] Consequently, cephalopods have facilitated fundamental neurobiology research by furnishing seminal comparative neurophysiological model systems, including giant axons, chemical synapses, and chromatophore neuromuscular junctions.[12-19] The study of cephalopods has therefore illuminated basic mechanisms of neuronal communication and greatly advanced scientific understanding of human brain function.[4,6-11]

Outside of neuroscience, the complex skin structure of cephalopods has served as a source of inspiration for the development of novel functional devices from both artificial[20-25] and natural

materials.[26-29] For example, several groups have fabricated stimuli-responsive optical coatings from proteins known as reflectins, which play a crucial role in cephalopod structural coloration and possess unique self-assembly properties.[26-34] Moreover, the reflectin A1 isoform from *Doryteuthis* (*Loligo*) *pealeii* has been shown to function as an effective proton conduction medium, enabling its use in protonic transistors.[35,36] These findings have indicated that reflectins possess untapped potential as active materials not only for adaptive optics but also for bioelectronic devices.

Recently, cephalopods, and specifically the cuttlefish Sepia officinalis, have been touted as promising comparative models for ecological and evolutionary developmental biology.[37-39] Within this context, the presence of both mRNA and iridescence associated with reflectin were noted during the later stages of embryogenesis in Sepia officinalis.[40,41] Interestingly, reflectin was detected during developmental stages that correlate to some of the major steps of neurogenesis, precisely when brain maturation and growth occurs in Sepia officinalis embryos.[40,41] These observations hinted at undiscovered roles for reflectin in cephalopod neural development and inspired us to consider the possibility that reflectin could promote neural stem cell growth.

Herein, we report the finding that the reflectin A1 isoform constitutes an effective substrate material for human neural stem/progenitor cells (hNSPCs). We first fabricate reflectin films according to standard protocols.[26,27,35,36] We next show that these substrates support the growth of murine and human cells. We subsequently demonstrate that reflectin films facilitate the adhesion, proliferation, and differentiation of relatively difficult-to-culture hNSPCs. Our findings represent a crucial step toward the direct electrical monitoring and triggering of cellular biochemical events with reflectin-based bioelectronic devices.

5.3 Results and Discussion

We began our studies by fabricating reflectin films on quartz or silica substrates. We first expressed a histidine-tagged *Doryteuthis* (*Loligo*) *pealeii* reflectin A1 isoform in *E. coli*. We then coated the substrates with reflectin via a modified doctor blading procedure (Figure 5.1), yielding films that were similar to those reported in our previous studies.[26,27] The resulting reflectin-coated substrates were used directly for cell culture experiments (Figure 5.1).

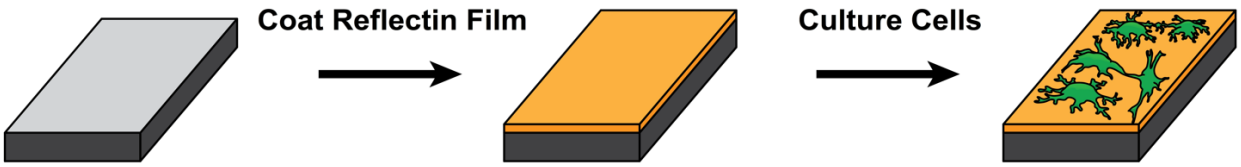

Figure 5.1: General illustration of cell culture experiments on reflectin-coated substrates. Reflectin films were fabricated via a modified doctor blading procedure and then used directly for the growth of mammalian cells.

We initially evaluated the ability of reflectin to support the growth of intrinsically adherent murine and human cells (before transitioning to a more challenging cell type). For these experiments, we specifically selected three established cell lines that are well-known to grow on varied surfaces: HEK293A (human embryonic kidney cells that are widespread in cell biology),[42-44] MDA-MB-231 (human mammary cells that are employed in breast cancer research),[45-47] and BV2 (murine microglial cell lines that are used for exploring the immune response of the central nervous system).[48-50] The use of these established cell lines facilitated our exploratory protocol optimization.

We incubated reflectin-coated substrates with HEK293A, MDA-MB-231, or BV2 cells. After 1 day, we visualized the substrates with bright-field microscopy (Figure 5.2). The three cell types exhibited morphologies that were consistent with literature precedent and indicative of adhesion and/or division. Indeed, HEK293A cells grew together in islands and possessed relatively flat bodies;[42-44] MDA-MB-231 cells featured granular and spindle-like bodies;[45-47] and BV2 cells

varied between flat spinous and small rounded bodies.[48-50] These observations demonstrated that reflectin films were capable of supporting mammalian cell adhesion and portended favorably for the subsequent experiments.

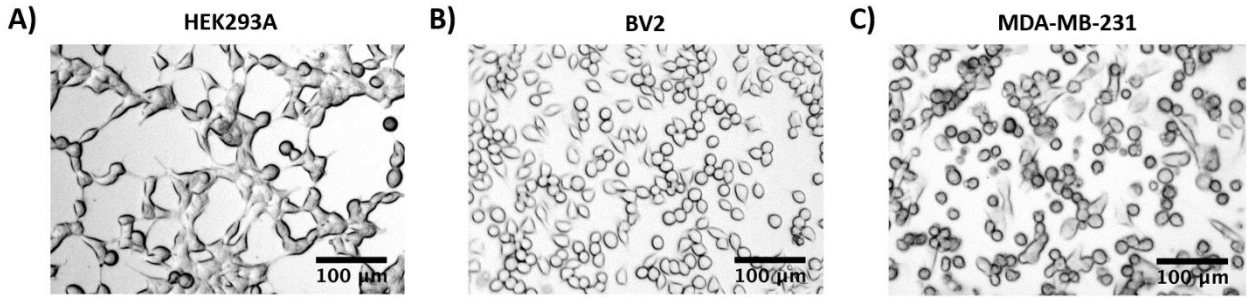

Figure 5.2: Typical bright-field microscopy images of A) HEK293A, B) BV2, and C) MDA-MB-231 cells on reflectin films. The images were collected 1 day after seeding and show that the cells have adhered to the substrates.

We proceeded to challenge our substrates with hNSPCs, which play an essential role in brain and spinal cord development.[51-53] As a general rule, stem cells are exquisitely sensitive to chemical and physical cues from their surrounding environment, making them relatively difficult to culture on arbitrary surfaces.[54-60] Here, we focused our efforts on SC27 hNSPCs derived from the cerebral cortex of a post-mortem fetal brain.[61,62] These cells express standard neural stem cell markers, including SOX2, nestin, and CD 133, and can potentially differentiate into three of the major brain cell types (i.e., astrocytes, neurons, and oligodendrocytes).[61-65] They have also been shown to possess therapeutic potential in mouse models of Sandhoff disease.[66] Furthermore, we have previously explored the adhesion, proliferation, and differentiation of SC27 hNSPCs under varied conditions on different substrates.[63,64,67] Thus, SC27 hNSPCs represented a particularly advantageous choice for our studies.

We seeded reflectin-coated and uncoated substrates with undifferentiated SC27 hNSPCs and visualized them with phase contrast optical microscopy over a period of 15 days (Figure 5.3). For the coated substrates, we were gratified to observe that the hNSPCs were bound to the surface after 1 day. Indeed, most of the cells adopted a predominantly elongated morphology, and some

of the cells displayed a rounded morphology while maintaining attachment to the substrate, as might be expected during cell division (Figure 5.3A). After 15 days, we found a marked >10-fold increase in the cell density, confirming division (Figure 5.3D). In contrast, uncoated substrates showed no hNSPC binding or growth under identical conditions over the same time period (Figure 5.3D). Together, these observations indicated that reflectin coatings facilitated hNSPC attachment and subsequent proliferation on their surfaces (and supported cell viability for an extended period of time).

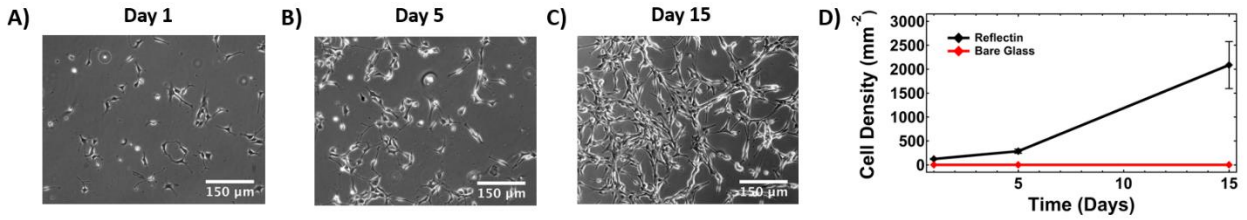

Figure 5.3: Typical phase contrast optical microscopy images of hNSPCs on reflectin films, which demonstrate cell proliferation over time. The images were collected A) 1 day, B) 5 days, and C) 15 days after seeding. D) The plot of the cell density on both reflectin-coated and uncoated substrates after 1 day, 5 days, and 15 days. The error bars indicate the standard error of the mean per film.

We next directly compared hNSPC growth on reflectin and more established materials (Figure 5.4). Due to their significance in both the fetal and adult central nervous systems, hNSPCs have been cultured on various substrates, including ceramics, polymers, polysaccharides, synthetic peptides, and naturally occurring proteins.[54-56] For our comparison, we selected fibronectin, laminin, and poly-d-lysine. These coatings were specifically chosen because they are in the same materials class as reflectin (i.e., proteins and peptides)[54-56] and have been previously used for the growth of hNSPCs.[63,64,67]

Phase contrast optical microscopy images of cells cultured under identical conditions on reflectin, fibronectin, laminin, and poly-d-lysine are shown in Figure 5.4. Here, because stem cells often produce their own extracellular matrices, which contribute to cell adhesion and proliferation over extended periods of time, we limited our analysis to the first 3 days of growth. Although

hNSPCs were not always uniformly distributed on reflectin-coated substrates (Figure 5.4A), the cell morphologies were similar to those observed on fibronectin- and laminin-coated substrates (Figure 5.4B,C) but quite distinct from those observed on poly-d-lysine-coated substrates (Figure 5.4D). Moreover, we observed that the cell densities on reflectin, fibronectin, and laminin were comparable and much higher than on poly-d-lysine (Figure 5.4E). Overall, the performance of reflectin was comparable to that of common validated neural stem cell growth matrices.

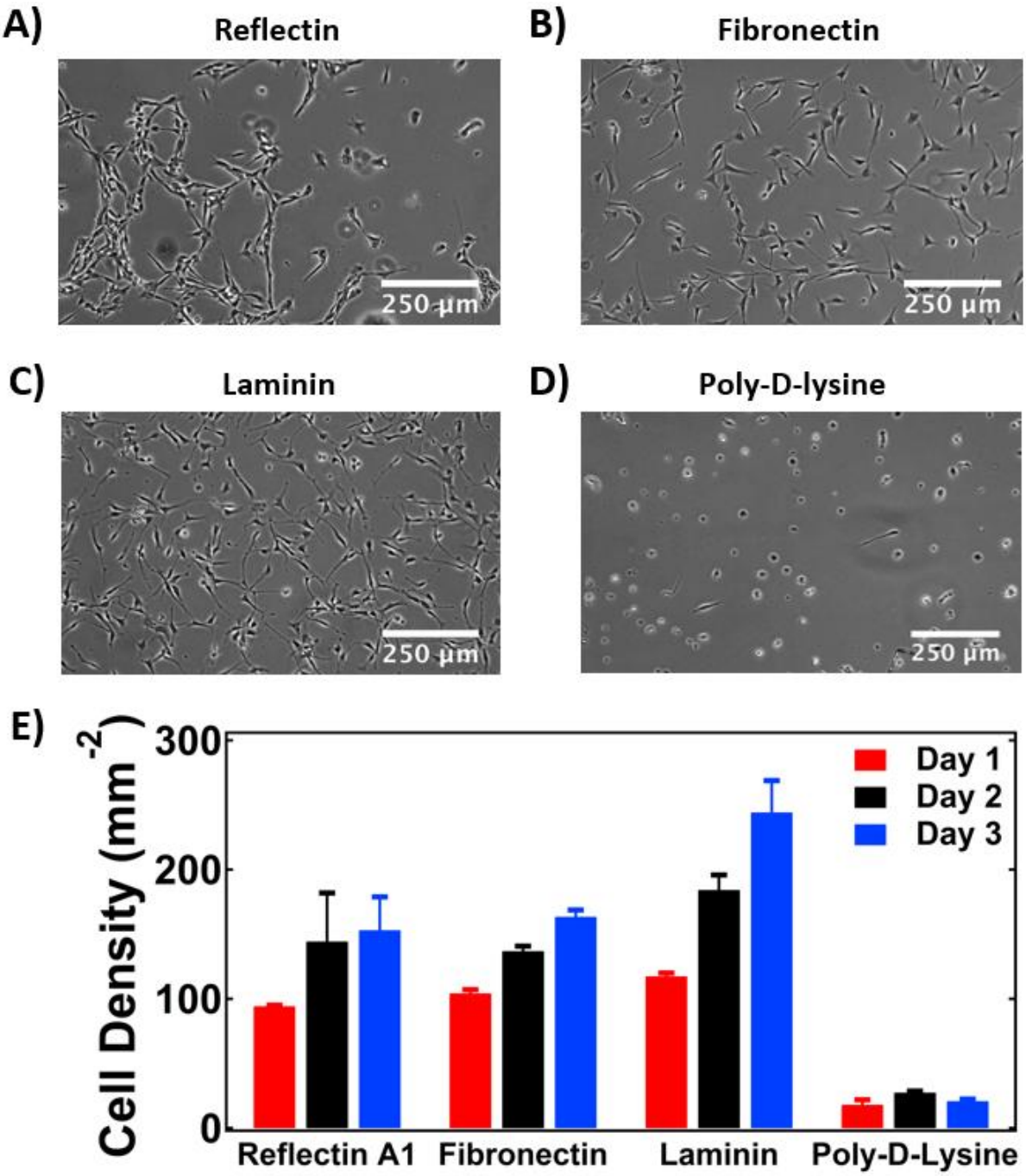

Figure 5.4: Typical phase contrast optical microscopy images of hNSPCs on A) reflectin, B) fibronectin, C) laminin, and D) poly-d-lysine. The cell cultures were prepared under identical conditions, and the images were collected 3 days after seeding. E) The corresponding plot of the cell density for each of the 4 substrates over the initial 3 days after seeding. Note that the cell density on reflectin is comparable to the cell density on fibronectin and laminin. The error bars indicate the standard error of the mean per film.

We proceeded to assess the behavior of hNSPCs cultured on reflectin-coated substrates. Because stem cell/matrix interactions influence cell fate,[54-60] we investigated whether reflectin

affected typical physiological processes previously documented for membrane-bound proteins at the cell–substrate interface. Thus, we studied the activity of the Ca^{2+}-permeable ion channel Piezo1, which influences stem cell differentiation via the transduction of matrix mechanical information.[67] For this purpose, we utilized total internal reflection fluorescence microscopy (TIRFM), a technique that reduces intracellular background fluorescence and specifically reports on events at the cell–substrate interface (Figure 5.5).[68,69] We postulated that reflectin would be especially well suited for TIRFM experiments due to its favorable optical properties, including a high refractive index of 1.54.[26,27]

We visualized hNSPCs on reflectin-coated substrates with TIRFM, monitoring them in real time (Figure 5.5). The fluorescent Ca^{2+} indicator Fluo-4AM facilitated imaging of individual cells (Figure 5.5B), enabling us to measure spontaneous Ca^{2+} transients that have been previously linked to Piezo1 activity.[67] As an example, two arbitrary representative areas are marked with blue and red boxes in Figure 5.5B, and the corresponding spontaneous transients are shown in Figure 5.5C. In general, the appearance of the hNSPCs, as well as the amplitude and frequency of the associated transient, closely resembled those found on fibronectin-coated substrates.[67] Overall, our TIRFM measurements provided additional evidence for hNSPCs exhibiting "typical" behavior and activity on reflectin.

Having validated that reflectin-coated substrates support hNSPC adhesion and proliferation, we investigated the differentiation potential of reflectin-bound neural stem cells. Thus, after 2 days of growth in proliferation media, we induced differentiation of the hNSPCs by substituting proliferation media with differentiation media. After 14 days in the differentiation media, we fixed, immunostained, and imaged the bound hNSPCs via standard protocols.[63,64,67] We

sought to detect the presence of neurons and astrocytes but not oligodendrocytes, as they are not efficiently generated via standard differentiation protocols.

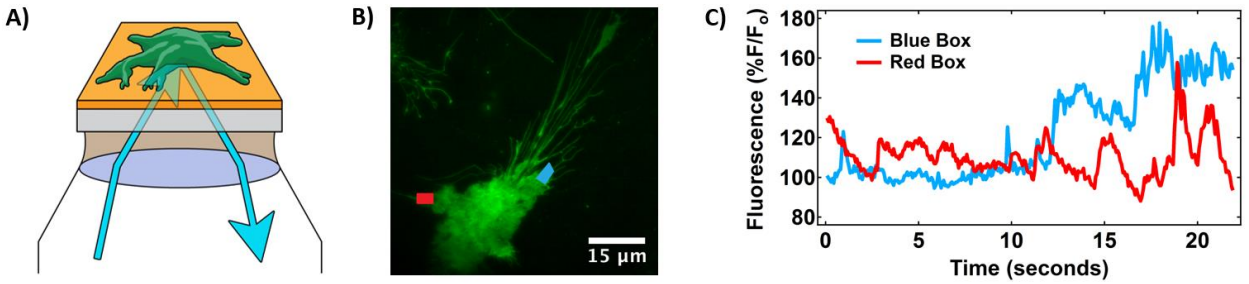

Figure 5.5: A) An illustration of total internal reflection fluorescence microscopy of an hNSPC (green) on a reflectin-coated substrate. The reflectin film is orange, and the reflected light is indicated by a blue arrow. B) A typical total internal reflection fluorescence microscopy image obtained of an hNSPC loaded with the fluorescent Ca^{2+} indicator Fluo-4 AM. Two arbitrary representative areas are marked with blue and red boxes. C) A plot of the fluorescence intensity as a function of time for the blue and red boxes in panel B. The plot shows the presence of spontaneous Ca^{2+} transients, which are associated with Piezo1 channel activity.

Fluorescence microscopy images of two different immunostained sets of hNSPCs are shown in Figure 5.6. To detect astrocytes, we labeled cells for SOX2, a stem/progenitor cell marker (Figure 5.6B), and GFAP, a typical astrocytic marker (Figure 5.6C). This costaining approach identified the SOX2-negative and GFAP-positive cells as fully differentiated astrocytes (Figure 5.6D). To detect neurons, we labeled cells for a combination of MAP2 and DCX, which are common neuronal markers (Figure 5.6F,G). This costaining approach identified the MAP2- and DCX-positive cells as differentiated neurons (Figure 5.6H). Here, we note that immunostained differentiated cells grown on reflectin (Figure 5.6) were almost indistinguishable from those grown on laminin under identical conditions (Figure 5.S1). For example, the percentages of hNSPCs on reflectin that transformed into astrocytes and neurons were 64.2 ± 0.6% and 3.9 ± 0.7%, respectively, and the percentages of hNSPCs on laminin that transformed into astrocytes and neurons were 67.1 ± 6.1% and 4.2 ± 0.8%, respectively. Overall, our experiments confirmed that reflectin-coated substrates were fully capable of supporting neural stem cell differentiation.

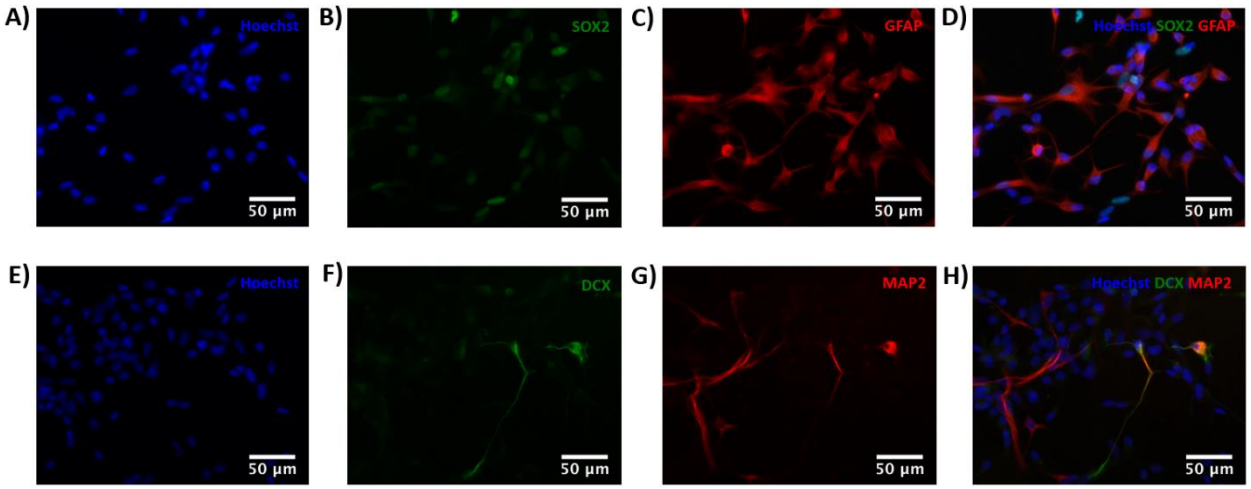

Figure 5.6: Typical fluorescence microscopy images of two separate sets of immunostained hNSPCs on reflectin-coated substrates after differentiation into (A–D) astrocytes and (E–H) neurons. The cells were costained with A) the nuclei marker Hoechst, B) the stem/progenitor cell marker SOX2, and C) the astrocytic marker GFAP. The image corresponding to all three markers is shown in D), where SOX2-negative/GFAP-positive cells are differentiated astrocytes. The neurons were costained with E) the nuclei marker Hoechst, F) the neuronal marker DCX, and G) the neuronal marker MAP2. The image corresponding to all three markers is shown in H), where MAP2-positive and DCX-positive cells are neurons.

5.4 Conclusion

In summary, we have discovered that reflectin constitutes an effective material for cell growth and differentiation, as demonstrated for traditionally difficult-to-culture hNSPCs. The viability of the reflectin-bound neural stem cells was assessed with a combination of phase-contrast, bright-field, and fluorescence microscopy techniques. Overall, our studies indicate that reflectin is quite comparable to alternative neural stem cell matrix materials.

Here, we note that our experiments may be quite interesting from the perspective of developmental and cell biology. For example, reflectin's unexpected presence during key stages of brain development in Sepia officinalis embryos, together with its functionality as a surface for hNSPC growth, hint that the protein may potentially play some as-of-yet undetermined general role in cephalopod nervous system development. Moreover, given that positively charged reflectin is similar to fibronectin and laminin, but superior to positively charged poly-d-lysine, as a cell growth substrate, its unusual amino acid sequence[30-32,34] may influence stem cell binding and/or

proliferation. These possibilities are exciting and certainly warrant further exploration, especially within the context of cephalopods as general comparative model systems for vertebrates.

Finally, our findings hold particular significance from the perspective of bioelectronic applications. Indeed, relatively few materials have been shown to simultaneously exhibit excellent electrical properties and support stem cell attachment, proliferation, and differentiation.[54-60] Reflectin's ability to serve as a substrate for neural stem cell growth therefore establishes the groundwork for interfacing hNSPCs with protein-based protonic devices and raises the intriguing possibility of directly regulating neurogenesis with protonic currents. Moreover, in contrast with some traditional neural stem cell growth materials, reflectin possesses a similar refractive index to glass, making it nearly ideal for TIRFM measurements. The protein's combination of favorable optical and electrical properties thus opens an opportunity for the spectroelectrochemical triggering and monitoring of ion channel activity in single isolated neural stem cells. Together, these advantages portend favorably for the future of reflectin as an inherently biocompatible active layer in a diverse array of bioelectronic devices.

5.5 Supplementary Information

Statement of Ethics: Informed written consent was obtained for all human subjects. All human cell research involved cells with no patient identifiers and was approved by the University of California, Irvine Institutional Review Board and the Human Stem Cell Research Oversight Committee.

Expression, Purification, and Characterization of Reflectin: Reflectin was prepared according to previously reported protocols.[26,27,35,36] An *E. coli* codon optimized gene coding for 6X histidine-tagged reflectin A1 protein from *Doryteuthis pealeii* (Genbank: ACZ57764.1) was synthesized

and cloned into the pJExpress414 vector (DNA2.0). The vector was transformed into BL21(DE3) cells (Novagen). Reflectin was expressed at 37 °C using Overnight Express Instant Terrific Broth (TB) media (Novagen) supplemented with 100 μg mL^{-1} Carbenicillin. Reflectin was completely insoluble when expressed at 37 °C and was sequestered in inclusion bodies prepared using BugBuster (Novagen) according to the manufacturer's suggested protocols. The inclusion bodies were then solubilized in denaturing buffer (pH 7.4, 50 mM sodium phosphate, 300 mM sodium chloride, 6 M guanidine hydrochloride) and purified under denaturing conditions on a HisPur Cobalt Resin gravity column (Thermo Scientific) according to the manufacturer's protocols (elution was performed using denaturing buffer supplemented with 250 mM imidazole). The fractions containing the reflectin protein were pooled and concentrated on an Amicon Concentrator (Millipore) before being purified with high performance liquid chromatography (HPLC) on an Agilent 1260 Infinity system using a reverse phase C18 column. The gradient was evolved from 95% Buffer A:5% Buffer B to 5% Buffer A:95% Buffer B at a flow rate of 0.5 mL min^{-1} over 20 min (Buffer A: 99.9% water, 0.1% trifluoroacetic acid; Buffer B: 95% acetonitrile, 4.9% water, 0.1% trifluoroacetic acid). After purification, the identity of the protein was confirmed with Sodium dodecyl sulfate polyacrylamide gel electrophoresis (SDS-PAGE) and in-gel tryptic digestion, followed by mass spectrometry analysis. The pure reflectin was pooled, flash frozen in liquid nitrogen, and lyophilized. Protein concentrations and yields were quantified via the Bradford protein assay (BioRad) with BSA as the standard.

Fabrication of Reflectin-Coated Substrates: Reflectin-coated substrates were prepared according to previously reported procedures.[26,27,35,36] For bright-field microscopy experiments, reflectin films were fabricated on silica substrates (SQI), and for phase contrast optical microscopy

and fluorescence microscopy experiments, reflectin films were fabricated on glass coverslips (ThermoFisher). In a typical experiment, uncoated substrates were first cleaned sequentially with Milli-Q water, acetone, and isopropanol, as well as flame-sterilized with a Bunsen burner. A fresh 10–20 mg/mL reflectin solution was then prepared and filtered through sterile 0.45 and 0.22 μm filters (ThermoFisher). Subsequently, Teflon tape (McMaster-Carr) was applied to edges of the substrates to act spacer for coating. The reflectin protein solution was then cast onto the substrate in front of a plastic blade, which was translated at a constant speed across the surface to produce films. To promote water evaporation, the coating procedure was performed at 80 °C. Note that the absence of a graphene oxide adhesion layer[26,27] reduced film uniformity over large areas.

Growth of HEK, BV2, and MDA-MB-231 Cell Cultures: The HEK cells were a gift from Dr. Naoto Hoshi, the BV2 cells were a gift from Dr. Heike Wulff, and the MDA-MB-231 cells were purchased from ATCC. HEK, BV2, and MDA-MB-231 cells were plated at densities of 20,000–105,000 cells/cm^2. The cells were grown as adherent cultures according to known procedures[42-50] at 37 °C and under 5% CO_2 in DMEM (Life Technologies), supplemented with 10% fetal bovine serum (Gemini Bio-Products) and 1% penicillin/streptomycin.

Growth of Adherent Human Neural Stem/Progenitor Cell Cultures: hNSPCs denoted as SC27 were procured from the National Human Neural Stem Cell Resource.[61-63] The hNSPCs were originally derived from brain subventricular zone (SVZ) tissue of a premature neonate that died shortly after birth, as previously described.[61,62] For donation of the requisite brain tissue, informed consent was obtained prior to tissue acquisition, and this process was approved by the Institutional Review Board.[61,62] In our studies, the cells were plated at densities of 40 000–80 000 cells per 18

mm coverslip. The cells were grown as adherent cultures at 37 °C and under 5% CO_2 in base proliferation media, which consisted of DMEM:F12 (Gibco/Invitrogen), 20% (v/v) BIT 9500 (bovine serum albumin, insulin, and transferrin) (Stem Cell Technologies), and 1% (v/v) antibiotic/antimycotic (penicillin, streptomycin, and amphotericin) (Gibco/Invitrogen). This media was supplemented with 40 ng/mL epidermal growth factor (EGF) (BD Biosciences), 40 ng/mL fibroblast growth factor (FGF) (BD Biosciences), and 20 ng/mL platelet-derived growth factor (PDGF-AB) (Peprotech). To induce differentiation, the base media was exchanged for the differentiation media, which consisted of a 1:1 mixture of the base media and Neurobasal media (Invitrogen) supplemented with 0.5% (v/v) B27 (Life Technologies), 20 ng/mL brain-derived neurotrophic factor (BDNF) (Peprotech), 20 ng/mL neurotrophin-3 (NT3) (Peprotech), 1% (v/v) fetal bovine serum (FBS) (Gibco/Invitrogen), 2.5 ng/mL FGF, and 0.1 μM all-trans-retinoic acid (Sigma). The cells were maintained in the differentiation media for a minimum of 14 days.

Optical Microscopy of Adherent Mammalian Cells: Bright-field microscopy images of HEK, BV2, and MDA-MB-231 cells were obtained with a Carl Zeiss Axio Imager A1 microscope in a 145 mM NaCl, 3 mM KCl, 3 mM $CaCl_2$, 2 mM $MgCl_2$, 5 mM Hepes, pH = 7.3 buffer solution. Phase contrast optical microscopy images of hNSPC cells were obtained with either an Advanced Microscopy Group EVOS XL microscope or an Olympus IX71 microscope, which was outfitted with a Hamamatsu C8484 digital camera. The hNSPC images were collected in the base proliferation media. To quantify cell densities, the images were analyzed with FIJI software.[70]

Fluorescence Microscopy of Immunostained Human Neural Stem/Progenitor Cells: Fluorescence microscopy images of immunostained hNSPCs were obtained with a Nikon Eclipse Ti microscope and acquired with NIS element AR3.10 software. For imaging, the differentiated

hNSPCs were first fixed by treatment with 4% paraformaldehyde for 10 min. These fixed cells were then treated with 0.3% Triton X-100 in phosphate-buffered saline (PBS) for 5 min, followed by blocking in 5% bovine serum albumin in PBS for 1 h. All cell nuclei were stained with Hoechst 33342 at 1:500 (2 μg/mL) in PBS for 1 min. To detect astrocytes, the cells were stained with mouse anti-GFAP (Sigma) and goat anti-SOX-2 (Santa Cruz Biotechnology) primary antibodies for 2 h at room temperature. To detect neurons, the cells were stained with mouse anti-MAP2 (Sigma) and goat anti-DCX (Santa Cruz Biotechnology) primary antibodies for 2 h at room temperature. Both neurons and astrocytes were stained with donkey antimouse Alexa-Fluor 555 (Life Technologies) and donkey antigoat Alexa-Fluor 488 (Life Technologies) secondary antibodies for 1 h in the dark at room temperature. The primary and secondary antibodies were diluted at 1:200 in 1% bovine serum albumin in PBS solution. To compensate for a lower neuron differentiation percentage, hNSPCs were plated at densities of 80 000 cells per 18 mm coverslip for neurons and at 40 000 cells per 18 mm coverslip for astrocytes. The images were analyzed with FIJI software.[70]

Total Internal Reflection Fluorescence Microscopy Imaging of Adherent Human Neural Stem/Progenitor Cells: Fluorescence microscopy images were obtained by using an Olympus IX71 microscope equipped with an Andor iXon EMCCD camera, a Melles Griot 488 nm solid-state laser, and a 1.49 NA Olympus 100x objective lens. The images were collected with an exposure time of 0.04081 s at 13.7 Hz. For Ca^{2+} imaging, the hNSPC cells were loaded with a Ca^{2+} indicator by incubation in a solution of 1 μM Fluo-4 AM in phenol red-free DMEM/F12 (Invitrogen) for 10 min at 37 °C. The cells were then washed three times and further incubated at room temperature for another 10–15 min to allow for intracellular cleavage of the AM ester. The total internal reflection fluorescence microscopy images were obtained in a 148 mM NaCl, 3 mM

KCl, 3 mM $CaCl_2$, 2 mM $MgCl_2$, 8 mM glucose, 10 mM Hepes, pH = 7.3 buffer solution. The images were analyzed with FIJI[70] and Origin 9.1 software.

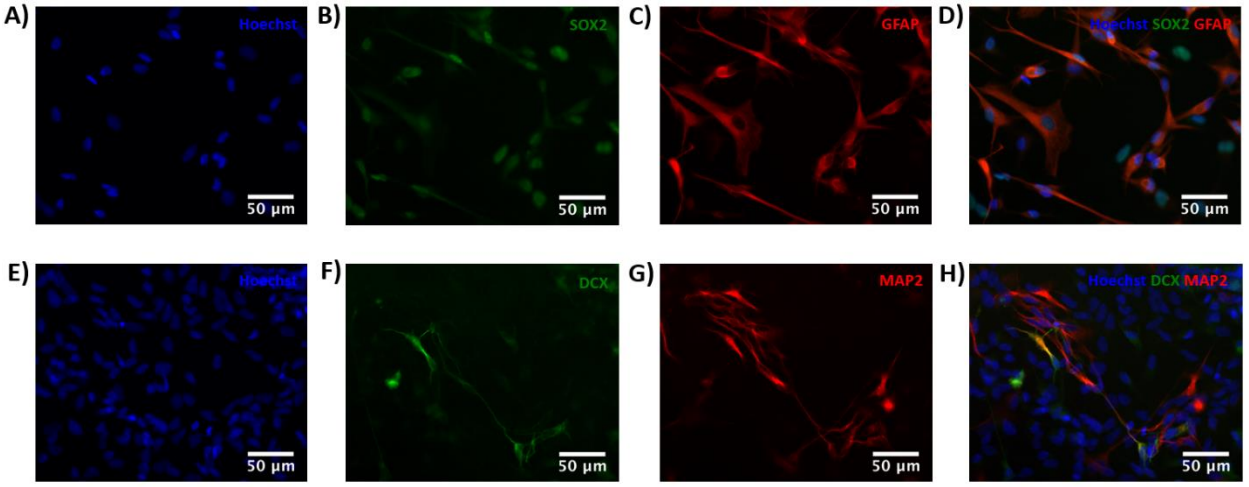

Figure S5.1: Typical fluorescence microscopy images of two separate sets of immunostained hNSPCs on laminin-coated substrates after differentiation into A)-D) astrocytes and E)-H) neurons. The cells were co-stained with A) the nuclei marker Hoechst, B) the stem/progenitor cell marker SOX2, and C) the astrocytic marker GFAP. The image corresponding to all three markers is shown in D), where SOX2-negative and GFAP-positive cells are differentiated astrocytes. The neurons were co-stained with E) the nuclei marker Hoechst, F) the neuronal marker DCX, and G) the neuronal marker MAP2. The image corresponding to all three markers is shown in H), where MAP2-positive and DCX-positive cells are neurons.

5.6 Acknowledgements

This chapter is an adaptation of the material as it appears in: L. Phan, R. Kautz, J. Arulmoli, I. H. Kim, D. T. T. Le, M. A. Shenk, M. M Pathak, L. A. Flanagan, F. Tombola, A. A. Gorodetsky, *ACS Appl. Mater. Interfaces*, 2016, **8**, 278–284. The co-authors listed in this publication directed and supervised research which forms the basis for the material in the chapter. Author Contributions: L. P., R. K., J. A., I. H. K., M. M. P., L. A. F., F. T., and A. A. G. conceptualized and designed the experiments; L. P., R. K., J. A., I. H. K., D. T. T. L., and M. A. S. performed the research; L. P. and R. K. expressed and purified the protein; L. P., R. K., M. M. P., L. A. F., F. T., and A. A. G. analyzed the data; and L. P., R. K., and A. A. G. wrote the paper.

5.7 References

1. Hanlon, R. T.; Messenger, J. B. Cephalopod Behaviour, Cambridge University Press, Cambridge, 1996.
2. Mäthger, L. M.; Denton, E. J.; Marshall, N. J.; Hanlon, R. T. Mechanisms and Behavioural Functions of Structural Coloration in Cephalopods *J. R. Soc. Interface.* **2009**, *6*, 149.
3. Hanlon, R. T.; Chiao, C. C. C.; Mäthger, L. M.; Buresch, K. C.; Barbosa, A.; Allen, J. J.; Siemann, L.; Chubb, C. Rapid Adaptive Camouflage in Cephalopods, in Animal Camouflage: Mechanisms and Function, Cambridge University Press, Cambridge, 2011.
4. Abbott, N.J.; Williamson, R.; Maddock, L. Cephalopod Neurobiology: Neuroscience Studies in Squid, Octopus, and Cuttlefish, Oxford University Press, Oxford, 1995.
5. Nixon, M.; Young, J. Z. The Brains and Lives of Cephalopods, Oxford University Press, Oxford, 2003.
6. Borrelli, L.; Fiorito, G. Behavioral Analysis of Learning and Memory in Cephalopods. In: Byrne JJ Learning and Memory: A Comprehensive Reference, Academic Press, Oxford, 2008.
7. Sandeman, D. Homology and Convergence in Vertebrate and Invertebrate Nervous Systems. *Naturwissenschaften* **1999**, *86*, 378.
8. Williamson, R.; Chrachri, A. Cephalopod Neural Networks. *Neurosignals* **2004**, *13*, 87.
9. Grant, P.; Zheng, Y.; Pant, H. C. Squid (*Loligo pealei*) Giant Fiber System: A Model for Studying Neurodegeneration and Dementia? *Biol. Bull.* **2006**, *210*, 318.
10. Hochner, B.; Shomrat, T.; Fiorito, G. The Octopus: A Model for a Comparative Analysis of the Evolution of Learning and Memory Mechanisms. *Biol. Bull.* **2006**, *210*, 308.

11. Walters, E. T.; Moroz, L. L. Molluscan Memory of Injury: Evolutionary Insights into Chronic Pain and Neurological Disorders. *Brain. Behav. Evol.* **2009**, *74*, 206.
12. Williams, L. W. The Anatomy of the Common Squid, *Loligo* pealii, Lesueur. The Library and Printing Office of E. J. Brill: Leiden, 1910.
13. Young, J. Z. Structure of Nerve Fibres in Sepia. *J. Physiol.* **1935**. *83*, 27.
14. Bullock, T. H. Properties of a Single Synapse in the Stellate Ganglion of Squid. *J. Neurophysiol* **1948**, *11*, 343.
15. Sereni, E.; Young, J. Z. Nervous Degeneration and Regeneration in Cephalopods. *Pubbl. Stast. Zool. NapoU*. **1932**, *13*, 173.
16. Hodgkin, A. L.; Huxley, A. F. A Quantitative Description of Membrane Current and its Application to Conduction and Excitation in Nerve. *J. Physiol.* **1952**, *117*, 500.
17. Bloedel, J.; Gage, P. W.; Llina´s, R.; Quastel, D. M. Transmitter Release at the Squid Giant Synapse in the Presence of Tetrodotoxin. *Nature* **1966**, *212*, 49.
18. Katz, B.; Miledi, R. Input–output Relation of a Single Synapse. *Nature* **1966**, *212*, 1242.
19. Florey, E.; Dubas, F.; Hanlon, R. T. Evidence for L-glutamate as a Transmitter Substance of Motor Neurons Innervating Squid Chromatophore Muscles. *Comp. Biochem. Physiol.* **1985**, *82C*, 259.
20. Kreit, E.; Mäthger, L. M.; Hanlon, R. T.; Dennis, P. B.; Naik, R. R.; Forsythe, E.; Heikenfeld, J. Biological vs. Electronic Adaptive Coloration: How Can One Inform the Other? *J. R. Soc.* **2013**, *10*, 20120601
21. Manakasettharn, S.; Taylor, J. A.; Krupenkin, T. N. Bio-inspired Artificial Iridophores Based on Capillary Origami: Fabrication and Device Characterization. *Appl. Phys. Lett.* **2011** *99*, 144102.

22. Morin, S. A.; Shepherd, R. F.; Kwok, S. W.; Stokes, A. A.; Nemiroski, A.; Whitesides, G. M. Camouflage and Display for Soft Machines. *Science* **2012**, *337*, 828.

23. Rossiter, J.; Yap, B.; Conn, A. Biomimetic Chromatophores for Camouflage and Soft Active Surfaces. *Bioinspiration Biomimetics* **2012**, *7*, 036009.

24. Yu, C; Li, Y.; Zhang, X.; Huang, X.; Malyarchuk, V.; Wang, S.; Shi, Y.; Gao, L.; Su, Y.; Zhang, Y.; Xu, H.; Hanlon, R. T.; Huang, Y.; Rogers, J. A. Adaptive Optoelectronic Camouflage Systems with Designs Inspired by Cephalopod Skins. *Proc. Natl. Acad. Sci. U. S. A.* **2014**, *111*, 12998.

25. Wang, Q.; Gossweiler, G. R.; Craig, S. L.; Zhao, X. Cephalopod-inspired Design of Electro- mechanochemically Responsive Elastomers for On-demand Fluorescent Patterning. *Nat. Commun.* **2014**, *5*, 4899.

26. Phan, L.; Walkup IV, W. G.; Ordinario, D. D.; Karshalev, E.; Jocson, J. M.; Burke, A. M.; Gorodetsky, A. A. Reconfigurable Infrared Camouflage Coatings from a Cephalopod Protein. *Adv. Mater.* **2013**, *25*, 5621.

27. Phan, L.: Ordinario, D. D.; Karshalev, E.; Walkup IV, W. G.; Shenk, M. A.; Gorodetsky, A. A. Infrared Invisibility Stickers Inspired by Cephalopods. *J. Mater. Chem. C* **2015,** *3*, 6493-6498.

28. Kramer, R. M.; Crookes-Goodson, W. J.; Naik, R. R. The Self-organizing Properties of Squid Reflectin Protein. *Nat. Mater.* **2007**, *6*, 533.

29. Qin, G.; Dennis, P. B.; Zhang, Y.; Hu, X.; Bressner, J. E.; Sun, Z.; Crookes-Goodson, W. J.; Naik, R. R.; Omenetto, F. G.; Kaplan, D. L. Recombinant Reflectin-based Optical Materials. *J. Polym. Sci., Part B: Polym. Phys.* **2013**, *51*, 254.

30. Crookes, W. J.; Ding, L. L.; Huang, Q. L.; Kimbell, J. R.; Horwitz, J.; McFall-Ngai, M. J. Reflectins: The Unusual Proteins of Squid Reflective Tissues. *Science* **2004**, *303*, 235.
31. Izumi, M.; Sweeney, A. M.; DeMartini, D.; Weaver, J. C.; Powers, M. L.; Tao, A.; Silvas, T. V.; Kramer, R. M.; Crookes-Goodson, W. J.; Mäthger, L. M.; Naik, R. R.; Hanlon, R. T.; Morse, D. E. Changes in Reflectin Protein Phosphorylation Are Associated with Dynamic Iridescence in Squid. *J. R. Soc., Interface* **2010**, *7*, 549.
32. Tao, A. R.; DeMartini, D. G.; Izumi, M.; Sweeney, A. M.; Holt, A. L.; Morse, D. E. The Role of Protein Assembly in Dynamically Tunable Bio-optical Tissues. *Biomaterials* **2010**, *31*, 793.
33. DeMartini, D. G.; Krogstad, D. V.; Morse, D. E. Membrane Invaginations Facilitate Reversible Water Flux Driving Tunable Iridescence in a Dynamic Biophotonic System. *Proc. Natl. Acad. Sci. U. S. A.* **2013**, *110*, 2552.
34. DeMartini, D. G.; Izumi, M.; Weaver, A. T.; Pandolfi, E.; Morse, D. E. Structures, Organization, and Function of Reflectin Proteins in Dynamically Tunable Reflective Cells. *J. Biol. Chem.* **2015**, DOI: 10.1074/jbc.M115.638254.
35. Ordinario, D. D.; Phan, L.; Walkup IV, W. G.; Jocson, J. M.; Karshalev, E.; Hüsken, N.; Gorodetsky, A. A. Bulk Protonic Conductivity in a Cephalopod Structural Protein. *Nat. Chem*. **2014**, *6*, 596.
36. Ordinario, D. D.; Phan, L.; Jocson, J. M.; Nguyen, T.; Gorodetsky, A. A. Protonic Transistors From Thin Reflectin Films. *APL Mater.* **2015**, *3*, 014907.
37. Bonnaud-Ponticelli, L.; Bassaglia, Y. Cephalopod Development: What We Can learn from Differences. *OA Biology* **2014**, *2*, 6.
38. Bassaglia, Y.; Buresi, A.; Franko, D.; Andouche, A.; Baratte, S,; Bonnaud, L. Sepia

officinalis: A New Biological Model for Eco-Evo-Devo Studies. *J. Exp. Mar. Biol. Ecol.* **2013,** *447*, 4.

39. Navet, S.; Baratte, S.; Bassaglia, Y.; Andouche, A.; Buresi, A.; Bonnaud, L. Neurogenesis in Cephalopods: "Eco-Evo-Devo" Approach in the Cuttle Sepia officinalis (Mollusca-Cephalopoda) *Journal of JASNAOE*, **2014**, *22*, 15.
40. Bassaglia, Y.; Bekel, T.; Da Silva, C.; Poulain, J.; Andouche, A.; Navet, S.; Bonnaud, L. ESTs Library from Embryonic Stages Reveals Tubulin and Reflectin Diversity in Sepia officinalis (Mollusca – Cephalopoda). *Gene* **2012**, *498*, 203.
41. Andouche, A.; Bassaglia, Y.; Baratte, S.; Bonnaud, L. Reflectin Genes and Development of Iridophore Patterns in Sepia officinalis Embryos (Mollusca, Cephalopoda) *Dev. Dyn.* **2013**, *242*, 560.
42. *Growth and Maintenance of the 293A Cell Line*, Invitrogen Corporation, Carlsbad, 2003.
43. Graham, J.; Smiley, W. C.; Russell, R. Characteristics of a Human Cell Line Transformed by DNA from Human Adenovirus Type. *J. Gen. Virol.* **1977**, *36*, 59.
44. Thomas, P.; Smart, T. G. HEK293 Cell Line: A vehicle for the Expression of Recombinant Proteins. *J. Pharmacol. Toxicol. Methods* **2005**, *51*, 187.
45. American Type Culture Collection. MDA-MB-231 (ATCC HTB-26). http://www.atcc.org/products/all/HTB-26.aspx?geo_country=us (accessed June 23, 2015).
46. Cailleau, R.; Young, R.; Olivé, M.; Reeves Jr., W. J. Breast Tumor Cell Lines from Pleural Effusions. *J. Natl. Cancer Inst. (1940-1978)* **1974**, *53*, 3.
47. Holliday, D. L.; Speirs, V. Choosing the Right Cell Line for Breast Cancer Research. *Breast Cancer Res.* **2011**, *13*, 215.

48. Blasi, E.; Barluzzi, R.; Bocchini, V.; Mazzolla, R.; Bistoni, F. Immortalization of Murine Microglial Cells by a v-raf/v-myc Carrying Retrovirus. *J. Neuroimmunol.* **1990**, *27*, 229.
49. Bocchini, V.; Mazzolla, R.; Barluzzi, R.; Blasi, E.; Sick, P.; Kettenmann, H. An Immortalized Cell Line Expresses Properties of Activated Microglial Cells. *J. Neurosci. Res.* **1992**, *31*, 616.
50. Stansley, B.; Post, J.; Hensley, K. A Comparative Review of Cell Culture Systems for the Study of Microglial Biology in Alzheimer's. *J. Neuroinflammation* **2012**, *9*, 115.
51. Gage, F. H. Mammalian Neural Stem Cells. *Science* **2000**, *287*, 1433.
52. Kornblum, H. I. Introduction to Neural Stem Cells. *Stroke* **2007**, *38*, 810.
53. Gage, F. H.; Temple, S. Neural Stem Cells: Generation and Regenerating the Brain. *Neuron* **2013**, *80*, 588.
54. Willerth, S. M.; Sakiyama-Elbert, S. E. *Combining Stem Cells and Biomaterial Scaffolds for Constructing Tissues and Cell Delivery*, Harvard Stem Cell Institute, Cambridge, 2008.
55. Little, L.; Healy, K. E.; Schaffer, D. V. Engineering Biomaterials for Synthetic Neural Stem Cell Microenvironments. *Chem. Rev.* **2008**, 108, 1787.
56. Yao, S.; Liu, X.; Wang, X.; Merolli, A.; Chen, X.; Cui, F. Directing Neural Stem Cell Fate with Biomaterial Parameters for Injured Brain Regeneration. *Prog. Nat. Sci.* **2013**, *23*, 103.
57. Discher, D. E.; Mooney, D. J.; Zandstra, P. W. Growth Factors, Matrices, and Forces Combine and Control Stem Cells. *Science* **2009**, *324*, 1673.
58. Lutolf, M. P.; Gilbert, P. M.; Blau, H. M. Designing Materials to Direct Stem-Cell Fate. *Nature* **2009**, *462*, 433.

59. Celiz, A. D.; Smith, J. G. W.; Langer, R.; Anderson, D. G.; Winkler, D. A.; Barrett, D. A.; Davies, M. C.; Young, L. E.; Denning, C.; Alexander, M. R. Materials for Stem Cell Factories of the Future. *Nat. Mater.* **2014**, *13*, 570.

60. Murphy, W. L.; McDevitt, T. C.; Engler, A. J. Materials as Stem Cell Regulators. *Nat. Mater.* **2014**, *13*, 547.

61. Palmer, T. D.; Schwartz, P. H.; Taupin, P.; Kaspar, B.; Stein, S. A.; Gage, F. H. Cell Culture: Progenitor Cells from Human Brain after Death. *Nature* **2001**, *411*, 42.

62. Schwartz, P. H.; Bryant, P. J.; Fuja, T. J.; Su, H.; O'Dowd, D. K.; Klassen, H. Isolation and Characterization of Neural Progenitor Cells from Post-Mortem Human Cortex. *J. Neurosci. Res.* **2003**, *74*, 838.

63. Flanagan, L. A.; Rebaza, L. M.; Derzic, S.; Schwartz, P. H.; Monuki, E. S. Regulation of Human Neural Precursor Cells by Laminin and Integrins. *J. Neurosci. Res.* **2006**, *83*, 845.

64. Labeed, F. H.; Lu, J.; Mulhall, H. J.; Marchenko, S. A.; Hoettges, K. F.; Estrada, L. C.; Lee, A. P.; Hughes, M. P.; Flanagan, L. A. Biophysical Characteristics Reveal Neural Stem Cell Differentiation Potential. *PLoS ONE* **2011** *6*, e25458.

65. Pistollato, F.; Chen, H. L.; Schwartz, P. H.; Basso, G.; Panshision, D. M. Oxygen Tension Controls the Expansion of Human CNS Precursors and the Generation of Astrocytes and Oligodendrocytes. *Mol. Cell. Neurosci.* **2007**, *35*, 424.

66. Lee, J. P.; Jeyakumar, M.; Gonzalez, R.; Takahashi, H.; Lee, P. J.; Baek, R. C.; Clark ,D.; Rose, H.; Fu, G.; Clarke, J.; McKercher, S.; Meerloo, J.; Muller, F. J.; Park, K. I.; Butters, T. D.; Dwek, R. A.; Schwartz, P.; Tong, G.; Wenger, D.; Lipton, S. A.; Seyfried, T. N.; Platt, F. M.; Snyder, E. Y. Stem Cells Act Through Multiple Mechanisms to Benefit Mice with Neurodegenerative Metabolic Disease. *Nat. Med.* **2007**, *13*, 439.

67. Pathak, M. M.; Nourse, J. L.; Tran, T.; Hwe, J.; Arulmoli, J.; Le, D. T. T.; Bernardis, E.; Flanagan, L. A.; Tombola, F. Stretch-Activated Ion Channel Piezo1 Directs Lineage Choice in Human Neural Stem Cells. *Proc. Natl. Acad. Sci. U. S. A.* **2014**, *111*, 16148.
68. Axelrod, D.; Total Internal Reflection Fluorescence Microscopy. *Methods Cell Biol.* **2008**, *89*, 169.
69. Axelrod, D. Total Internal Reflection Fluorescence Microscopy in Cell Biology. *Traffic* **2001**, *2*, 764.
70. Schindelin, J.; Arganda-Carreras, I.; Frise, E.; Kaynig, V.; Longair, M.; Pietzsch, T.; Preibisch, S.; Rueden, C.; Saalfeld, S.; Schmid, B.; Tinevez, J. Y.; White, D. J.; Hartenstein, V.; Eliceiri, K.; Tomancak, P.; Cardona, A. Fiji: An Open-Source Platform for Biological–Image Analysis. *Nature Methods* **2012**, *9*, 676.

CHAPTER 6 Production and Electrical Characterization of the Reflectin A2 Isoform from *Doryteuthis (Loligo) pealeii*

6.1: Abstract

Cephalopods have recently emerged as a source of inspiration for the development of novel functional materials. Within this context, a number of studies have explored structural proteins known as reflectins, which play a key role in cephalopod adaptive coloration in vivo and exhibit interesting properties in vitro. Herein, we report an improved high-yield strategy for the preparation and isolation of reflectins in quantities sufficient for materials applications. We first select the *Doryteuthis* (*Loligo*) *pealeii* reflectin A2 (RfA2) isoform as a "model" system and validate our approach for the expression and purification of this protein. We in turn fabricate RfA2-based two terminal devices and employ both direct and alternating current measurements to demonstrate that RfA2 films conduct protons. Our findings underscore the potential of reflectins as functional materials and may allow a wider range of researchers to investigate their properties.

6.2: Introduction

Cephalopods (squid, octopuses, and cuttlefish) are well known for their sophisticated neurophysiology, complex behavior, and stunning camouflage displays.[1–6] Recently, these animals have drawn significant attention as sources of novel materials for optical systems,[7–10] biomedical technologies,[11–15] and bioelectronic devices.[16–20] Within this context, a number of literature reports have investigated the properties of unique structural proteins known as reflectins,[7–10,14,16–18,21–24] which are found in cephalopod skin cells (*i.e.* leucophores, iridophores, and chromatophores).[25–30] *In vivo*, reflectins in general have been shown to play important roles in cephalopod adaptive coloration by serving as components of optically-active ultrastructures, including layered stacks

of membrane-enclosed platelets in iridophores,[25,26] membrane-bound arrangements of spherical microparticles in leucophores,[27,28] and interconnected networks of pigment granules in chromatophores.[29,30] *In vitro*, the *Doryteuthis (Loligo) pealeii* reflectin A1 (RfA1) isoform has found applications in reconfigurable infrared camouflage coatings that are actuated by chemical and mechanical stimuli,[7,8] proton-conducting films with electrical figures of merit rivaling those of some artificial analogues,[16–18] and biocompatible substrates that support the proliferation and differentiation of neural stem cells.[14] Overall, reflectins' fascinating properties have provided a strong impetus for their continued exploration from both fundamental and applied perspectives.

Herein, we describe an improved methodology for the production of difficult-to-handle reflectins in quantities sufficient for materials applications. We first select the *Doryteuthis (Loligo) pealeii* reflectin A2 (RfA2) isoform as a "model" system for electrical characterization and validate a new high-yield strategy for the expression and purification of this precipitation-prone protein. We subsequently fabricate and characterize two-terminal devices for which RfA2 thin films constitute the active layer. We in turn interrogate RfA2-based devices featuring palladium and palladium hydride electrodes *via* direct current electrical measurements and RfA2-based devices featuring gold electrodes *via* alternating current electrical measurements. From our experiments, we glean that RfA2 is an effective proton-conducting material, with properties similar to those of RfA1. Overall, our findings underscore the potential of reflectins as functional materials and may allow a wider range of researchers to investigate their properties.

6.3: Results and Discussion

Having previously demonstrated that *Doryteuthis (Loligo) pealeii* reflectin A1 is an excellent proton conductor,[16–18] we sought to extend these studies and explore the electrical

functionality of other reflectins. For our experiments, we specifically selected *Doryteuthis (Loligo) pealeii* reflectin A2 (Figure 6.1A) due to its key biological role in the dynamic optical functionality of iridophores[23,26] and its similarity to reflectins from other squid species (with the exception of reflectin B1). Indeed, RfA2 from *D. pealeii* features a >60% pair-wise amino acid sequence identity with the majority of isolated reflectins from *E. scolopes*,[21] *D. opalescens*,[26] and *L. forbesi*,[31] and much like its homologues, this reflectin variant contains multiple characteristic $(M/F–D–X_5)(M–D–X_5)_n(M–D–X_{3/4})$ sequence motifs and large percentages of both aromatic and charged amino acids (Figure 6.1A).[23,26] Furthermore, although the biochemical characterization of RfA2 has been reported,[23,24,26] the protein has not been studied as a functional material to date and possesses completely unexplored electrical properties. Given the aforementioned considerations, we viewed RfA2 as a judicious "model" reflectin for electrical characterization and further investigation.

We began our studies by developing and implementing an improved strategy for the production of RfA2 in high yield (Figure 6.1B), with each step of the revised procedure monitored *via* gel electrophoresis (Figure 6.1C). First, we used protocols validated for RfA1 to heterologously express histidine-tagged RfA2 in *E. coli*,[7,16] finding that the protein was sequestered within intracellular inclusion bodies (as reported for RfA1). The inclusion bodies were then prepared/isolated through several rounds of non-ionic detergent extraction and centrifugation. Subsequently, the nearly pure RfA2 (from the inclusion bodies) was solubilized through repeated manual agitation. Here, when attempting to purify the protein *via* immobilized metal ion affinity chromatography (IMAC), we found that even under denaturing conditions, RfA2 was prone to irreversible self-assembly into larger aggregates and/or spontaneous precipitation (as reported for some reflectins).[9,10,22,24] Our standard protocol[7,16] thus furnished relatively small amounts of

material, which were appropriate for basic characterization but not adequate for high throughput device fabrication. Consequently, rather than relying upon a time-consuming, expensive, and difficult IMAC step, we revised our procedure and simply filtered the RfA2 solutions to remove any insoluble debris and/or precipitates. We in turn isolated the desired protein from the filtrate *via* high performance liquid chromatography (HPLC), obtaining typical estimated purities of >95% (Figure S6.1). Finally, we confirmed the identity of the protein *via* in-gel tryptic digestion and tandem mass spectrometry, obtaining typical sequence coverages of >80% (Figure S6.2). Notably, due to the use of histidine-tagged RfA2, we were able to directly compare the efficacy of the previously reported[7,16] and current procedures, discovering that our new streamlined strategy not only avoided a challenging column chromatography step but also improved the yield by well over an order of magnitude to >200 mg of pure protein per liter of cell culture.

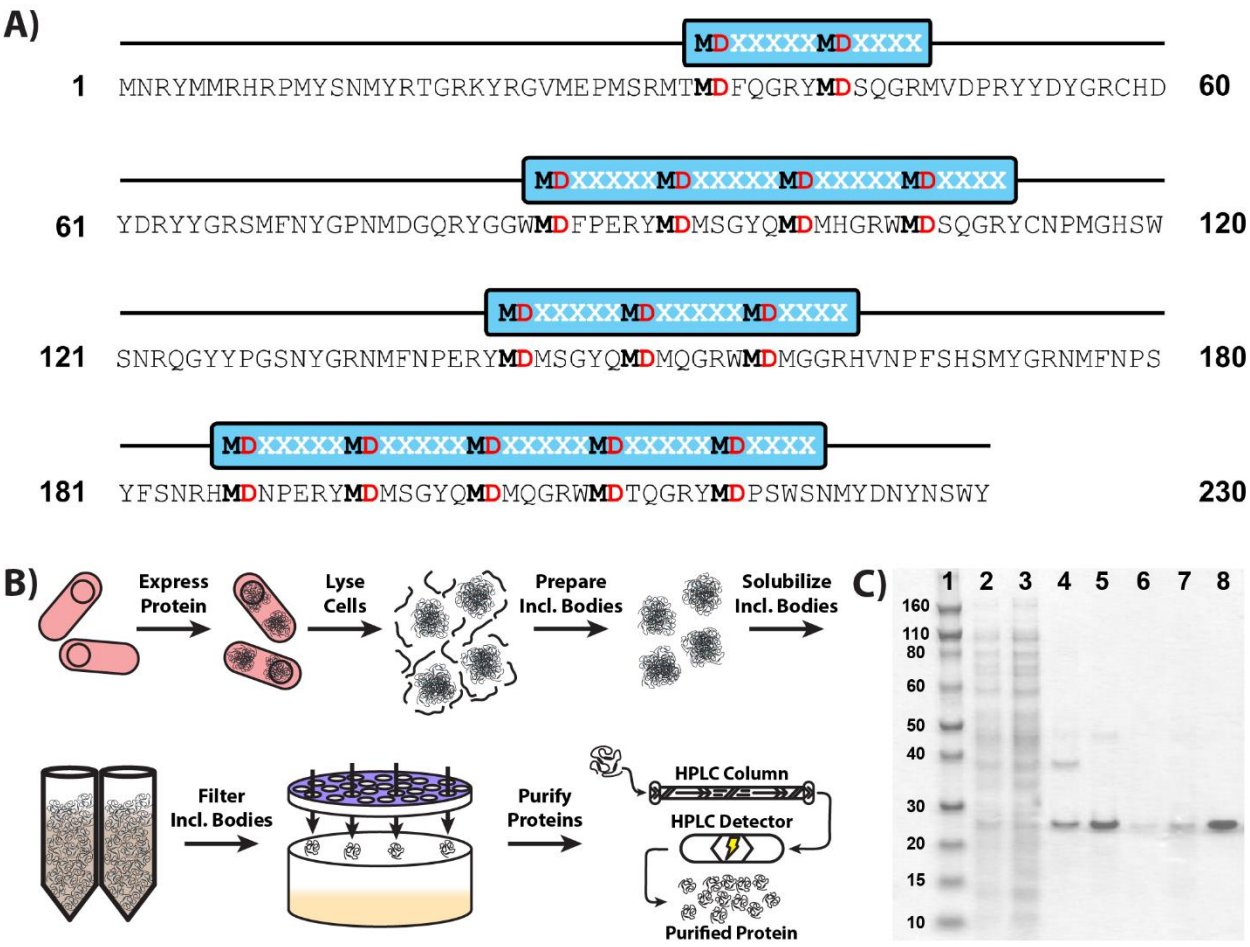

Figure 6.1: A) Illustration of the primary sequence of *Doryteuthis* (*Loligo*) *pealeii* reflectin A2. The conserved sequence motifs of the form $(M/F–D–X_5)(M–D–X_5)_n(M–D–X_{3/4})$ are indicated above the sequence in light blue. The conserved aspartic acid and methionine residues present in the subdomains are indicated in bolded red and bolded black, respectively. B) Illustration of the expression and purification of RfA2. The procedure entails protein expression, cell lysis, inclusion body preparation, inclusion body solubilization, inclusion body filtration, and protein purification via high performance liquid chromatography. C) Analysis of the expression and purification of RfA2 via sodium dodecyl sulfate polyacrylamide gel electrophoresis (SDS-PAGE). The stain indicates the total protein. The individual lanes correspond to: lane 1, 10–160 kDa molecular weight standards; lane 2, total protein; lane 3, soluble protein; lane 4, insoluble protein; lane 5, solubilized inclusion bodies; lane 6, filtered inclusion bodies; lane 7, concentrated filtered inclusion bodies; lane 8, HPLC eluate.

With our desired material in hand, we proceeded to fabricate two-terminal bottom contact devices according to the scheme illustrated in Figure 6.2A.[16–18] First, we prepared arrayed palladium or gold metal contacts on either silicon dioxide/silicon or glass substrates, respectively, *via* electron beam physical vapor deposition through a shadow mask. Next, we dropcast aqueous solutions of RfA2 directly onto the electrode arrays. We then allowed the residual solvent to evaporate, prior to removing excess material through mechanical scribing.

These arrayed devices enabled high throughput physical and electrical characterization of RfA2 films.

We next characterized our RfA2-based devices with optical microscopy and atomic force microscopy (AFM).[16–18] The optical microscopy experiments indicated that the RfA2 active layers contained few apparent defects (representative image for palladium-contacted devices is shown in Figure 6.2B). The AFM experiments indicated that the RfA2 films were relatively uniform with root mean square (RMS) roughnesses of >3 nm (representative image is shown in Figure 6.2C). The physical characterization experiments confirmed the integrity of our films and facilitated interpretation of the electrical measurements.

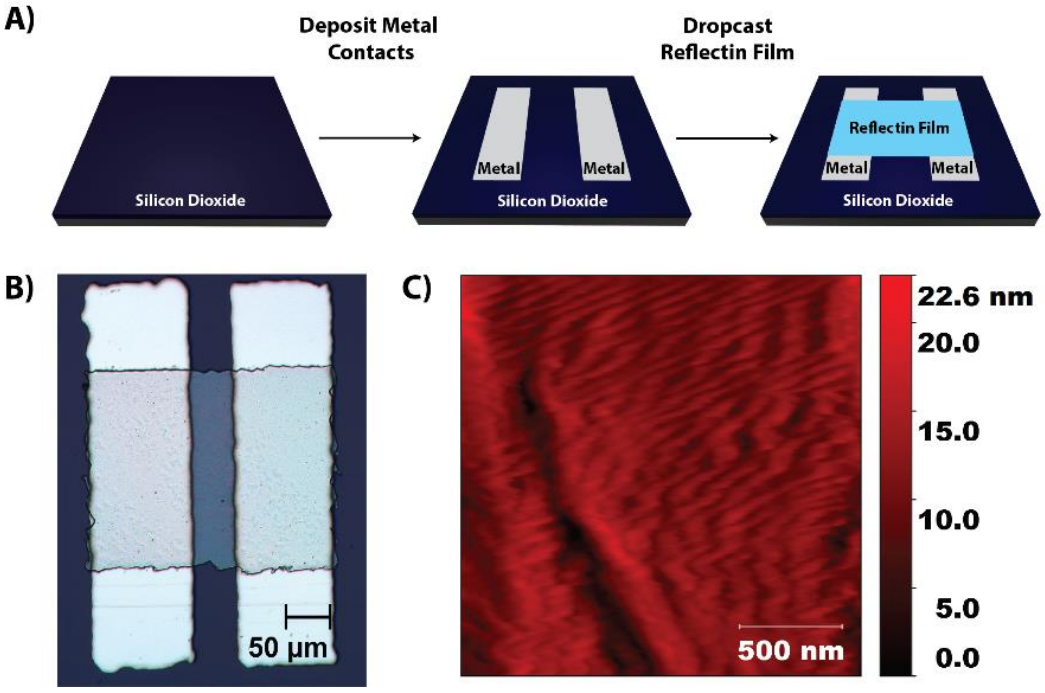

Figure 6.2: A) General scheme for the fabrication of RfA2-based devices. B) A representative optical image of a completed device for which an RfA2 film bridges two palladium electrodes. C) A representative atomic force microscopy (AFM) image of an RfA2 film.

We subsequently investigated the electrical properties of RfA2 films contacted by proton-blocking palladium and proton-injecting palladium hydride electrodes (Figure 6.3A). Thus, we first recorded current (I) as a function of voltage (V) at a relative humidity (RH) of 80% for

palladium-contacted devices (representative measurements are shown in Figure 6.3B). From the I–V characteristics, we extracted an average current density of $7.3 \pm 4.5 \times 10^{-4}$ A cm^{-2} at 1.5 V across 6 independent palladium-contacted devices. We in turn formed proton-transparent palladium hydride contacts via exposure of the palladium contacts to hydrogen gas in situ (Figure 6.3A),[16–20,32] prior to again recording current as a function of voltage at an RH of 80% (representative measurements are shown in Figure 6.3B). From the I–V characteristics, we extracted an average current density of $1.8 \pm 0.6 \times 10^{-2}$ A cm^{-2} at 1.5 V across 6 independent palladium hydride-contacted devices. Here, we found that the characteristics displayed hysteresis between the forward and reverse scans and that the observed current density increased by more than an order of magnitude upon conversion of the contacts from proton-blocking to proton-injecting (in close agreement with literature precedent for RfA1[16–18] and derivatized chitosan[19,20]). Interestingly, the current density found for RfA2 was lower than the current density of $\sim 2.6 \times 10^{-2}$ A cm^{-2} previously found for RfA1 at an RH = 80%.[16] This difference could be rationalized by analyzing the two proteins' histidine-tagged amino acid sequences (Figure S6.3); relative to RfA1, RfA2 possesses a small but significant decrease in its percentage of charged amino acids (which are crucial for proton transport)[16] and thus might be expected to function less effectively as a proton conductor. Altogether, our observations provided strong evidence that RfA2 was a proton-conducting material.

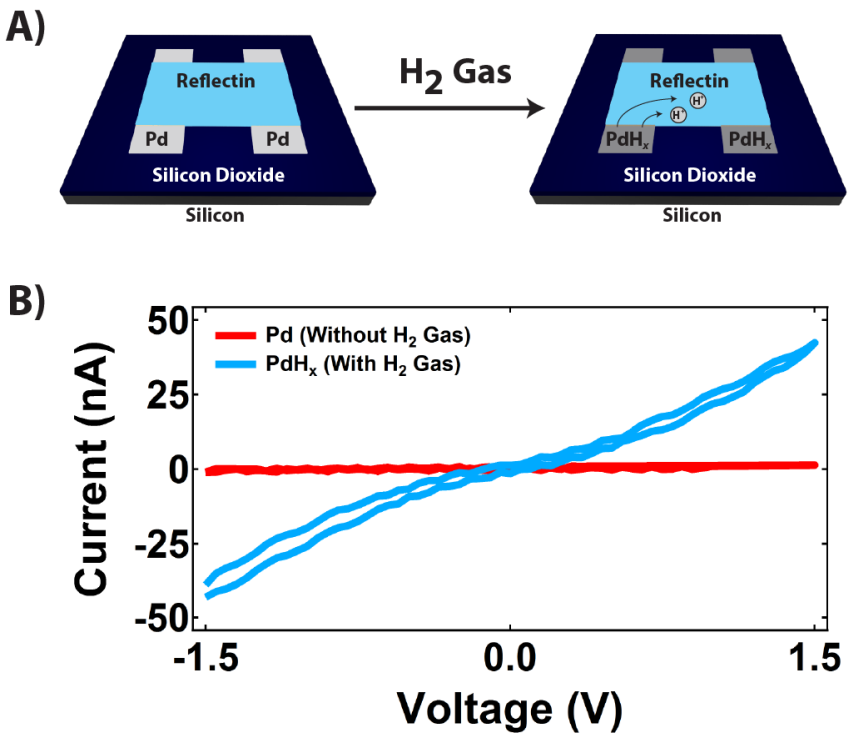

Figure 6.3: A) An illustration of an RfA2-based two-terminal device before and after in situ treatment with hydrogen (H_2) gas. The palladium (Pd) electrodes are converted to palladium hydride (PdH_x) electrodes in the presence of H_2, enabling the injection of protons into the film. B) The current versus voltage characteristics of an RfA2 film contacted with palladium (red) and palladium hydride (blue) electrodes. The magnitude of the current increases by more than an order of magnitude upon moving from proton-blocking to proton-injecting electrodes. Both the forward and reverse scans are shown for each measurement.

To gain additional insight into the electrical properties of RfA2, we used electrochemical impedance spectroscopy to interrogate RfA2 films contacted by gold electrodes in the presence of water (H_2O) and deuterium oxide (D_2O) vapor (Figure 6.4A). Thus, we first recorded Nyquist plots of the imaginary *versus* the real parts of the impedance at an RH of 80% for devices in the presence of H_2O (representative measurements are shown in Figure 6.4B). By fitting our curves with a simple equivalent circuit that accounted for the bulk impedance and capacitive effects at the electrodes,[16] we extracted an average conductivity of $7.4 \pm 2.0 \times 10^{-5}$ S cm^{-1} across 5 independent devices in the presence of H_2O. We in turn altered the environment from H_2O to D_2O vapor *in situ* (Figure 6.4A), prior to again recording the imaginary *versus* the real parts of the impedance at an RH of 80% (representative measurements are shown in Figure 6.4B). From fits of this data, we

extracted an average conductivity of 4.3 ± 1.1 × 10^{-5} S cm^{-1} across 5 independent devices in the presence of D_2O. Here, we found that our plots displayed a semicircle in the high-frequency region and an inclined spur in the low-frequency region, in line with both literature precedent for RfA1[16] and expectations for ion-conducting materials contacted by blocking electrodes.[33–37] Importantly, we also noted a clear kinetic isotope effect for the RfA2 films, with a decrease of ~40% in their average conductivity upon moving from H_2O to D_2O vapor. Together, our observations provided additional compelling evidence that RfA2 was a proton-conducting material.

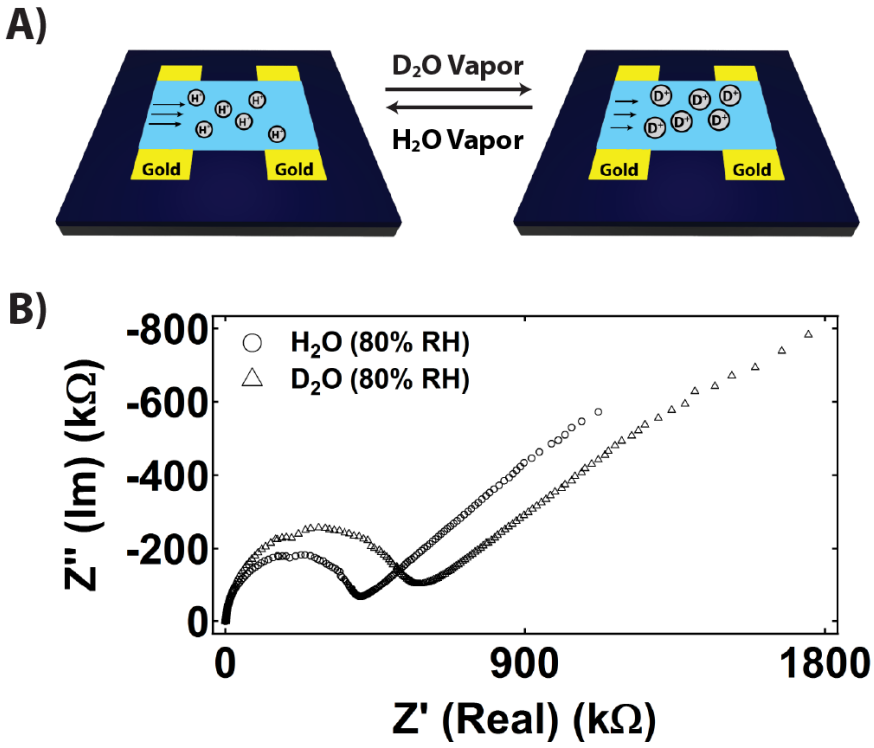

Figure 6.4: A) An illustration of a two-terminal RfA2-based device in the presence of water (H_2O) vapor and deuterium oxide (D_2O) vapor. B) A representative Nyquist plot of the imaginary versus the real parts of the impedance for an RfA2-based two-terminal device in the presence of H_2O (open circles) and D_2O (open triangles). There is a change in the effective film resistance upon moving from H_2O to D_2O, demonstrating the kinetic isotope effect for the RfA2 film.

6.4: Conclusion

In conclusion, we have demonstrated an improved methodology for the production of reflectins in quantities sufficient for materials applications, and our findings constitute a significant advance for several reasons. First, our straightforward protocol omits a challenging chromatography step and enables the expression and purification of potentially difficult-to-handle reflectins in high yield, as demonstrated for the RfA2 "model" system. The presented strategy should be broadly applicable for the production of arbitrary reflectin variants (and perhaps even unrelated proteins) that are sequestered within inclusion bodies (for example, we have included the gel electrophoresis data for RfA1 produced *via* our protocol in Figure S6.4). Furthermore, our methodology has enabled the exploration of RfA2's electrical functionality for the first time, adding to the limited body of knowledge currently available for reflectins' materials properties. Based on the sequence similarity between various reflectins and the demonstrated electrical functionality of both RfA1 and RfA2, we cautiously postulate that protonic conductivity may be a general property of these proteins (although our hypothesis certainly warrants additional investigation). Finally, due to its relatively short amino acid sequence (when compared to RfA1), RfA2 may hold value as a platform for establishing relationships between structure and *in vitro* function for the reflectin family of proteins. Altogether, our observations highlight the potential of reflectins as functional materials and may afford new opportunities for the study of their multi-faceted properties.

6.5: Supplementary Information

Expression and Purification of Reflectin A2: Histidine-tagged wild type reflectin A2 (RfA2) was expressed and purified *via* a protocol that was modified from an analogous one previously

reported for wild type reflectin A1 (RfA1)[31,32]. In brief, an *E. coli* codon optimized gene coding for histidine-tagged wild type RfA2 from *Doryteuthis (Loligo) pealeii* (Genbank: ACZ57765.1) was synthesized and cloned into the pJExpress414 vector (DNA2.0). The vector was transformed into BL21(DE3) cells (Novagen). RfA2 was expressed at 37 °C using Overnight Express Instant Terrific Broth (TB) media (Novagen) supplemented with 100 μg mL^{-1} Carbenicillin. RfA2 was insoluble when expressed at 37 °C and was sequestered in inclusion bodies. The inclusion bodies were then extracted by using BugBuster® (Novagen) according to the manufacturer's suggested protocols. The inclusion bodies were subsequently solubilized in denaturing buffer (pH 7.4, 50 mM sodium phosphate, 300 mM sodium chloride, 6 M guanidine hydrochloride) through repeated manual agitation and sequentially filtered through 5, 0.45, and 0.22 μm filters. The protein was next purified by high-performance liquid chromatography (HPLC) on an Agilent 1260 Infinity system using an Agilent reverse phase C18 column with a gradient evolved from 95% Buffer A:5% Buffer B to 5% Buffer A:95% Buffer B at a flow rate of 1 mL min^{-1} over 30 minutes (Buffer A: 99.9% H2O, 0.1% TFA; Buffer B: 95% acetonitrile, 4.9% H2O, 0.1% TFA) (Figure S6.1). The fractions containing RfA2 were pooled, flash frozen in liquid nitrogen, and lyophilized, yielding > 200 mg of pure RfA2 protein per liter of *E. coli* cell culture.

Characterization of Reflectin A2: Wild type RfA2 was characterized according to a general protocol, which was adopted from the literature[31-34]. Throughout the purification process, purified and unpurified reflectin samples were analyzed by sodium dodecyl sulfate polyacrylamide gel electrophoresis (SDS-PAGE) and GelCode Blue Staining (Thermo) using an Invitrogen XCell *SureLock* Mini using NuPAGE Novex 4-12% Bis-Tris gels, with NuPAGE MOPS as the running buffer under reducing conditions. Stained protein bands were routinely subjected to in-gel tryptic

digestion, as confirmation of protein identity[31-33]. After digestion, the peptides were separated on a reverse phase C18 chromatography column and analyzed by mass spectrometry either on a Synapt G2 instrument (Waters) outfitted with an electrospray ionization source or on an EASY-nLC system (Proxeon Biosystems, now Thermo Scientific) connected to a hybrid LTQ-FT spectrometer (Thermo Scientific) equipped with a nanoelectrospray ion source (Proxeon Biosystems, now Thermo Scientific)[31,34]. The resulting sequence coverages routinely exceeded > 80 % for RfA2 (Figure S6.2).

Fabrication of Reflectin A2-based Devices: The two-terminal devices were fabricated using a protocol modified from established procedures[32]. In brief, silicon dioxide/silicon or glass substrates (International Wafer Service, Inc.) were first cleaned in Piranha solution (1:3 hydrogen peroxide to sulfuric acid) and washed thoroughly. To fabricate devices for two-terminal direct current measurements, arrays of paired electrodes consisting of a 4 nm chromium adhesion layer overlaid with a 40 nm palladium layer were electron-beam evaporated onto SiO_2/Si substrates through a shadow mask. The dimensions of the palladium paired electrodes were 100 μm wide by 400 μm long, with an inter-electrode separation of 50 μm. To fabricate devices for two-terminal alternating current measurements, arrays of paired electrodes consisting of a 4 nm chromium adhesion layer overlaid with a 40 nm gold layer were electron-beam evaporated onto glass substrates through a shadow mask. The dimensions of the gold paired electrodes were 2.5 cm wide by 3 cm long with an inter-electrode separation of 100 μm. For all devices, aqueous solutions containing HPLC-purified RfA2 were prepared and subsequently dropcast onto the electrodes. The resulting films were dried in ambient conditions, and the excess material was scribed away mechanically, leaving the desired completed devices. To convert electron-injecting palladium (Pd)

electrodes to proton-injecting palladium hydride (PdH_x) electrodes, the devices were exposed to a 5% hydrogen/95% argon atmosphere both before and during the electrical measurements.

Physical Characterization of Reflectin A2-based Devices: The devices were characterized with optical and atomic force microscopy, as previously described[31,32]. The dimensions of the reflectin films were determined from analysis of optical images obtained with a Zeiss Axio Imager A1 Microscope. The thicknesses of both dry and humidified reflectin films were determined from the analysis of topographical scans obtained with an Asylum Research MFP-3D Atomic Force microscope outfitted with an Asylum Research Humidity Sensing Cell.

Electrical Characterization of Reflectin A2-based Devices: The completed devices were characterized electrically in two different configurations according to established procedures[32]. The direct current measurements were performed on a Cascade Microtech PM-5 Probe Station outfitted with an Agilent 4156C Semiconductor Parameter Analyzer, with the current was recorded as a function of voltage at a scan rate of ~ 0.6 V/s. The direct current measurements for palladium-contacted and palladium hydride-contacted devices were performed under 100% argon and 5% hydrogen/95% argon atmospheres, respectively. The alternating current measurements were performed with a 4294A Impedance Analyzer (Agilent) at various frequencies with a constant applied voltage of 500 mV. The alternating current measurements for gold-contacted devices were performed under a 100% argon atmosphere. All electrical experiments were performed at an 80% relative humidity, which was monitored with a Fisher Scientific hygrometer.

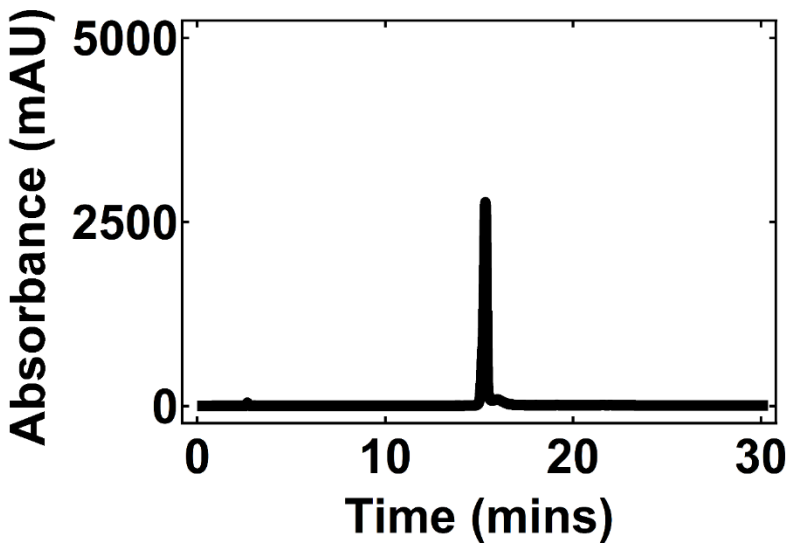

Figure S6.1: A typical analytical reverse phase HPLC chromatogram for RfA2 obtained after inclusion body filtration and concentration. The elution of the protein was monitored at a wavelength of 280 nm. The peak indicates excellent purity.

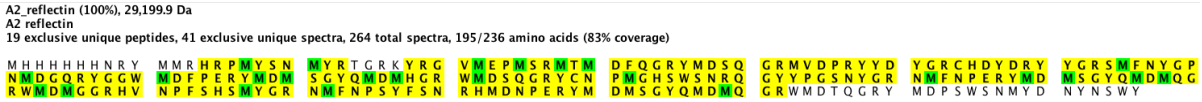

Figure S6.2: A tryptic peptide sequence coverage map obtained from tandem mass spectrometry analysis of the trypsin-digested of the histidine-tagged RfA2 protein. Bolded amino acids with a yellow background correspond to amino acids comprising tryptic peptides. Bolded amino acids with a green background correspond to oxidized amino acids comprising tryptic peptides. The total sequence coverage of ~ 83 % confirmed the purified protein's identity as RfA2 from *Doryteuthis pealeii*.

```
A2              -MHHHHHHNRYMMRHRPMYSNMYRTGRKYRGVMEPMSRMTMDFQGRYMDSQGRMVDPRYY
A1              MAHHHHHHNRYLNRQR-LY-NMYRN--KYRGVMEPMSRMTMDFQGRYMDSQGRMVDPRYY

A2              D-YGRCHDYDRYYGRSMFNYGPNMDGQRYGGWMDFPERYMDMSGYQMDMHGRWMDSQGRY
A1              DYYGRMHDHDRYYGRSMFNQGHSMDSQRYGGWMDNPERYMDMSGYQMDMQGRWMDAQGRF

A2              CNPMGHSWSNRQGYYPG-----SNYGRNMFN----------PERYMDMSGYQMDMQG
A1              NNPFGQMWHGRQGHYPGYMSSHSMYGRNMYNPYHSHYASRHFDSPERWMDMSGYQMDMQG

A2              RWMDMGGRHVNPFSHSMYGRNMFNP--SYFSNRHMDNPERYMDMSGYQMDMQGRWMDTQG
A1              RWMDNYGRYVNPFNHHMYGRNMCYPYGNHYYNRHMEHPERYMDMSGYQMDMQGRWMDTHG

A2              RYMDP----------------------------------------SWSNMYDNY-------
A1              RHCNPFGQMWHNRHGYYPGHPHGRNMFQPERWMDMSGYQMDMQGRWMDNYGRYVNPFSHN

A2              ------------------------------------NSW--------------------
A1              YGRHMNYPGGHYNYHHGRYMNHPERHMDMSSYQMDMHGRWMDNQGRYIDNFDRNYYDYHM

A2              Y
A1              Y
```

Figure S6.3: A sequence alignment of histidine-tagged reflectin A2 and histidine-tagged reflectin A1[31,32] from *D. pealeii*. The alignment was generated by using the MUSCLE software[42,43]. The charged amino acids (D, E, H, K, R) are highlighted in yellow, and they constitute 27.5% of the sequence for RfA2 and 30.3% of the sequence RfA1.

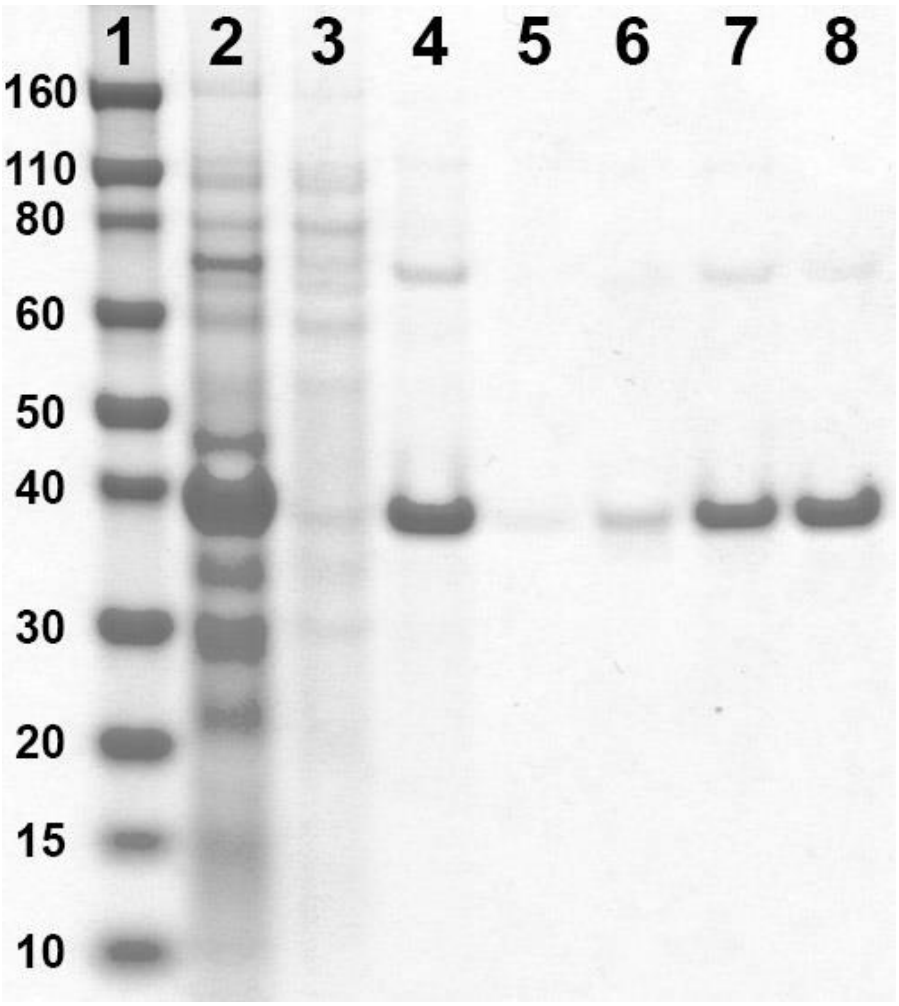

Figure S6.4: Analysis of the expression and purification of histidine-tagged RfA1[31,32] *via* sodium dodecyl sulfate polyacrylamide gel electrophoresis (SDS-PAGE). The overall procedure was identical to the one described for RfA2 above. The stain indicates the total protein. The individual lanes correspond to: lane 1, 10-160 kDa molecular weight standards; lane 2, total protein; lane 3, soluble protein; lane 4, insoluble protein; lane 5, solubilized inclusion bodies; lane 6, filtered inclusion bodies; lane 7, concentrated filtered inclusion bodies; lane 8, HPLC eluate. After HPLC purification, RfA1 produced via this method was indistinguishable from the one produced via the previously reported protocols[31,32].

6.6: Acknowledgements

This chapter is an adaptation of the material as it appears in: D. D. Ordinario, L. Phan, W. G. Walkup IV, Y. Van Dyke, E. M. Leung, M. Nguyen, A. G. Smith, J. Kerr, M. Naeim, I. Kymissis, A. A. Gorodetsky, *RSC Adv.* **2016**, *6*, 57103. The co-authors listed in this publication directed and supervised research which forms the basis for the material in the chapter. Author Contributions: D. D. O. and A. A. G. conceptualized and designed the experiments; D. D. O., L.

P., W. G. W. IV, Y. V. D., E. M. L., and M. N. performed the research; L. P. and W. G. W. IV designed and cloned the genes; L. P., E. M. L., J. K., and M. N. expressed and purified the protein; D. D. O., I. K., and A. A. G. analyzed the data; and D. D. O. and A. A. G. wrote the paper.

6.7: References

1. N. J. Abbott, R. Williamson, L. Maddock, in *Cephalopod Neurobiology: Neuroscience Studies in Squid, Octopus, and Cuttlefish*, Oxford University Press, Oxford, **1995**.
2. L. Borrelli, G. Fiorito, in *Learning and Memory: A Comprehensive Reference*, ed. J. H. Byrne, Academic Press, Oxford, **2008**, ch. 1.31, pp. 605–627.
3. R. T. Hanlon, J. B. Messenger, in *Cephalopod Behaviour*, Cambridge University Press, United Kingdom, **1998**.
4. L. M. Mäthger, E. J. Denton, N. J. Marshall, R. T. Hanlon, *J. R. Soc., Interface* **2009**, *6*, 149–163.
5. R. T. Hanlon, C.-C. Chiao, L. M. Mäthger, K. C. Buresch, A. Barbosa, J. J. Allen, L. Siemann, C. Chubb, in *Animal Camouflage: Mechanisms and Functions*, ed. M. Stevens and S. Merilaita, Cambridge University Press, Cambridge, **2011**, ch. 9, pp. 145–163.
6. G. Kaufman, C. Orlt, Kings of Camouflage, Producers. *Cuttlefish: The Brainy Bunch* [Television Broadcast], Public Broadcasting Service (PBS), **2011**.
7. L. Phan, W. G. Walkup IV, D. D. Ordinario, E. Karshalev, J.-M. Jocson, A. M. Burke, A. A. Gorodetsky, *Adv. Mater.* **2013**, *25*, 5621–5625.
8. L. Phan, D. D. Ordinario, E. Karshalev, W. G. Walkup IV, M. Shenk, A. A. Gorodetsky, *J. Mater. Chem. C* **2015**, *3*, 6493–6498.
9. R. M. Kramer, W. J. Crookes-Goodson, R. R. Naik, *Nat. Mater.* **2007**, *6*, 533–538.

10. G. Qin, P. B. Dennis, Y. Zhang, X. Hu, J. E. Bressner, Z. Sun, W. J. Crookes-Goodson, R. R. Naik, F. G. Omenetto, D. L. Kaplan, *J. Polym. Sci., Part B: Polym. Phys.* **2013**, *51*, 254–264.
11. J. Jin, V. Reese, R. Coler, D. Carter, M. Rolandi, *Adv. Healthcare Mater.* **2014**, *3*, 349–353.
12. P. Hassanzadeh, M. Kharaziha, M. Nikkhah, S. Shin, J. Jin, S. He, W. Sun, C. Zhong, M. Dokmeci, A. Khademhosseini, M. Rolandi, *J. Mater. Chem. B* **2013**, *1*, 4217–4224.
13. A. Cooper, C. Zhong, Y. Kinoshita, R. Morrison, M. Rolandi, M. Zhang, *J. Mater. Chem.* **2012**, *22*, 3105–3109.
14. L. Phan, R. Kautz, J. Arulmoli, I. H. Kim, D. T. T. Le, M. A. Shenk, M. M. Pathak, L. A. Flanagan, F. Tombola, A. A. Gorodetsky, *ACS Appl. Mater. Interfaces* **2016**, *8*, 278–284.
15. Y. J. Kim, W. Wu, S. E. Chun, J. Whitacre, C. J. Bettinger, *Proc. Natl. Acad. Sci. U. S. A.* **2013**, *110*, 20912–20917.
16. D. D. Ordinario, L. Phan, W. G. Walkup IV, J.-M. Jocson, E. Karshalev, N. Hüsken, A. A. Gorodetsky, *Nat. Chem.* **2014**, *6*, 596–602.
17. D. D. Ordinario, L. Phan, J.-M. Jocson, T. Nguyen, A. A. Gorodetsky, *APL Mater.* **2015**, *3*, 014907.
18. D. D. Ordinario, L. Phan, Y. Van Dyke, T. Nguyen, A. G. Smith, M. Nguyen, N. M. Mofid, M. K. Dao, A. A. Gorodetsky, *Chem. Mater.* **2016**, *28*, 3703–3710.
19. C. Zhong, Y. Deng, A. F. Roudsari, A. Kapetanovic, M. P. Anantram, M. Rolandi, *Nat. Commun.* **2011**, *2*, 476.
20. Y. Deng, E. Josberger, J. Jin, A. F. Rousdari, B. A. Helms, C. Zhong, M. P. Anantram, M. Rolandi, *Sci. Rep.* **2013**, *3*, 2481.

21. W. J. Crookes, L. L. Ding, Q. L. Huang, J. R. Kimbell, J. Horwitz, M. J. McFall-Ngai, *Science* **2004**, *303*, 235–238.

22. A. R. Tao, D. G. DeMartini, M. Izumi, A. M. Sweeney, A. L. Holt, D. E. Morse, *Biomaterials* **2010**, *31*, 793–801.

23. M. Izumi, A. M. Sweeney, D. G. DeMartini, J. C. Weaver, M. L. Powers, A. R. Tao, T. V. Silvas, R. M. Kramer, W. J. Crookes-Goodson, L. M. Mäthger, R. R. Naik, R. T. Hanlon, D. E. Morse, *J. R. Soc., Interface* **2010**, 7, 549–560.

24. R. Levenson, C. Bracken, N. Bush, D. E. Morse, *J. Biol. Chem.* **2016**, 291, 4058–4068.

25. D. G. DeMartini, D. V. Krogstad, D. E. Morse, *Proc. Natl. Acad. Sci. U. S. A.* **2013**, *110*, 2552–2556.

26. D. G. DeMartini, M. Izumi, A. T. Weaver, E. Pandolfi, D. E. Morse, *J. Biol. Chem.* **2015**, *290*, 15238–15249.

27. D. G. DeMartini, A. Ghoshal, E. Pandolfi, A. T. Weaver, M. Baum, D. E. Morse, J. *Exp. Biol.* **2013**, *216*, 3733–3741.

28. L. Mäthger, S. L. Senft, M. Gao, S. Karaveli, G. R. R. Bell, R. Zia, A. M. Kuzirian, P. B. Dennis, W. J. Crookes-Goodson, R. R. Naik, G. W. Kattawar, R. T. Hanlon, *Adv. Funct. Mater.* **2013**, *23*, 3980–3989.

29. L. F. Deravi, A. P. Magyar, S. P. Sheehy, G. R. R. Bell, L. M. Mäthger, S. L. Senft, T. J. Wardill, W. S. Lane, A. M. Kuzirian, R. T. Hanlon, E. L. Hu, K. K. Parker, *J. R. Soc., Interface* **2014**, *11*, 20130942.

30. J. B. Messenger, *Biol. Rev. Cambridge Philos. Soc.* **2001**, *76*, 473–528.

31. L. Phan, W. G. Walkup IV, D. D. Ordinario, E. Karshalev, J.-M. Jocson, A. M. Burke, A. A. Gorodetsky, *Adv. Mater.* 2013, **25**, 5621–5625.

32. D. D. Ordinario, L. Phan, W. G. Walkup IV, J.-M. Jocson, E. Karshalev, N. Hüsken, A. Gorodetsky, *Nat. Chem.* 2014, **6**, 596–602.

33. A. Kalli, S. Hess, *Proteomics* 2012, **12**, 21–31.

34. A. Shevchenko, H. Tomas, J. Havlis, J. V. Olsen, M. Mann, *Nat. Protoc.* 2006, **1**, 2856–2860.

35. J. L. Weiss, N. A. Evans, T. Ahmed, J. D. J. Wrigley, S. Khan, C. Wright, J. N. Keen, A. Holzenburg, J. B. C. Findlay, *Biochim. Biophys. Acta, Biomembr.* **2005**, *1668*, 164–174.

36. H. Morgan, R. Pethig, G. T. Stevens, *J. Phys. E: Sci. Instrum.* **1986**, *19*, 80–82.

37. E. Barsoukov, J. R. Macdonald, in *Impedance Spectroscopy: Theory, Experiment and Applications, 2nd ed.*, Wiley, Hoboken, **2005**.

38. X.-Z. Yuan, C. Song, H. Wang, J. Zhang, in *Electrochemical Impedance Spectroscopy in PEM Fuel Cells: Fundamentals and Applications*, Springer, New York, **2012**.

39. R. A. Huggins, *Ionics* **2002**, *8*, 300–313.

40. Z. Xie, C. Song, B. Andreaus, T. Navessin, Z. Shi, J. Zhang, S. Holdcroft, *J. Electrochem. Soc.* **2006**, *153*, 173–178.

41. T. Soboleva, Z. Xie, Z. Shi, E. Tsang, T. Navessin, S. Holdcroft, *J. Electroanal. Chem.* **2008**, *622*, 145–152.

42. R. C. Edgar, *Nucleic Acids Res.* **2004**, *32*, 1792 – 1797.

43. R. C. Edgar, *BMC Bioinf.* **2004**, *5*, 113.

CHAPTER 7 Conclusion

The body of work presented in this thesis provides a foundation for development of novel reflectin-based optical devices and cell growth substrates. We first developed process methods for the heterologous expression and purification of bulk quantities of reflectin A1 protein, subsequently using this material to fabricate functional thin films that can reflect visible and infrared light. Films coated on rigid and flexible substrates were optically characterized and demonstrated an ability to act as reconfigurable infrared camouflage whereas those coated on flexible FEP tape lend to a more versatile application as a wearable product with the goal of endowing soldiers with added nighttime protection in the form of infrared identification tags. Moreover, we demonstrated that film reflectance could be modulated *via* chemical (acid), mechanical, and electrical triggers, further enhancing versatility of infrared camouflage where the infrared signature may need to be toggled between the "on" and "off" states in order to protect soldiers transitioning between cover.

To expand our protein tool box for generation of novel reflectin-based optical devices we adapted and optimized our procedure for expression and purification of reflectin A1 to allow for high-throughput production and purification of other isoforms in the reflectin family, including the troublesome reflectin A2 isoform. Time consuming and costly process steps were eliminated and replaced with rapid, sequential filtrations, all while retaining the high purity (>99%) and increasing the yield (~1 gram pure protein per liter culture) of the original protocol. Our novel procedures for reflectin purification are easily scalable for industrial applications, allowing for the coating of large area surfaces and thus widespread commercial and military applications that seek to use reflectin as the active material.

Additionally, we found novel use for reflectin as an effective substrate for hNSPC cell growth and differentiation and illustrated that it performs similarly to the commonly used cell adherents fibronectin and laminin, but superior to poly-d-lysine. Reflectin's unique and unusual amino acid sequence may imbue it with qualities that make it a favorable growth substrate for stem cell related research, and when coupled with adherent cells that contain proton channels, the visible color changes associated with the pH sensitivity of reflectin films may facilitate their inclusion as an acid sensor in future biomedical devices.

Future biophysical and materials studies providing insight into the tunability of reflectin-based Bragg reflector structures and textured reflectin surfaces, could provide additional means to enhance overall film brightness, angle-dependence, and color tunability for camouflage applications. Further interrogation of reflectin protein structure and sequence relationships, could pave the way towards engineered reflectin proteins with tightly defined reflectance ranges or chemically inducible reflectance changes. Identification of minimally functional reflectin subunits/domains could provide low cost media for stem cell proliferation as well as a drug discovery platform for identifying novel proton channel inhibitors.